Dissertation zur Erlangung des Doktorgrades
der Fakultät für Chemie und Pharmazie
der Ludwig–Maximilians–Universität München

Light-matter interactions: From ionization to the control of nuclear and electron dynamics

Robert Arthur Siemering

aus

München, Deutschland

2017

Erklärung:

Diese Dissertation wurde im Sinne von §7 der Promotionsordnung vom 28. November 2011 von Frau Prof. Dr. Regina de Vivie-Riedle betreut.

Eidesstattliche Versicherung:

Diese Dissertation wurde eigenständig und ohne unerlaubte Hilfe erarbeitet.

München, den 10.04.2017,
Robert Siemering

Dissertation eingereicht am:	10.04.2017
1. Gutachterin:	Prof. Dr. Regina de Vivie-Riedle
2. Gutachter:	Prof. Dr. Matthias Kling
Tag der mündlichen Prüfung:	16.05.2017

Contents

Abstract v

List of publications vii

1 Introduction 1

2 Methods 3
2.1 Quantum chemistry . . . 3
2.1.1 The Hartree-Fock method . . . 4
2.1.2 Multi Reference Configuration Interaction (MRCI) . . . 6
2.1.3 Complete Active Space Self Consistent Field (CASSCF) . . . 6
2.2 Nuclear quantum dynamics on potential energy surfaces . . . 6
2.2.1 Time dependent and time independent coupling in the system Hamiltonian . . . 7
2.2.2 Methods for solving the time-dependent Schrödinger equation . . . 7

3 Tunnel ionization 9
3.1 Small overview of theoretical descriptions of tunnel ionization . . . 9
3.2 Angular dependent tunnel ionization in small hydrocarbons . . . 12
3.3 Angular dependent tunnel ionization from an excited state . . . 37

4 Control of nuclear dynamics 45
4.1 Suppression of a barrier with a laser . . . 45
4.2 CEP control of directional bond cleavage . . . 57
4.3 CEP control of bond rearrangement . . . 65

5 Control of electron dynamics 73

6 Summary and Outlook 81

7 List of abbreviations 85

References 87

Abstract

Understanding light-matter interaction is important to control the electron and nuclear dynamics of quantum-mechanical systems. The present work investigates this in the form of angular dependent tunnel ionization and different control mechanisms for nuclear, electron and coupled dynamics. With the help of close collaboration with experimental groups several control mechanisms could be examined and explained. The refined methods and models for these studies can be expanded for different experiments or more general concepts. The first part of this thesis focuses on tunnel ionization as one of the fundamental quantum-mechanical light -matter interactions while the second and third part investigates the control of nuclear and electron dynamics in depth.

The angular dependent tunnel ionization of small hydrocarbons and the impact of their field dressed orbitals are researched in chapter 3. Advanced quantum chemical methods are used to explain experimental findings that could not be recognized by only looking at the Highest Occupied Molecular Orbital (HOMO). The so studied molecules show the importance to consider field dressed instead of field free orbitals to understand the light-matter interaction, to replicate experimental findings with theoretical models and to predict the behavior of different molecules. The influence of Rydberg character in virtual orbitals, that can become populated in a field dressed picture, can explain the difference in the angular dependent tunnel ionization for two similar derivates of Cyclohexadiene (CHD) and the lobed structure for C_2H_4. This chapter also shows the success of adapting a previous used model for diatomic systems to polyatomic systems.

The second part (chapter 4) investigates the deprotonation and isomerization reaction of acetylene (C_2H_2) and allene (C_3H_4) and the potential control with laser pulses over theses reaction. The first control mechanism utilizes the light field to suppress the reaction barrier, which allows molecules with lower energy to undergo isomerization and therefore increase the rate of the reaction. The second scheme controls the asymmetry of the reaction, so that either the left to right or right to left isomerization is preferred. This control is exercised by directly manipulating the nuclear wave packet with the Carrier–Envelope–Phase (CEP) of the laser pulse. The mechanism relies on forming a superposition of different normal modes that are excited by different means and therefore have a phase difference. One or more normal modes are excited by the light field and get the CEP imprinted in their phase while the other important normal modes are indirectly excited by the ionization process. This enables directional control of the nuclear dynamics in symmetric molecules. The concept of forming the superposition is general enough to be used in different reactions and molecules.

In the last part (chapter 5) the control of electron dynamics with laser pulses is studied. The test case is the selective population of dressed states (SPODS) in the potassium dimer (K_2). There a first pulse will populate an electronic superposition between the ground and first excited state. Depending on the relative phase of the second pulse to the oscillating dipole created by the electronic wave packet, the upper or lower dressed state will be populated. Excitation from the two different dressed states leads to two distinguishable final states. Although the scheme focuses on the control of the electron dynamics, the whole mechanism is also heavily influenced by the associated nuclear dynamics.

List of publications

This thesis is based on the following six publications listed in chronological order. They are reprinted in the chapters 3 (**4, 6**), 4 (**2, 3, 5**) and 5 (**1**).

1 T. Bayer, H. Braun, C. Sarpe, R. Siemering, P. von den Hoff, R. de Vivie-Riedle, T. Baumert, and M. Wollenhaupt:
Charge oscillation controlled molecular excitation
Phys. Rev. Lett. **110** (2013), 123003.

2 E. Wells, C. E. Rallis, M. Zohrabi, R. Siemering, B. Jochim, P. R. Andrews, U. Ablikim, B. Gaire, S. De, K. D. Carnes, B. Bergues, R. de Vivie-Riedle, M. F. Kling, and I. Ben-Itzhak:
Adaptive strong-field control of chemical dynamics guided by three-dimensional momentum imaging
Nat. Commun. **4** article number: 2895 (2013).

3 A. S. Alnaser, M. Kübel, R. Siemering, B. Bergues, N. G. Kling, K. J. Betsch, Y. Deng, J. Schmidt, Z. A. Alahmed, A. M. Azzeer, J. Ullrich, I. Ben-Itzhak, R. Moshammer, U. Kleineberg, F. Krausz, R. de Vivie-Riedle, and M.F. Kling :
Subfemtosecond steering of hydrocarbon deprotonation through superposition of vibrational modes
Nat. Commun. **5** 3800 (2014).

4 R. Siemering, O. Njoya, T. Weinacht, and R. de Vivie-Riedle:
Field-dressed orbitals in strong-field molecular ionization
Phys. Rev. A **92** (2015), 042515.

5 M. Kübel, R. Siemering, C. Burger, Nora G. Kling, H. Li, A. S. Alnaser, B. Bergues, S. Zherebtsov, A. M. Azzeer, I. Ben-Itzhak, R. Moshammer, R. de Vivie-Riedle, and M. F. Kling:
Steering Proton Migration in Hydrocarbons Using Intense Few-Cycle Laser Fields
Phys. Rev. Lett. **116** (2016), 193001.

6 Bethany Jochim, R. Siemering, M. Zohrabi1, A. Voznyuk, J. B. Mahowald, D. G. Schmitz, K. J. Betsch, Ben Berry, T. Severt, Nora G. Kling, T. G. Burwitz, K. D. Carnes, M. F. Kling, I. Ben-Itzhak, E. Wells, and R. de Vivie-Riedle:
The importance of Rydberg orbitals in dissociative ionization of small hydrocarbon molecules in intense few-cycle laser pulses
Manuscript, (unpublished).

Additional publications listed in chronological order:

7 P. von den Hoff, R. Siemering and R. de Vivie-Riedle:
Molecular processes controllable by electron dynamics.
in: Ultrafast Phenomena XVII, M. Chergui, D. Jonas, E. Riedle, R.W. Schoenlein, A. Taylor, eds. (Oxford University Press, Inc., New York 2011), 101-103.

8 P. von den Hoff, M. Kowalewski, R. Siemering and R. de Vivie-Riedle:
Electron dynamics and its control in molecules: From diatomics to larger molecular systems.
IEEE Journal of Selected Topics in Quantum Electronics **18**(2012), 119-129.

9 P. von den Hoff, S. Thallmair, M. Kowalewski, R. Siemering, and R. de Vivie-Riedle:
Optimal control theory - closing the gap between theory and experiment
Phys. Chem. Chem. Phys. **14**(2012), 14460-14485.

10 H. Braun, P. von den Hoff, T. Bayer, R. Siemering, R. de Vivie-Riedle, M. Wollenhaupt, and T. Baumert:
Efficient attosecond control of electron dynamics in molecules
in: Ultrafast Phenomena XVIII, M. Chergui, S. Cundiff, A. Taylor, R. de Vivie-Riedle, K. Yamanouchi (Eds.), *EPJ Web of Conferences* **41** (2013), 02026.

11 S. Thallmair, R. Siemering, P. Kölle, M. Kling, M. Wollenhaupt, T. Baumert, R. de Vivie-Riedle:
The Interplay of Nuclear and Electronic Motion in the Control of Molecular Processes: A Theoretical Perspective.
in: Molecular Quantum Dynamics – From Theory to Applications, F. Gatti (Ed.), Springer, 2014, 213–248.

12 H. Braun, T. Bayer, C. Sarpe, R. Siemering, R. de Vivie Riedle, T. Baumert, and M. Wollenhaupt:
Coupled electron-nuclear wavepacket dynamics in potassium dimers
J. Phys. B: At. Mol. Opt. Phys. **47** (2014), 124015.

13 R. Siemering, M. Kübel, B. Bergues, A.S. Alnaser, M. Kling, and R. de Vivie-Riedle:
Sub-femtosecond steering of carbon hydrogen bonds
in: Ultrafast Phenomena XIX, K. Yamanouchi, S. Cundiff, R. de Vivie-Riedle, M. Kuwata-Gonokami, L. DiMauro (Eds.), Springer Proceedings in Physics 162 (Springer International Publishing, 2015), 126-129.

14 C. Burger, Nora G. Kling, R. Siemering, A. S. Alnaser, B. Bergues, A. M. Azzeer, R. Moshammer, R. de Vivie-Riedle, M. Kübel and M. Kling:
Visualization of bond rearrangements in acetylene using near single-cycle laser pulses
Faraday Discuss., 2016, Advance Article

1 Introduction

One of the big goals in chemistry is the understanding of natural and artificial processes on a molecular scale and the utilization of the so gained knowledge to manipulate the investigated systems on the molecular level as well [1–3]. The main tool for observation and control on this small length and time scale are short and ultrashort laser pulses, because the electric field can directly interact with the nuclei and electrons of the system. The first experiments focused on following the nuclear dynamics of molecules [4–6], but advancements in laser technology also allowed the observation of electron dynamics and furthermore the control of nuclear and electron dynamics. Nowadays lasers cover a wide area of time scales from almost single cycle attosecond pulses to microsecond pulses and an energy range from the infrared to the ultraviolet, while also highly tunable in phase, frequency and intensity to create many different pulse-shapes for a very selective pulse-molecule interaction [7–14]. While this is a powerful toolbox many experiments involving them are carried out in the gas phase or in low pressure environments using traps. The insight to fundamental light-matter interaction from these experiments will help the understanding of photochemical reaction and offer a pathway to light as potential catalysts for chemical reactions.

While the Schrödinger equation in principal describes all molecular processes even the solution for stationary systems with more than one electron is not trivial. For the systems of interest excited electronic states and time-dependent dynamics are also involved and the resulting complexity of the Schrödinger equation is often not solvable within a reasonable time [15–19]. Therefore theorists developed several approximations and simplified approaches to calculate the properties of quantum systems [20]. The computational effort is a severe restraint for big systems so linear scaling algorithms are an important development [21–24]. There are two general approaches for solving the time independent Schrödinger equation. Density based methods (DFT) [25] are quite fast and can accommodate large molecules, but depending on the electronic structure, time dependent density functional theory (TDDFT) [26–28] is not accurate enough for excited states, especially in the vicinity of conical intersections (CoIn) [29, 30]. On the other hand multi-referential, wave function based methods like coupled cluster (CC) [31, 32], complete or restricted active space (CAS/RAS) [33] and their combination with perturbation theory (CASPT2) [34–36] have the theoretical limit of a full CI (configuration interaction) wave function, that is, together with the limit of a full basis set [37–39], the numerical solution of the Schrödinger equation. However computational resource limitations keep the applications of these methods away from the theoretical limit.

The time dependent Schrödinger equation also allows the description of nuclear and electron dynamics, but a full quantum mechanical description for both simultaneously remains unachievable for anything but very small systems. Nuclear dynamics on fully calculated potential energy surfaces (PES) [40] are limited to few dimensions, but if the Hamiltonian can be expanded as a sum of products of one-particle operators the Multi Configuration Time Dependent Hartree (MCTDH) algorithm can calculate wave packets for up to 80 dimensions [41, 42]. Another option is to calculate the motion of the nuclei classically and the electron energy and gradients “on-the-fly”. Multiple electronic states can be coupled and therefore allow the trajectory to switch between them during the time evolution [43–46]. A swarm of trajectories can in many cases approximate the behavior of the nuclei, but it fails if the phase of the nuclear wave packet is important. Most time dependent electron dynamics either ignore the nuclear motion outright or use classic trajectories [47, 48]. So another obstacle is the bidirectional coupling between the electron and the nuclear wave function, i.e. that the electron wave function influences the nuclear wave function as well as the other way around. Therefore the theoretical approach has to be tailored to the system under investigation.

The first interaction between strong lasers and an atomic or molecular system that comes to mind is the excitation and especially ionization of an atom or molecule within the laser field. For a single atom, especially the hydrogen atom or noble gases theses interactions are well researched in experiment and theory in many different regimes. There are also many experiment and theoretical studies for small diatomic molecules, for example H_2 [49–54], HCl [55, 56], N_2 [57], O_2 [57], NO [58], CO [59, 60], the most renowned being NaI, as it was the first molecule studied in real time by the group of Nobel laureate Achmed H. Zewail [4, 61, 62]. For the ionization of diatomic molecules the angular dependence of the tunnel ionization is of special interest, as it reveals that not only the electronic structure of the valence orbitals (or highest occupied orbitals (HOMO)) but also the interaction of the laser field with neighboring orbitals is relevant for the observable effects [63]. This work investigates the angular tunnel ionization of more complex molecules in chapter 3 in detail. The first example is the homologue series of small hydrocarbons acetylene C_2H_2, ethylene C_2H_4 and ethane C_2H_6 and the second example is the molecule cyclohexadien (CHD) and its substituted derivates α-terpinene (AT) and α-phellandrene (AP).

The next step is the control of nuclear or electron dynamics with laser pulses. The main pathway for reaction control is utilizing photochemical reactions either via CoIn [29, 64–66] or different excited states [67]. This type of control uses the natural occurring gradients and energy differences of electronic states to steer the nuclei. In some cases the effect is enhanced by manipulating the nuclear wave packet for a specific behavior. In contrast methods that utilize the laser field directly include phase or angular dependent ionization or excitation, altering the gradients of the electronic state, for example via Stark shift, or forming specific nuclear wave packets before or during the excitation or ionization. This work focuses on the latter two points demonstrated primarily on acetylene (C_2H_2) in chapter 4. The first example is the suppression of the isomerization barrier of the reaction from acetylene to vinylidene, with an optimized laser pulse. The second example focuses on the same reaction, but utilizes the CEP of the laser pulse to directly control the nuclear wave packet instead.

Electron dynamics are very important in reactions, that depend on absorbing light, which includes all photochemical reactions, but also light harvesting complexes in nature or solar cells. The conditions of these reactions are typically long exposure to incoherent light. Laser pulses on the other hand enable a more selective interaction and therefore possible control of the electron dynamics. These are mostly studied in atomic or other small systems. This work discusses electron dynamics and the influence of nuclear dynamics for the example of selective population of dressed states (SPODS) in the potassium dimer K_2 and the subsequent control of the final excited state, measured by the energy of the photo electrons. While the control mechanism is for the electronic structure there is a non negligible interaction between the electron and nuclear dynamics as outline in chapter 5.

2 Methods

The following chapter is a short overview of the theoretical methods that were used for quantum-chemical and quantum-dynamical calculations [16–19, 68]. The quantum-chemical methods in section 2.1 allow for approximate solutions of the stationary Schrödinger equation, that are used for potential energy surfaces (PES), gradients, molecular orbitals and electronic wave functions. Quantum-chemical calculations in this work have been performed by the program package MOLPRO [69]. While the electron dynamics is covered by the quantum-chemical methods the nuclear dynamics is calculated with the quantum-dynamics methods from section 2.2, that describe the motion of the nuclear wave packet and therefore its location on the PES.

2.1 Quantum chemistry

For the description of the dynamics of quantum mechanical system, for example molecules, the solution of the time dependent Schrödinger equation

$$i\frac{\partial \Psi_{\text{mol}}(R,r,t)}{\partial t} = \hat{H}\Psi_{\text{mol}}(R,r,t) \tag{2.1}$$

is needed.

Hereby is $\Psi_{\text{mol}}(R,r,t)$ the molecular wave function, depending on the nuclear coordinates R, the electron coordinates r and the time t. The Hamilton operator of the quantum mechanical system

$$\hat{H} = \hat{T}_{\text{nuc}} + \underbrace{\hat{T}_{\text{el}} + \hat{V}_{\text{nuc,nuc}} + \hat{V}_{\text{nuc,el}} + \hat{V}_{\text{el,el}}}_{\hat{H}_{\text{el}}} \tag{2.2}$$

consists of the operators for the kinetic energy of the nuclei ($\hat{T}_{\text{nuc}}$) and the electrons ($\hat{T}_{\text{el}}$) as well as the operators for the coulomb interaction between the nuclei ($\hat{V}_{\text{nuc,nuc}}$), between the electrons ($\hat{V}_{\text{el,el}}$) and between the nuclei and electrons ($\hat{V}_{\text{nuc,el}}$). Normally the terms $\hat{T}_{\text{el}}$, $\hat{V}_{\text{nuc,nuc}}$, $\hat{V}_{\text{el,el}}$ and $\hat{V}_{\text{nuc,el}}$ are combined as the electronic Hamilton operator $\hat{H}_{\text{el}}$. To solve the Schrödinger equation the molecular wave function $\Psi_{\text{mol}}(R,r,t)$ is separated in the nuclear wave function $\chi_i(R,t)$ and the electronic wave function $\Phi_i(r,t,\bar{R})$ and expanded in the basis of the electronic eigenfunctions:

$$\Psi_{mol}(R,r,t) = \sum_i \chi_i(R,t)\Phi_i(r,t,\bar{R}). \tag{2.3}$$

The notation $\Phi_i(r,t,\bar{R})$ designates the parametric dependence of the electronic wave function from the nuclear coordinate R. The right part of equation 2.1 can be reformulated with the help from equations 2.2 and 2.3 to:

$$\hat{H}\Psi(R,r,t) = (\hat{H}_{\text{el}} + \hat{T}_{\text{nuc}})\sum_i \chi_i(R,t)\Phi_i(r,t,\bar{R}). \tag{2.4}$$

Multiplicating equation 2.4 with the total electronic wave function $\sum_j \Phi_j^*(r,t,\bar{R})$ from left and subsequent integration over the electronic coordinate r leads to:

$$\begin{aligned}\int \mathrm{d}r \sum_j \Phi_j^*(r,t,\bar{R})\hat{H}\Psi(R,r,t) = \\ \int \mathrm{d}r \sum_j \Phi_j^*(r,t,\bar{R})(\hat{H}_{\text{el}} + \hat{T}_{\text{nuc}}) \sum_i \chi_i(R,t)\Phi_i(r,t,\bar{R}) \\ = \int \mathrm{d}r \sum_j \sum_i \Phi_j^*(r,t,\bar{R})\hat{H}_{\text{el}}\Phi_i(r,t,\bar{R})\chi_i(R,t) \\ + \int \mathrm{d}r \sum_j \sum_i \Phi_j^*(r,t,\bar{R})\hat{T}_{\text{nuc}}\Phi_i(r,t,\bar{R})\chi_i(R,t).\end{aligned} \tag{2.5}$$

The nuclei are over a thousand times heavier than the electrons, and are therefore much slower than them. This allows the electrons to accustom themselves to the changes in nuclear geometry adiabatically. This is the justification of the Born-Oppenheimer approximation, that the influence of the kinetic nuclear operator $\hat{T}_{\text{nuc}}$ on the electronic wave function $\Phi_i(r,t,\bar{R})$ can be neglected. This allows to simplify equation 2.5 to:

$$\begin{aligned}\int \mathrm{d}r \sum_j \Phi_j^*(r,t,\bar{R})\hat{H}\Psi(R,r,t) = \\ \int \mathrm{d}r \sum_j \sum_i \underbrace{\Phi_j^*(r,t,\bar{R})\hat{H}_{\text{el}}\Phi_i(r,t,\bar{R})}_{E_{\text{el},i}(R)\cdot\delta_{ij}} \chi_i(R,t) \\ + \int \mathrm{d}r \sum_j \sum_i \underbrace{\Phi_j^*(r,t,\bar{R})\Phi_i(r,t,\bar{R})}_{\delta_{ij}} \hat{T}_{\text{nuc}}\chi_i(R,t) \\ = \sum_i (E_{\text{el},i}(R) + \hat{T}_{\text{nuc}})\chi_i(R,t).\end{aligned} \tag{2.6}$$

Substituting equation 2.6 in 2.1 gives the time dependent Schrödinger equation for the nuclear dynamics:

$$i\frac{\partial\chi(R,t)}{\partial t} = \sum_i (E_{\text{el},i}(R) + \hat{T}_{\text{nuc}})\chi_i(R,t). \tag{2.7}$$

Solving this differential equation needs the electronic eigenenergies $E_{\text{el},i}(R)$ of the considered system in dependence of the nuclear geometry. These can be calculated with the stationary Schrödinger equation of the electrons:

$$\hat{H}_{\text{el},i}\Phi(r,\bar{R}) = E_{\text{el},i}\Phi(r,\bar{R}) \tag{2.8}$$

This electronic Schrödinger equation for a specific nuclear geometry can be solved with appropriate quantum chemical methods, either wave function based methods like Hartree-Fock and extensions or density functional based.

The main method used in the calculations in the following chapters is the complete-active-space-self-consistent field (CASSCF) method. So beginning with the root method Hartree-Fock the following sections explain these methods.

2.1.1 The Hartree-Fock method

Within the Hartree-Fock method, that is the foundation of all other wave function based methods, the electronic wave function Φ is generally written as a slater determinant of the one-electron wave functions

(spin orbitals) ϕ:

$$\begin{aligned}\Phi(r_1, r_2, \ldots, r_n) &= \frac{1}{\sqrt{n!}} \begin{vmatrix} \phi_1(r_1) & \phi_2(r_1) & \cdots & \phi_n(r_1) \\ \phi_1(r_2) & \phi_2(r_2) & \cdots & \phi_n(r_2) \\ \vdots & \vdots & \ddots & \vdots \\ \phi_1(r_n) & \phi_2(r_n) & \cdots & \phi_n(r_n) \end{vmatrix} \\ &= \big|\phi_1(r_1), \phi_2(r_2), \ldots, \phi_n(r_n)\big\rangle.\end{aligned} \tag{2.9}$$

The spin orbitals ϕ are the product of the spatial component φ and the spin component σ, with $\sigma \in \{|\alpha\rangle, |\beta\rangle\}$. The basis of the spin orbitals is chosen to be orthonormal, i.e. $\langle\phi_i|\phi_j\rangle = \delta_{ij}$ (also $\langle\alpha|\alpha\rangle = 1$, $\langle\beta|\beta\rangle = 1$ and $\langle\alpha|\beta\rangle = \langle\beta|\alpha\rangle = 0$). The spin orbitals or molecular orbitals (MO) are represented in the basis of atomic orbitals (AO). The shape and number of atomic orbitals are defined by the basis set.

The slater determinant (equation 2.9) satisfies the Pauli exclusion principle and describe an antisymmetric wave function. Two electrons with the same four quantum numbers are equivalent to two identical spin orbitals ($\phi_i = \phi_j$), which leads to two identical columns in the determinant, causing the value of it to be zero. Swapping two electrons equates to swapping two rows in the determinant, leading to an inversion of the sign.

The slater determinant is not an eigenfunction of the electronic Hamiltonian $\hat{H}_{\text{el}}$ and therefore not an exact solution of the Schroedinger equation. For this reason the expectation value

$$\langle\hat{H}_{\text{el}}[\{\phi_i\}]\rangle = \big\langle\Phi(r_1, r_2, \ldots, r_n)\big|\hat{H}_{\text{el}}\big|\Phi(r_1, r_2, \ldots, r_n)\big\rangle = \langle E(\Phi^{\text{HF}})\rangle \tag{2.10}$$

is calculated. With the help of the variational theorem, stating that these energies are greater or equal to the true energy of the system $\langle E(\Phi^{\text{HF}})\rangle \geq E(\Phi^{\text{exakt}})$, the wave function can be varied, to reach the lowest energy. So the functional

$$L[\{\phi_i\}] = \langle\hat{H}_{\text{el}}[\{\phi_i\}]\rangle - \sum_{i=1}^{N}\sum_{j=1}^{N}\lambda_{ij}(\langle\phi_i|\phi_j\rangle - \delta_{ij}), \tag{2.11}$$

with the auxiliary condition of orthonormal orbitals, is minimized by varying the molecular orbitals ϕ_i.

This leads to the non-canonical Hartree-Fock equation

$$\hat{f}(1)\phi_1(1) = \sum_{j=1}^{N}\lambda_{j1}\phi_j(1), \tag{2.12}$$

that can be transformed with an unitary operation into the canonical form

$$\hat{f}(1)\phi_1(1) = \lambda_1\phi_1(1) \tag{2.13}$$

The Fock-operator

$$\hat{f}(1) = \hat{T}_{\text{el},1} + \hat{V}_{\text{nuc,el},1} + \sum_j(\hat{J}_j(1) - \hat{K}_j(1)) \tag{2.14}$$

with

$$\hat{J}_j(1) = \int \mathrm{d}r_2 \frac{|\phi_j(2)|^2}{|r_1 - r_2|} \tag{2.15}$$

and

$$\hat{K}_j(1)\phi_1(1) = \left[\int \mathrm{d}r_2\phi_j(2)^* \frac{1}{|r_1 - r_2|}\phi_1(2)\right]\phi_j(1) \tag{2.16}$$

is an effective one electron operator and invariant toward unitary transformations. Because the operator is dependent on the orbitals ϕ_i, the Hartree-Fock calculations need an initial guess for a set of starting orbitals. A common starting point are the molecular orbitals (MO) from the Hückel approximation. With an iterative method the orbital optimization reaches a self consistent field (SCF). The form of the atomic orbitals (AO) is given by the basis set. To reduce the calculation effort the radial functions are approximated by Gaussian functions instead of slater functions, as the four center two electron integral is easier to calculate. The quality of the optimized molecular orbitals is dependent on the quality of the basis set. The Hartree-Fock method utilizes a mean field of the electrons and can not describe the electron correlation accurately. So several methods were developed to improve the wave function and the energy.

2.1.2 Multi Reference Configuration Interaction (MRCI)

The MRCI method allows a better description of the electron correlation and is better suited for the characterization of excited states. The MRCI wave function is a linear combination of several determinants $\left|\Phi_i\right\rangle$, that are single or double excitations from preset reference determinants:

$$\Phi_j^{\text{MRCI}} = \sum_i c_{ij} \left|\Phi_i\right\rangle \tag{2.17}$$

The determinants $\left|\Phi_i\right\rangle$ in this methods are generated from optimized MOs of a previous HF calculation. The energy values E_j and the corresponding CI coefficients c_{ij} are obtained by solving the eigenvalue problem

$$\hat{H}_{\text{el}} \Phi_j^{\text{MRCI}} = E_j \Phi_j^{\text{MRCI}} \tag{2.18}$$

2.1.3 Complete Active Space Self Consistent Field (CASSCF)

The CASSCF method, like the MRCI method, describes the wave function not as a single slater determinant, but as a linear combination of slater determinants. They correspond to all possible excitations within a preset active space. More complex methods, like RAS (Restricted-Active-Space), reduce the number of allowed excitations to reduce computational effort in bigger systems. In contrast to the MRCI method not only the CI coefficients are varied, but in a coupled iterative process, also the MO coefficients of the orbitals ϕ_i, to minimize the expectation value of the energy. Contributions from excitations from electrons or in orbitals outside the active space are assumed to be negligible to the full energy of the system and are therefore not included. So the occupation of outside orbitals stays constant. The advantage over the MRCI method is that it also optimizes the molecular orbitals within the active space, even the virtual ones, as CAS molecular orbitals. So the CASSCF method also gives a good basis in MOs to describe the electronic wave function in addition to an energy value that takes electron correlation into account. The corresponding CAS wave function for the electronic system can be written analogous to the MRCI wave function in equation 2.17, but the determinants $\left|\Phi_i\right\rangle$ are constructed with the newly optimized CAS orbitals instead of the previous HF orbitals:

$$\Phi_j^{\text{CAS}} = \sum_i c_{ij} \left|\Phi_i\right\rangle \tag{2.19}$$

But this method is very expensive for large molecules and/or large active spaces.

2.2 Nuclear quantum dynamics on potential energy surfaces

The solution of the stationary Schrödinger equation 2.8 of the electrons for different nuclear geometries R gives the (multidimensional) potential energy surface (PES) $V_i(R) = E_{\text{el},i}(R)$. With the help of the

PES the Hamilton operator for the nuclei can be written as:

$$\begin{pmatrix} \hat{T}_{nuc} + \hat{V}_1 & 0 & \cdots & 0 \\ 0 & \hat{T}_{nuc} + \hat{V}_2 & \cdots & 0 \\ \vdots & \vdots & \ddots & \vdots \\ 0 & 0 & \cdots & \hat{T}_{nuc} + \hat{V}_n \end{pmatrix} \tag{2.20}$$

The potentials $V_i(R)$ act multiplicative upon the wave function $\chi_i(R)$ in the position space, while the kinetic operator $\hat{T}_{nuc}$ is not local. With an Fourier transformation the wave function χ_i can be converted from the position space to the momentum space, in which $\hat{T}_{nuc}$ can operate local upon χ_i. For a time independent Hamiltonian $\hat{H}$ the integration of equation 2.1 over the corresponding time interval results in the following time evolution of the system:

$$\chi(R,t) = e^{-i\hat{H}t}\chi(R,r,0) = \hat{U}(t)\chi(R,r,0). \tag{2.21}$$

2.2.1 Time dependent and time independent coupling in the system Hamiltonian

Adding a time dependent potential $\hat{V}(t)$ to the Hamiltonian, e.g. a laser pulse, results in a time dependent Operator. In this case equation 2.7 can be written with the dipole approximation as [70]

$$i\frac{\partial}{\partial t}\begin{pmatrix} \chi_1 \\ \chi_2 \\ \vdots \\ \chi_n \end{pmatrix} = \begin{pmatrix} \hat{T}_{nuc} + \hat{V}_1 - \mu_1(R)\epsilon(t) & -\mu_{1,2}(R)\epsilon(t) & \cdots & -\mu_{1,n}\epsilon(t) \\ -\mu_{1,2}(R)\epsilon(t) & \hat{T}_{nuc} + \hat{V}_2 - \mu_2(R)\epsilon(t) & \cdots & -\mu_{2,n}\epsilon(t) \\ \vdots & \vdots & \ddots & \vdots \\ -\mu_{1,n}(R)\epsilon(t) & \mu_{2,n}(R)\epsilon(t) & \cdots & \hat{T}_{nuc} + \hat{V}_n - \mu_n(R)\epsilon(t) \end{pmatrix}\begin{pmatrix} \chi_1 \\ \chi_2 \\ \vdots \\ \chi_n \end{pmatrix}. \tag{2.22}$$

$\hat{V}_i$ are the R dependent potentials of the i-th electronic state, $\mu_{i,j}(R)$ is the position dependent transition dipole moment between the i-th and j-th state, $\mu_i(R)$ is the dipole moment of the i-th state and $\epsilon(t)$ is the time dependent electrical field of the laser. If solving analytically the time step should be small enough to resolve the oscillation of the laser field. The result is the total nuclear wave function $\chi_{tot}(R,t)$ [70].

As an alternative or additionally the Hamiltonian can have a time independent coupling, for example a non-adiabatic coupling. In this case equation 2.7 can be written as:

$$i\frac{\partial}{\partial t}\begin{pmatrix} \chi_1 \\ \chi_2 \\ \vdots \\ \chi_n \end{pmatrix} = \begin{pmatrix} \hat{T}_{nuc} + \hat{V}_1 & K_{1,2}(R) & \cdots & K_{1,n} \\ -K_{1,2}(R) & \hat{T}_{nuc} + \hat{V}_2 & \cdots & K_{2,n} \\ \vdots & \vdots & \ddots & \vdots \\ -K_{1,n}(R) & -K_{2,n}(R) & \cdots & \hat{T}_{nuc} + \hat{V}_n \end{pmatrix}\begin{pmatrix} \chi_1 \\ \chi_2 \\ \vdots \\ \chi_n \end{pmatrix}. \tag{2.23}$$

In general a coupling (non diagonal elements in the Hamiltonian) allows a population transfer between the corresponding states. Thus the wave function χ_i is also dependent on all coupled wave functions χ_j.

2.2.2 Methods for solving the time-dependent Schrödinger equation

Considering a time dependent Hamilton operator $\hat{H}(t)$, for example including a time dependent coupling of potential, only over a small time step $\Delta t = \frac{t}{N}$, leads to the approximation that the Hamiltonian and accordingly the propagator $\hat{U}$ is constant for the duration of the time step [71].

$$\hat{U}(t) = \prod_{n=0}^{N-1}\left[\hat{U}((n+1)\Delta t, n\Delta t)\right]\hat{U}(t+\Delta t, t) = e^{-i\hat{H}(t)t} \tag{2.24}$$

The sum $\hat{H} = \hat{T} + \hat{V}$ in the exponent of equation 2.24 can not be divided into the product of two exponential functions, because the operators $\hat{T}$ and $\hat{V}$ are not commutative. This leads to the problem that

$$\hat{U}(\Delta t) = e^{-i\Delta t\hat{H}} = e^{-i\Delta t(\hat{T}+\hat{V})} \neq e^{-i\Delta t\hat{T}} e^{-i\Delta t\hat{V}}. \tag{2.25}$$

One approximation for the time evolution operator (equation 2.25) is the Chebychev-propagator [71], which approaches the exact propagator through a polynomial expansion with Chebychev-polynomials:

$$\hat{U}(\Delta t) = \sum_{Q} e^{-i\Delta t(\Delta E/2+V_{\text{min}})} a_Q \frac{\Delta E}{2} \Delta t C_Q(-i\hat{H}_{\text{norm}}). \tag{2.26}$$

Here is $\Delta E = V_{\text{max}} - V_{\text{min}}$. The expansion of the propagator $\hat{U}(\Delta t)$ works after scaling the Hamiltonian to the eigenvalue spectrum in the interval [-1;1]

$$\hat{H}_{\text{norm}} = \frac{\hat{H} - \hat{1}(\Delta E/2 + V_{\text{min}})}{\Delta E/2} \tag{2.27}$$

which is offset with the phase factor $e^{-i\Delta t(\Delta E/2+V_{\text{min}})}$. The Chebychev-polynomials are defined with the recursive relation

$$C_{Q+2} = C_Q - 2i\hat{H}_{\text{norm}} C_{Q+1} \tag{2.28}$$

with $C_0 = \hat{1}$ and $C_1 = -i\hat{H}_{\text{norm}}$. The Bessel-function a_Q converges in higher order Q to zero, which allows reasonable termination of the series expansion.

The advantage of the Chebychev-propagator is the error tolerance even with large time steps Δt. Therefore the choice of Δt is only restricted through the resolution of time dependent component, i.e. the oscillation of the laser pulse.

3 Tunnel ionization

One of the most fundamental processes of light matter interaction with strong laser fields is ionization [72, 73]. Because this leads to at least two charged particles, the electron and the remaining cation, which can respond to the same or additional electric and magnetic fields. The well known and easily to control interaction between the charged ions and the electromagnetic field allows to measure, detect and identify the mass, momentum and charge of the particle or fragments, in case of molecules [74]. This is a powerful tool to analyze the observed atom or molecule, either isolated or after an extended experiment, most likely involving one or more prior laser pulses in a pump-probe setup [12, 75]. But the ionization can also be the first step in an experiment to create or control the dynamics in the ionic species, to trap the ions, to generate a (localized) plasma, to further ionize the probe or to create attosecond laser pulses [76, 77]. For this variety of applications it is important to understand the ionization step.

Generally the investigated object, in most cases an atom or a molecule, but also a surface or a cluster, has a ionization energy, that is the energy needed to free the weakest bound electron of the system. Normally a laser would need a high enough frequency to provide this energy, as the freed electron is lifted to a continuum state the laser can also have an higher frequency, but an intense laser can overcome this in two different ways. The first is multi-photon ionization, where several photons combine their energy to excite the electron [78]. This process can be aided by naturally occurring electronic states, where the electron has the somewhat longer lifetime of the state to wait for another photon, or by virtual electronic states that only have very short lifetimes. The regime of multi-photon ionization is in general for high intensities, and therefore a high photon flux, of the laser field, especially if a high number of photons is needed for the ionization. Figure 3.1 highlights this case in the left panel, where multiple photons (red arrows) have enough energy to lift the electron (depicted as an electronic wave function in blue) outside the bound potential (black) of the, in this example, two atomic molecule. Another possibility for the strong-field laser to facilitate the electron leaving the bound states is via a process called tunnel ionization [63]. In this case the field bends the electronic potential in such a way that the outside continuum state is energetically equal and lower than the bound state and only separated by a finite barrier through which the electron can tunnel. The tunnel ionization is still dependent on the laser intensity, in order to bend the potential, but in most cases the requirements for the intensity are substantially lower for tunnel ionization than for multi-photon ionization. This is shown in figure 3.1 in the right panel, where the laser field (red) bends the undisturbed potential (black) to the potential with laser interaction (green). The electronic wave function (blue) can tunnel through the now small barrier along the blue arrow.

There are several studies for strong-field ionization in atoms, mostly focusing on the H atom or the noble gases [79]. In those cases the ionization process is so dominated by the outermost occupied atomic orbital, that angular dependent tunnel ionization can even be used to image these orbitals [80]. In contrast the multi-photon ionization couples with the continuum state and shows almost no angular dependence in photo electron emission spectra [81].

3.1 Small overview of theoretical descriptions of tunnel ionization

The theory of tunnel ionization in atoms is also well understood. While it is possible to solve the time dependent Schrödinger equation (TDSE), many approximations and models, like the strong-field approximation (SFA) [82], the Perelomov-Popov-Terent'ev model (PPT) [83] or the Ammosov-Delone-Krainov

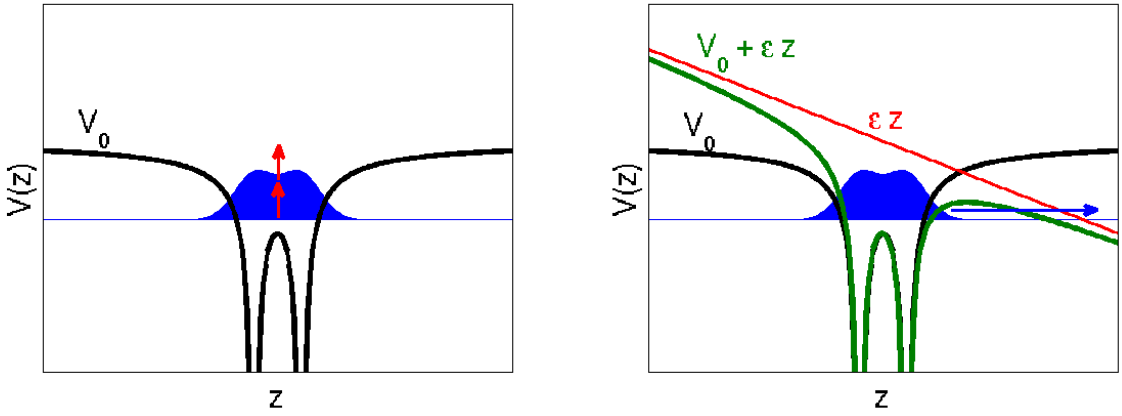

Figure 3.1: Schematic representation of a two atomic molecular potential (black) with a bound electron wave function (blue). The left panel shows the possibility of multi-photon ionization along the red arrows. The right panel depict how the laser field (red) can influence the potential to become bend (green potential), opening the way for the wave function to tunnel outside the barrier along the path of the blue arrow.

model (ADK) [84] show excellent agreement with TDSE and experiments in the tunneling regime and, PPT especially, also for the multi-photon regime.

The interaction of the external field with the barrier of the molecular potential leads to an electron flux $W(t)$, that can be used to calculate the ionization probability of a molecule in an electric field:

$$\begin{aligned} W(t) &= \int_S j(r,t)\,\mathrm{d}S \\ j(r,t) &= -\frac{i}{2}(\psi(r,t)\nabla\psi(r,t)^* - \psi(r,t)^*\nabla\psi(r,t)) \end{aligned} \tag{3.1}$$

Here $j(r,t)$ is the electron flux density, $\psi(r,t)$ is the electronic wave function in the presence of the electric field and r and t are the spacial and time coordinates of the electrons. For the surface S it is convenient to choose a plane perpendicular to the direction of the electric field. In our case, S is located at the outer turning points of the electronic wave function. Here, the wave function enters the classically-forbidden region where tunneling occurs. The basic premise of atomic tunneling theory is that the asymptotic electron wave function behaves as the asymptotic Coulomb wave functions, as the electrons sufficiently far away from the core only feel an effective Coulomb force. Reference [85] shows how to derive the ADK ionization rates (eq. 3.2) from these assumptions, with the field strength F, the ionization potential $I_p = \kappa^2/2$, the magnetic quantum number m, the azimuthal quantum number l, the nuclear charge Z and the normalization constant D, determined by matching the quantum mechanical wave function of the atom to the asymptotic Coulomb form.

$$W = D^2 \frac{2l+1}{2} \frac{(l+|m|)!}{(l-|m|)!} \frac{1}{2^{|m|}|m|!} \frac{1}{\kappa^{2Z/\kappa-1}} \left(\frac{2\kappa^3}{F}\right)^{2Z/\kappa-|m|-1} e^{-2\kappa^3/3F} \tag{3.2}$$

The main points from the formula is that ionization is slower for orbitals where the quantum number $m \neq 0$ and that lower lying states are vastly more unlikely to contribute as the ionization potential to the power of $3/2$ is part of a negative exponent. The PPT model improves upon the ADK model by including the frequency of the laser and the effect of the Coulomb field during ionization.

To adapt the ADK model for molecules (MO-ADK) [63] the molecular wave function was expanded as a superposition of spherical harmonics, which is in principle a very basic LCAO-MO (linear combination of atomic orbitals to molecular orbitals) ansatz with only one center. While for small molecules, especially linear or diatomic ones, the qualitative agreement for a similar modified MO-PPT is accept-

able [86], it is certainly not a promising prospect to scale the models for larger molecules. The accuracy of the TDSE is higher but the high computational cost is prohibiting the widespread use for larger molecules. Also some features of the angular tunnel ionization can only be explained by taking effects into account that are not present in the models. One point, as reported by [87], is the influence of dynamic exchange in strong field ionization. Especially in CO_2, where the peak ionization angle changes considerable. Another main point is that only the highest occupied molecular orbital (HOMO) is considered as the orbital responsible for the tunnel ionization. Later works that take neighboring orbitals into account, either statically or dynamically, have much better agreement with experimental measurements.

For polyatomic molecules, hydrocarbons in particular, it is not enough to look at the undisturbed orbitals, instead the field-dressed orbitals can have a profound effect on the ionization rates. This is especially true if the investigated molecule has low-lying Rydberg orbitals that can influence the character of the field-dressed orbitals. The quantum-mechanical ansatz from reference [88] already includes field-dressed orbitals and is scalable for larger molecules.

Going back to equation 3.1 using the electronic wave functions, evaluated by a quantum chemical program package, that are typically real, would yield their flux density as zero. Refs. [60, 88] demonstrated that this problem can be overcome by evaluating the electron flux for the electron density $\rho(r,t)$ with the help of the divergence theorem

$$\int_S j(r,t)\,\mathrm{d}S = \int_{V'} \nabla j(r,t)\,\mathrm{d}V' \tag{3.3}$$

and the continuity equation, as proposed by [89]

$$\frac{\mathrm{d}}{\mathrm{d}t}\rho(r,t) = -\nabla j(r,t) \tag{3.4}$$

equation 3.1 can be rewritten as

$$W(t) = -\int_{V'} \nabla j(r,t)\,\mathrm{d}V' = \frac{\mathrm{d}}{\mathrm{d}t}\rho(r,t)\,\mathrm{d}V' \tag{3.5}$$

with V' being the part of the total volume V in which the electronic wave function $\psi(r)$ is defined and which is spanned by the surface S and a vector perpendicular to S pointing away from the nuclei. In order to calculate the tunneling probability $T(S)$, we need the electron density with (at final time t_f) and without the external field (at initial time t_i). Therefore Eqn. 3.5 is integrated over time to obtain the following:

$$T(S) = \int_{V'} \rho(r,t_f)\,\mathrm{d}V' - \int_{V'} \rho(r,t_i)\,\mathrm{d}V' \tag{3.6}$$

This equation stays in the quasi-static approximation and allows to calculate the tunnel probability $T(S)$ through a surface S numerically, with the necessary wave functions on a three dimensional grid given by quantum chemical calculations with and without the external field. The dipole field can be added to the one electron Hamiltonian in the quantum chemical calculation. This will lead to a set of field dressed orbitals. Changing the relative angle between the field and the molecule allows to calculate the angle dependent tunnel ionization rate. This approach can utilize the full quantum chemical theory (see section 2.1) for approximations, optimizations and electron correlation. A multi configuration calculation (see sections 2.1.2 or 2.1.3) will also give the coefficients for a linear combination of molecular orbitals, that become partially occupied under the influence of the field, to allow a coherent ionization from multiple orbitals. References [88, 90] show that this method has a much better agreement with experimental measurements when compared to the MO-ADK. For the examples in the following sections (3.2 and 3.3) the density $\rho(r,t)$ is calculated numerically for a three dimensional Cartesian grid.

3.2 Angular dependent tunnel ionization in small hydrocarbons

The first test cases for this approach were diatomic molecules [88], that compared favorably to experimental measurements and other theoretical models. So the next step was to expand to polyatomic molecules, in this case for the series acetylene (C_2H_2), ethylene (C_2H_4) and ethane (C_2H_6) as well as for the bigger molecule cyclohexadien (CHD) and its substituted derivates α-terpinene (AT) and α-phellandrene (AP). Acetylene is still linear, but the other molecules have an additional rotation that needs to be considered when comparing theory and experiment. In the experiment the relative angle between laser polarization and signal is measured and this is not sensitive to a rotation of the fragment along the signal direction, so in the theory this rotation is averaged as there is no indication of preference.

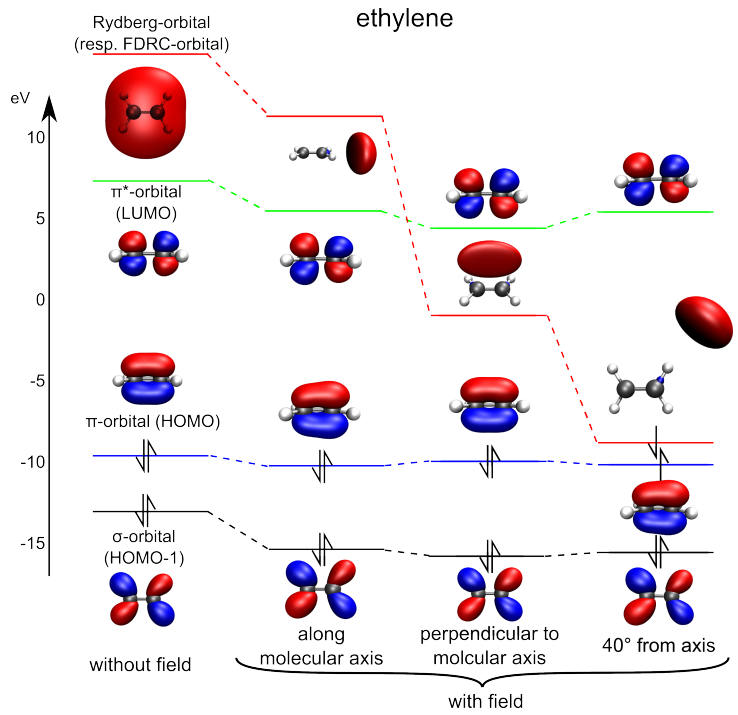

Figure 3.2: Ethylene orbitals calculated on the CASSCF[12,12] level of theory using the 6-31++G** basis set with various orientations of the laser polarization for an intensity of $9 \cdot 10^{13}\mathrm{Wcm}^{-2}$ and without field. The leftmost column shows the undisturbed orbitals and the other field dressed orbitals. The most notable difference occurs in the FDRC orbital, that is a Rydberg orbital in the field free case. The electron density moves with the dipole field and its energy changes drastically depending on the orientation. When the polarization lies along the C-H bond the energy gap between HOMO and FDRC orbital is small enough that partial occupation of the FDRC orbital occurs, which increases the ionization rate in that direction.

In all investigated hydrocarbons, a field dressed orbital with Rydberg character (FDRC orbital) was stabilized through the intense laser field, especially if the laser polarization points at or near a C-H bond. The resulting orbitals, with and without field, for ethylene (C_2H_4) are shown in figure 3.2. The leftmost column shows the undisturbed orbitals and the other field dressed orbitals. The most notable difference occurs in the FDRC orbital, that is a Rydberg orbital in the field free case. The electron density moves with the dipole field and its energy changes drastically depending on the orientation. When the energy difference between the HOMO and the FDRC orbital became small enough, then the FDRC orbital was partially occupied in the multi configuration representation of the electronic wave function, this is the case for the rightmost column in figure 3.2. While the general form of the FDRC orbital is already visible in the virtual orbitals of a HF calculation, the further optimization of the orbital in the CASSCF step brings the orbital energy close to the HOMO and allows for partial occupation in the CASSCF wave function. This partial occupation leads to a higher tunnel ionization rate, because the FDRC orbital is more pliable and as the corresponding electron density is farer away from the nuclei it is easier to tunnel

through the remaining barrier. If the HOMO had π character lower intensities were necessary for a small energy gap, which is a prerequisite for partial occupation, between the HOMO and the FDRC orbital, than for HOMOs with σ character. This effect can be seen in the different influence of the FDRC orbital in ethane, that does not have π orbitals, and acetylene and ethylene, that have π orbitals. Experimental details, figures of the important orbitals and the angular dependent tunnel ionization rates are explained in the manuscript “The importance of Rydberg orbitals in dissociative ionization of small hydrocarbon molecules in intense few-cycle laser pulses”, which is printed hereafter.

The importance of Rydberg orbitals in dissociative ionization of small hydrocarbon molecules in intense few-cycle laser pulses

Bethany Jochim[1], R. Siemering[2], M. Zohrabi[1], A. Voznyuk[3], J. B. Mahowald[3], D. G. Schmitz[3],
K. J. Betsch[1], Ben Berry[1], T. Severt[1], Nora G. Kling[1,4], T. G. Burwitz[3], K. D. Carnes[1], M. F. Kling[1,4] ,
I. Ben-Itzhak[1], E. Wells[3], and R. de Vivie-Riedle[2]

Much of our intuition about strong-field processes is built upon studies of diatomic molecules, which typically have electronic states that are relatively well separated in energy. In polyatomic molecules, however, the electronic states are closer together, leading to more complex interactions. A combined experimental and theoretical investigation of strong-field ionization followed by hydrogen elimination in the hydrocarbon series C_2D_2, C_2D_4 and C_2D_6 reveals that the photofragment angular distributions can only be understood when the field-dressed orbitals rather than the field-free orbitals are considered. Our measured angular distributions and intensity dependence show that these field-dressed orbitals can have strong Rydberg character for certain orientations of the molecule relative to the laser polarization and that they may contribute significantly to the hydrogen elimination dissociative ionization yield. These findings suggest that Rydberg contributions to field-dressed orbitals should be routinely considered when studying polyatomic molecules in intense laser fields. This improved understanding of the links between photofragment images and the electronic dynamics in the molecule can enhance efforts at image-based strong-field coherent control.

[1] J.R. Macdonald Laboratory, Department of Physics, Kansas State University, Manhattan, KS 66506 USA
[2] Department für Chemie, Ludwig-Maximilians-Universität München, Butenandt-Strasse 11, D-81377 München, Germany.
[3] Department of Physics, Augustana University, Sioux Falls, SD 57197 USA
[4] Department für Physik, Ludwig-Maximilians-Universität München, Am Coulombwall 1, D-85748 Garching, Germany
Correspondence and requests for materials should be addressed to E. W. (email: eric.wells@augie.edu) or R. de V-R. (email: Regina.de_Vivie@cup.uni-muenchen.de)

Strong-field ionization is a key topic in ultrafast science since it is an essential step in attosecond pulse generation [1-5], serves as a probe of electronic and nuclear dynamics [6-13] and is used to image molecular orbitals [14-17]. Continued development of our understanding of ionization dynamics in molecular systems [18] is an important aspect of forefront experimental challenges such as controlling molecular fragmentation dynamics [19-22], the creation of multi-hole electronic wave packets [23-27] and the drive for ever finer time-resolved measurements of molecular dynamics [28-29] that one day may, for example, probe charge migration [30-33] on intrinsic timescales.

Strong-field ionization is well studied in atoms [34-41], in the benchmark H_2 molecule [42-47] and in somewhat more complex systems [48-50]. This work has informed our understanding of many characteristic strong-field processes, such as tunnel ionization, above-threshold ionization and high harmonic generation. Since the electronic states in atomic systems are generally well-separated, in many cases the behavior of the outermost occupied orbitals approximately characterize the entire process. As strong-field ionization experiments moved to diatomic molecules, however, the electronic behavior became more complex. Unlike in atomic cases, a simple ionization potential could no longer adequately characterize the relative tunneling rates [48,51-55]. Subsequent work has included examples of diatomics (CO, N_2, HCl) [26,56-58] where several orbitals participate in the tunneling process. These studies and other recent efforts exploring strong-field molecular ionization of multi-electron systems [56-68] suggest that a full understanding of the ionization process and associated angular structure requires consideration of not just the highest occupied molecular orbital (HOMO) but also the neighboring HOMO-1. In this study we show that also formerly unoccupied molecular orbitals should be taken into account in strong field ionization already for small hydrocarbon molecules.

Polyatomic molecules are now the focus of many strong-field ionization experiments since these molecules are important in a variety of settings, such as the building blocks in molecular machines, in quantum information applications, for energy storage and structural classification of proteins. These experiments offer opportunities to test imaging techniques [69-71] and explore and control dynamics [60,64,72] in more complicated molecular systems. The polyatomic nature of the system does not change the foundational role of strong-field ionization in ultrafast processes, but the ionization dynamics become increasingly complex. Mechanisms such as Freeman resonances [73] and laser-induced AC Stark shifts result in more complicated behavior as the number and proximity of electronic states increase. Of particular interest in this work is the strong-field driven modification of the molecular orbitals, which becomes relatively more important as the number and angular complexity of the molecular orbitals increase and the energetic separation of the field-free orbitals decreases. Common theoretical practice uses only the field-free orbitals to describe ionization, but as recently shown for strong field

ionization for excited cyclohexadiene and its derivates, the field-dressed orbitals can have altered spatial characteristics [74] and a significant amount of Rydberg character, which leads to high ionization rates. In this article, we present a series of measurements that illustrate that these Rydberg contributions also play an important role in the strong-field ionization of small hydrocarbon molecules starting from their electronic groundstate.

Results

We focus on a specific process initiated by intense few-cycle laser pulses in acetylene (C_2D_2), ethylene (C_2D_4), and ethane (C_2D_6), namely single ionization of the parent molecule followed by hydrogen elimination. In each case, we measure the momentum of the remaining $C_2D_{n-1}^+$ fragment using velocity map imaging (VMI) [75]. We are assured that this fragmentation channel is uniquely identified as neutral hydrogen elimination by the lack of any momentum-matching D^+ partner ions obtained under the same laser conditions, therefore excluding contributions from the $D^+ + C_2D_{n-1}^+$ channel. The short pulse duration (approximately 5 fs) limits any possibility for significant vibration or rotation of the nuclei while the laser pulse is present [18,76] and avoids molecular dynamics such as internal conversion that sometimes occur on excited states of the neutral molecule via multiphoton resonances [77-79]. Thus, the measured $C_2D_{n-1}^+$ fragment angular distributions can represent the angle-dependent ionization probability. In the ethylene case, the general four-lobed structure shown in Fig. 1(a) and (b) for the $C_2D_3^+$ photofragments is independent of pulse intensity and duration (at least up to ≈45 fs [72]).

The comparison between measured and calculated $C_2D_3^+$ photofragment angular distributions from ethylene, shown in Fig. 1, clearly illustrates the need to include Rydberg contributions from field-dressed orbitals if the calculations are to even approximate the experimental result. Calculations (detailed in the Discussion and Methods sections) that do not include ionization from field-dressed orbitals with Rydberg character (called FDRC orbitals from now on) result in an approximately isotropic angular distribution, like the one shown in Fig. 1(c). Here the tunnel ionization is considered only from the HOMO. Including ionization from FDRC orbitals yields the four-lobed structure illustrated in Fig. 1(d), which qualitatively matches the experimental results.

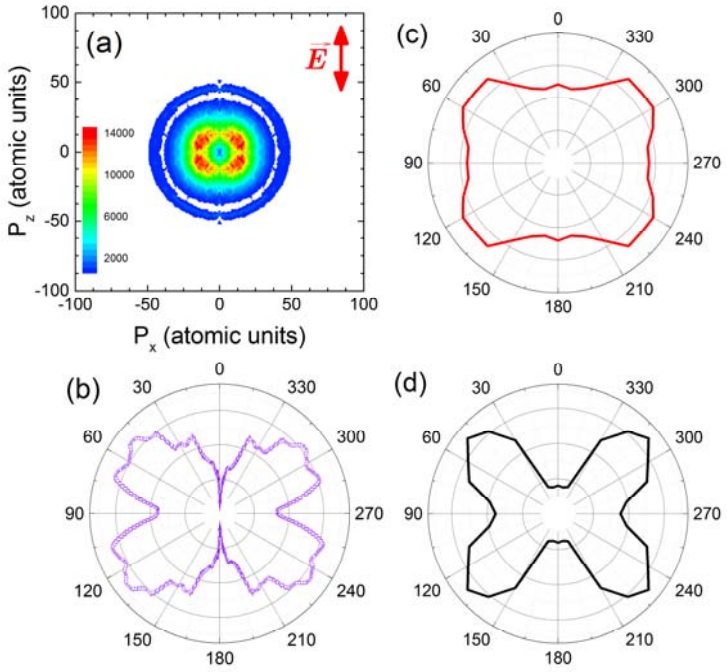

Figure 1: (a) The two-dimensional slice ($P_y \approx 0$) through the three-dimensional momentum distribution obtained from VMI data of $C_2D_3^+$ photofragments produced in the $n\omega + C_2D_4 \rightarrow C_2D_4^+ \rightarrow C_2D_3^+ + D$ process. The laser polarization, indicated by the arrow, is vertical (0-180°) in all panels. The faint outer ring is mirrored in the D^+ momentum image, suggesting that those ions are part of the double ionization process ($D^+ + C_2D_3^+$). The laser pulses are approximately 5 fs in duration with a central wavelength of 740 nm and a focused intensity of approximately $6x10^{14}$ W cm^{-2}. (b) Measured yield as a function of the relative angle between the $C_2D_3^+$ photofragment and the laser polarization. The yield is obtained for the inner single ionization followed by hydrogen elimination process and excludes the faint outer double ionization process. (c) Calculated angular distribution for the $C_2D_3^+$ photofragments (see Methods for details) without including FDRC orbitals, for an intensity of $9x10^{13}$ W cm^{-2}. (d) Similar calculations but with the ionization from FDRC orbitals included, for an intensity of $9x10^{13}$ W cm^{-2}.

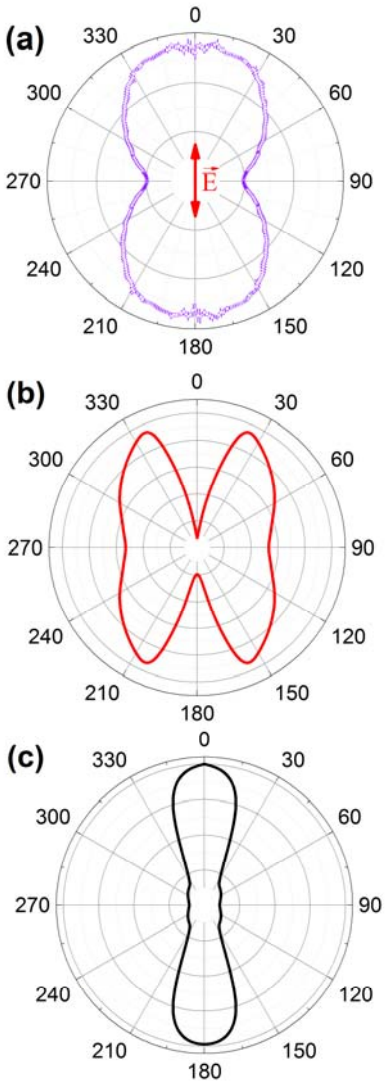

Figure 2: (a) Experimental C_2D^+ photofragment angular distributions arising from nω + C_2D_2 → $C_2D_2^+$ → C_2D^+ + D. Experimental laser parameters are about 5 fs and 8x10^{15} W cm^{-2}. The laser polarization is vertical (along the 0-180° direction) in all panels, as indicated by the arrow. (b) Calculated angular distribution for the C_2D^+ photofragments (see Methods for details) without including FDRC orbitals, for an intensity of 9x10^{13} W cm^{-2}. (c) Similar calculations but with the ionization from FDRC orbitals included, for an intensity of 9x10^{13} W cm^{-2}.

Similar calculations to those performed for ethylene were conducted for the hydrogen elimination channels in acetylene and ethane, nω + C_2D_2→ $C_2D_2^+$ → C_2D^+ + D and n□ + C_2D_6 → $C_2D_6^+$ → $C_2D_5^+$ + D, respectively. The comparison between the calculations and the experimental results, shown in Figures 2 and 3, again demonstrates the influence of the FDRC orbitals on the angle-resolved ionization yield. As in the ethylene

case, the experimental results from acetylene, shown in Figure 2(a), are qualitatively different than the calculations shown in Figure 2(b) taking into account only the HOMO. While the experimental angular distribution is less strongly peaked around the polarization direction than the calculation also including the FDRC orbitals (shown in Figure 2(c)), it does share the dominant feature of the ionization along the polarization axis.

The experimental and theoretical results for ethane molecules are shown in Figure 3. Due to ethane's energy level structure, the observed intensity-dependent angular distribution shown in Figure 3 is expected. The four lobes observed at higher intensity (Figure 3(b)) are due to the "turn on" of contributions to the ionization from the FDRC orbitals. This dependence is reproduced by our calculations (Figs. 3(c) and (d)) and described further in the Discussion section. Clearly, the angle-resolved ionization from all three of these small hydrocarbon molecules show significant effects due to contributions from the FDRC orbitals that are populated in intense, few-cycle laser pulses.

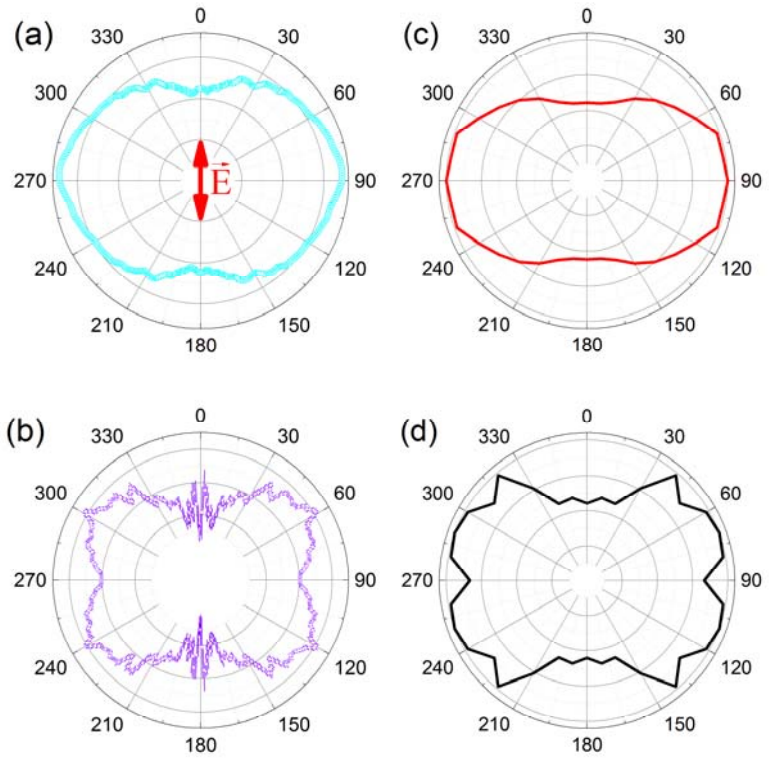

Figure 3: (a) Measured $C_2D_5^+$ photofragment angular distribution from the nω + $C_2D_6 \rightarrow C_2D_6^+ \rightarrow C_2D_5^+ + D$ process at a peak laser intensity of about 2 10^{15} W cm^{-2} and a pulse duration of about 5 fs. (b) Measured $C_2D_5^+$ photofragment angular distribution for the same process and pulse duration but at a higher intensity of approximately 7x10^{15} W cm^{-2}. (c) Calculated $C_2D_5^+$ angular distribution without including FDRC orbitals, for an intensity of 9x10^{13} W cm^{-2}. (d) Calculated $C_2D_5^+$ angular distribution once the FDRC orbitals are included, for an intensity of 2x10^{15} W cm^{-2}. The laser polarization, indicated by the red arrow in (a), is vertical in all panels.

Discussion

The angle-dependent ionization probabilities for ethylene, acetylene and ethane shown in Figs. 1-3 are calculated based upon electronic structure theory including the laser field as an external dipole field in the Hamiltonian, as detailed in reference [68]. The neutral molecules in our effusive jet are randomly oriented, and thus the interaction between the laser field and the electronic wavefunction depends on their angle relative to the laser polarization. In the calculations, therefore, the molecule is rotated in the plane formed by laser polarization and the C=C bond, as well as out of the plane, i.e., around the C=C bond axis. For each position, the electronic wavefunction is calculated in the presence of the electric field and the tunneling probability is deduced for various orbitals. Coherent ionization from multiple orbitals is treated using a linear combination of the selected orbitals, as described in [68].

As illustrated in Figure 4, the σ-, the π- and the π* orbitals do not change significantly either in shape or in energy under the influence of the laser field. In contrast, the orbital with Rydberg character reacts strongly to the applied field. Its shape aligns with the direction of the laser field, and its orbital energy strongly depends on the laser polarization. For polarization parallel or perpendicular to the C=C backbone, the orbital energy is lowered, but the HOMO and the FDRC orbital remain well separated in energy. When the laser polarization is aligned with the C-H bond direction, however, the energy gap between these orbitals decreases significantly. These calculations indicate that the field stabilizes a high-lying Rydberg orbital with a localized electron density in the direction of the laser polarization. For these orientations of the molecule relative to the laser polarization, the stabilization of the Rydberg orbital is so large that it becomes energetically close to the field-dressed π orbital (HOMO), leading to partial occupation of the FDRC orbital in the laser field. The electron density is far from the nuclei and the tunneling ionization rate becomes relatively large.

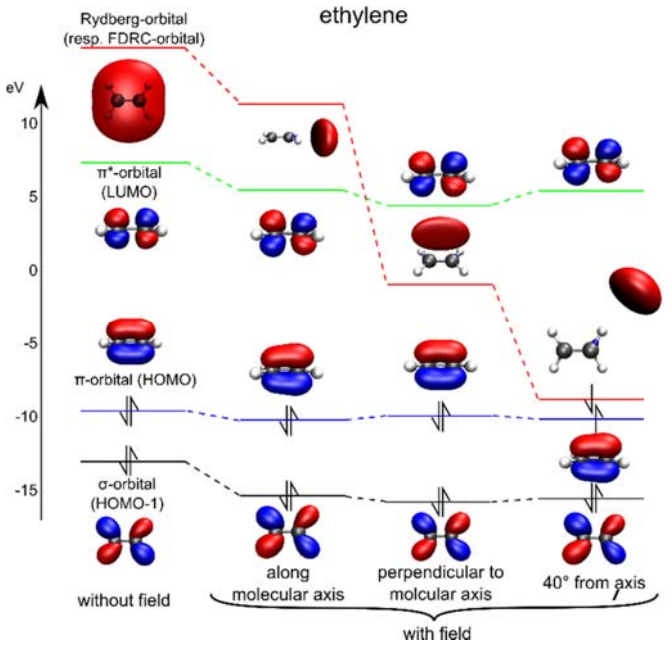

Figure 4: Ethylene orbitals for various orientations of the laser polarization, for an intensity of 9×10^{13} W cm^{-2}. The rightmost column shows the case where the laser polarization lies along the C-H bond direction. In this configuration, the field easily shifts electron density in that direction and the ionization rate correspondingly increases.

The calculated angular-dependent tunnel ionization only describes the electron leaving the system, while the experimental measurement is the photofragment from a C-H dissociation. To compare the theoretical calculations with the experimental results, we need to calculate the C-H bond dissociation direction related to the angular-dependent ionization rate. For the smallest molecule C_2H_2, the correlation between the detected C2H+ fragment and the angular-dependent ionization rate is simple, as this molecule is linear. If for example the molecule is rotated by an angle α in respect to the laser polarization and its ionization leads to a C-H bond break, the detected signal will be at the angle α (or 180° + α). The rotation of the molecule is about 1000 times slower than the vibration correlated with the dissociation and does not influence the shape of the angular distribution of the fragments. Thus the angular distribution is the same for the electron leaving the system as for the hydrogen or the counter ion leaving the system.

For the other two non-linear molecules with more than two H-atoms attached, the case is more complex. So we introduce a mapping of the tunnel ionization to the photofragment dissociation direction. In our calculations we use the C-C axis to determine the position of the molecule relative to the laser.

In calculating the angular distributions for hydrogen elimination in C_2H_4, we have explored three possible dissociative ionization scenarios, which are illustrated in Figure 5(a)-(c). In all scenarios tunnel ionization creates an electronic wavepacket with a hole localized along the two C-H bonds that align most closely with the laser field (“nearby” C-H bonds). The three scenarios differ in the degree of influence the localized wavepacket has for preferential C-H bond breaking.

In the first scenario, the tunnel ionization probability is largest when a C-H bond is aligned along the laser polarization. This situation leads to subsequent dissociation of these nearby C-H bonds. In this scenario, the hole is not allowed to evolve from its birthplace along the direction of the laser field and it is assumed that the nearby bonds break and not the other C-H bonds. In this scenario the localized wavepacket has a great influence in selecting possible C-H bond breaks. As can be seen in Figure 5(a), the theoretical photofragment distribution for this scenario displays a four-lobed structure similar to that observed in the experimental data. This scenario, however, as expected, yields zero ionization for 60°−120° and 240°−300°, as these angles do not correspond to the C-H bonds being near the laser polarization.

In the second scenario the electronic wavepacket delocalizes almost instantaneously and all C-H bonds dissociate with the same probability. In this scenario the former localized wavepacket has no influence for selective C-H bond breaking. Figure 5(b) shows the predicted angular distribution for this scenario. The yields at 90° and 270° come from dissociation of the C-H bonds farthest from the polarization axis of the laser

field, while the smaller contributions at angles of 45°, 135°, 225° and 315° are due to dissociation of the nearby C-H bonds.

As in the aforementioned cases, the final scenario, illustrated in Figure 5(c), dictates that the probability of hole creation is favored for the nearby C-H bonds, but here the photofragment yield contributions from various sites are weighted by their “distance” to the laser field. In this sense this scenario is a middle ground between scenario one and two. The localized electronic wavepacket influences the selection of which C-H bond breaks, in contrast to scenario two, but not as exclusively as in scenario one. This distance is indicated by the dotted green lines in Figure 5(c). Hence, while the nearby C-H bonds are most likely to break, the other C-H bonds have a much smaller but non-zero probability of breaking as well, thus leading to the yields at 60°−120° and 240°−300°, seen in Figure 5(c), which were absent in scenario 1. The final scenario best matches the experimental result, and its underlying idea is supported by the time-dependent propagation of the hole in the electronic density, shown in Figure 6. The electron hole density (after ionization) is demonstrated to spend the most time in the vicinity of the nearby C-H bonds within the first vibrational period of about 10 fs (the vibration is not shown). An animation of the electron hole density for the first 10 fs after ionization is available as supplemental information to this article. A similar strategy was applied to the ethane case in order to obtain the photofragment emission angular-distributions.

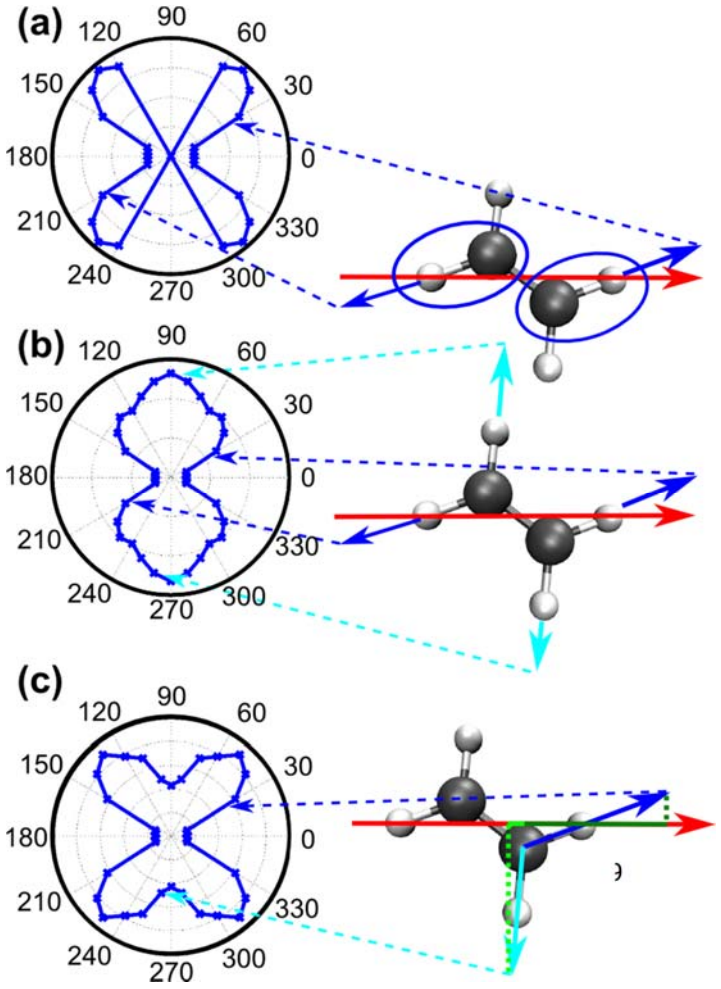

Figure 5: Schemes for calculating the photofragment angular distributions in C_2D_4 (right) and corresponding results (polar plots, left). The red arrow indicates the direction of the dipole field. The dashed arrows relate the orientation of the molecule to the dipole vector with the angle between the field and the dissociation direction plotted in the polar diagram. (a) Contributions from the hole localized at “nearby” C-H bonds only. The blue vector indicates the dissociation direction of these H-atoms. (b) The hole delocalizes quickly, allowing all C-H bonds to dissociate with equal probability. The cyan vector indicates the dissociation direction of the more remote H-atoms (c) Contributions to dissociative ionization yield are weighted partially by their projection to the dipole vector which is indicated by the dark and light green line, respectively (see eq. (4)). The individual projections are indicated as dotted lines.

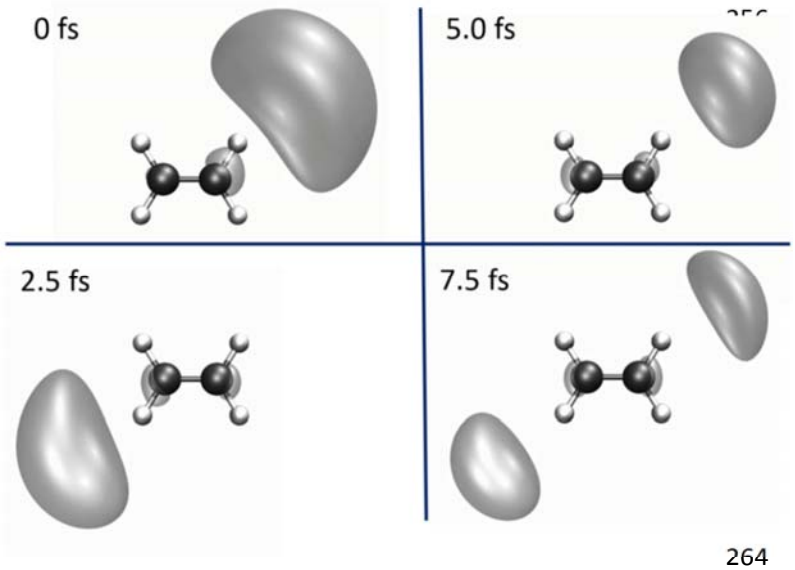

Figure 6: Snapshots of the time-dependent hole density in ethylene. The complete animation produced in the calculation is included in the supplemental information.

As shown in Figures 2 and 3, the FDRC orbitals make an important contribution to the dissociative ionization in acetylene and ethane. Ethane in particular provides an interesting energetic contrast to ethylene. The energy gap separating the HOMO and the FDRC orbitals in ethane is larger than that in ethylene. Consequently, in ethylene, the FDRC orbitals are expected to be populated and contribute significantly to the ionization yield at lower laser intensities, while in ethane this situation is expected to be realized only above a certain intensity. This idea is supported by Figure 7, which shows the intensity-dependent energies of the field-dressed HOMO and the FDRC orbitals of ethane. With increasing intensity the orbitals come close in energy and eventually cross. The intensity at which the FDRC-orbitals in ethane should become relevant is at around 3×10^{15} W/cm^2, consistent with the experimental results illustrated in Fig. 3.

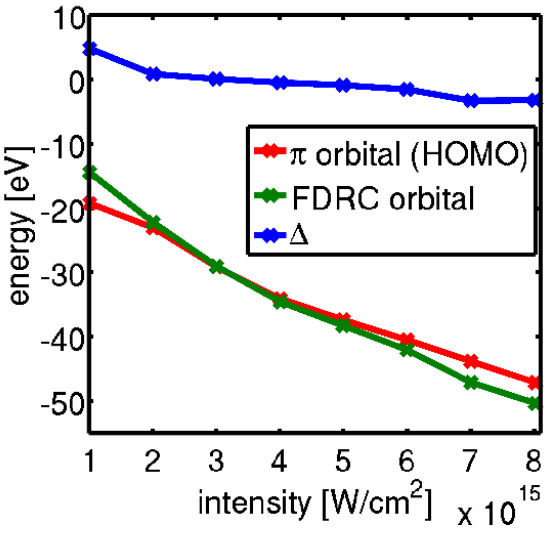

Figure 7: Intensity-dependent energies of the HOMO and the FDRC orbitals in ethane. The laser polarization is along a C-H bond for the most noticeable effect. Δ represents the difference in energy between these orbitals as a function of intensity.

Collectively, these results provide robust evidence of the important role played by field-dressed orbitals with Rydberg character in strong-field ionization of molecules where the energy separation between the HOMO and the FDRC-orbitals is comparable to the Stark shift provided by the laser. These conditions are satisfied in the hydrocarbon molecules studied here and should be relevant for large classes of polyatomic molecules that are attracting increasing experimental interest. Ionization from these field-dressed orbitals with Rydberg character creates holes in the electronic wavefunction that strongly influence the direction of the hydrogen elimination from the molecular cation. Understanding the link between the electronic properties of the ionization process and the photofragment angular distributions that result from molecular dissociation is an essential component of designing adaptive control schemes that use photofragment imaging as a feedback source. It should be noted, that the involvement of the FDRC-orbitals is a property of the (studied) hydrocarbons and not present in simpler diatomic molecules like CO, although the necessary basis functions to form FDRC-orbitals were available in previous calculations [68].

Methods

Calculations: We performed quantum chemical calculations for the ground state with the MOLPRO program package [80] at the CASSCF[10,12], CASSCF[12,12] and CASSCF[14,12] level of theory, for acetylene, ethylene and ethane respectively using the 6-31++G** basis set. The calculations were carried out with and without an external dipole field. The dipole field was added to the one-electron Hamiltonian to simulate the interaction with the strong ionization field, which corresponds to a static field.

The ionization probability of a molecule in a laser field can be modeled in terms of the induced electron flux through the barrier of the combined molecular and external electric field [79] (atomic units m = ħ = e = 1 are used throughout the paper):

$$W(t) = \int_S j(r,t)\, dS,$$

$$j(r,t) = -\frac{i}{2}\left(\psi(r,t)\nabla\psi(r,t)^* - \psi(r,t)^*\nabla\psi(r,t)\right) \quad (1)$$

Here *j(r,t)* is the electron flux density and *ψ(r,t)* is the electronic wavefunction in the presence of the electric field inducing the electron flux *W(t)*. For the surface *S* it is convenient to choose a plane perpendicular to the direction of the electric field. In our case, *S* is located at the outer turning points of the electronic wavefunction. Here the wavefunction enters the classically-forbidden region where tunneling occurs. The electronic wavefunctions, evaluated by a quantum chemical program package, are typically real, and their flux density (Eq. 1) is zero.

Refs. [68, 81] demonstrated that this problem can be overcome by evaluating the electron flux for the electron density *ρ(r,t)* with the help of the divergence theorem and the continuity equation, as proposed by [81].

We can then rewrite eq. (1) as:

$$W(t) = -\int_{V'} \nabla j(r,t)\, dV' = \frac{d}{dt}\int_{V'} \rho(r,t)\, dV' \quad (2)$$

with V' being the part of the total volume V in which the electronic wavefunction $\psi(r)$ is defined and which is spanned by the surface S and a vector perpendicular to S pointing away from the nuclei. In order to calculate the tunneling probability $T(S)$, we need the electron density with (at final time t_f) and without the external field (at initial time t_i).

Therefore we integrate Eqn. 2 over time and obtain the following:

$$T(t;S) = \int_{V'} \rho(r,t_f)\, dV' - \int_{V'} \rho(r,t_i)\, dV' \quad (3)$$

To treat ionization from more than one single orbital we solve the working equations derived above for a linear combination of the selected molecular orbitals. This implies a basis transformation rewriting the two orbitals (e.g. HOMO and LUMO) in the Slater determinant as the orbitals HOMO + LUMO and HOMO - LUMO, allowing for coherent ionization of the electron from both orbitals [60,82]. The coefficients for the linear combination are taken from the CASSCF calculations and correspond to the coefficients of the configuration expansion of the groundstate electronic wavefunction.

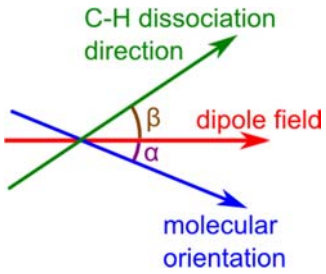

Figure 8: Relevant angles α, between the dipole field and the molecular orientation (in this case the C-C axis) and β, between the dipole field and the C-H dissociation direction.

The position of the molecules relative to the dipole field is given by a rotation φ along the C-C axis and a rotation α perpendicular to the C-C axis. Both rotations were varied in 10° steps. The resulting tunnel ionization $T(\alpha)$ is obtained from Eqn. 3 by integrating over the angle φ, as the surface S can be written depending on the angles α and φ. For the mapping step from angular tunnel ionization $T(\alpha)$ to the calculated angular H^+ fragment signal $U(\beta)$ where β describes the angle between the dipole field and the C-H dissociation direction as shown in Fig. 8, we used the following formula:

$$U(\beta) = \sum_{\alpha} T(\alpha) \cdot M(\alpha, \beta) \cdot w(\alpha, \beta), \quad (4)$$

with $M(\alpha, \beta)$, the mapping function and $w(\alpha, \beta)$ a weight for the "distance" between the C-H bond and the dipole field. The mapping function is one if β coincides with a C-H bond for a given angle α and zero otherwise. The weight was set to $w(\alpha, \beta) = 0.5\left(1 + \frac{\langle \vec{V} | \vec{D} \rangle}{|\vec{V}||\vec{D}|}\right)$, where $\vec{V}$ is the vector along the dissociation direction shown as the blue (and cyan) vectors in Figure 5 (c) and $\vec{D}$ is the vector of the dipole field.

The tunnel ionization creates a hole in the electron density in the FDRC orbital. This orbital is taken to represent the hole. To visualize the hole dynamics, the FDRC orbital is projected onto the basis of the field free orbitals. This projected hole is treated like an electronic wavepacket and propagated in the eigenstate basis.

Experiment: A Ti:Sapphire laser system generates 2 mJ pulses of approximately 24 fs duration and 790 nm central wavelength at 10 kHz. These pulses are used to generate few-cycle pulses (~200 μJ, 450-1000 nm bandwidth) through self-phase modulation in an argon-filled hollow-core fiber. A set of chirped mirrors compensates for substantial up-chirp acquired during spectral broadening and creates an overall negative dispersion to counterbalance positive dispersion from propagation through air and glass in the beam path. Moreover, a pair of fused silica wedges allows for fine adjustment of the dispersion. These procedures allow delivery of Fourier transform-limited pulses of about 5 fs duration on target. A small fraction of the laser beam is split off and focused into a stereographic above-threshold ionization (ATI) phase meter [83,84]. Using the phase meter to obtain a parametric asymmetry plot of the expected radius verifies the production of few-cycle pulses [85]. The main portion of the laser beam travels to the velocity map imaging (VMI) [86,87] spectrometer and is focused by an *f*=75 mm spherical mirror inside the chamber. An iris placed just before the entrance is used to vary the peak laser intensity, which is evaluated approximately using simple Gaussian beam optics.

Our VMI spectrometer follows well-documented design and operation, e.g., [75,88]. An effusive gas jet of the target hydrocarbon molecules intersects the laser beam inside the spectrometer, which is composed of an electrostatic lens system that focuses photofragments to specific radii on the detector depending upon their transverse momenta. Using a fast high voltage switch, the detector is active during a narrow time window (80-100 ns) around the expected arrival time of the fragment of interest. Deuterated hydrocarbon gas is used to ensure adequate time separation of fragments differing by only one "hydrogen" atom. The obtained images are inverted offline using a

379 version of the onion-peeling method [75,89] to retrieve the two-dimensional slice (Py ≈
380 0) through the three-dimensional momentum distribution of the dissociating fragments.

381

References

1. Agostini, P. and DiMauro, L.F. The Physics of Attosecond Light Pulses, *Reports on Progress in Physics* **67**, 813 (2004). DOI: http://dx.doi.org/10.1088/0034-4885/67/6/R01
2. Krausz, F. and Ivanov, M. Attosecond physics, *Rev. Mod. Phys*. **81**, 163 (2009). DOI: http://dx.doi.org/10.1103/RevModPhys.81.163
3. Chang, Z. *Fundamentals of attosecond optics* (CRC Press, Boca Raton, 2011).
4. Kienberger, R., Chang, Z., and Hee Nam, C. 10th anniversary of attosecond pulses, *J. Phys. B. At. Mol. Opt. Phys*. 45, 070201 (2012). DOI: http://dx.doi.org/10.1088/0953-4075/45/7/070201
5. Corkum, P.B. in *Attosecond Physics* (Springer-Verlag, Berlin, 2013), pp. 3-7. DOI: http://dx.doi.org/10.1007/978-3-642-37623-8_1
6. Li, W. Jaroń-Becker, A.A., Hogle, C.W., Sharma, V., Zhou, X., Becker, A., Kapteyn, H.C. and Murnane, M.M. Visualizing electron rearrangement in space and time during the transition from a molecule to atoms, *Proc. Nat. Acad. Sci*. **107**, 20219 (2010). DOI: doi:10.1073/pnas.1014723107
7. Zewail, A. H. Femtochemistry: Atomic-Scale Dynamics of the Chemical Bond Using Ultrafast Lasers (Nobel Lecture). *Angew. Chem. Int. Ed*. **39**, 2586–2631 (2000). DOI: 10.1002/1521-3773(20000804)39:15<2586::AID-ANIE2586>3.0.CO;2-O
8. Niikura, H., Légaré, F., Hasbani, R., Bandrauk, A.D., Ivanov, M.Y., Villeneuve, D.M. and Corkum, P.B. Sub-laser-cycle electron pulses for probing molecule dynamics, *Nature* **417**, 917 (2002). DOI: doi:10.1038/nature00787
9. Niikura, H., Légaré, F., Hasbani, R., Ivanov, M.Y., Villeneuve, D.M. and Corkum, P.B. Probing molecular dynamics with attosecond resolution using correlated wave packet pairs, *Nature* **421**, 826 (2003). DOI: doi:10.1038/nature01430
10. Baker, S., Robinson, J.S., Haworth, C.A., Teng, H., Smith, R.A., Chirila, C.C., Lein, M., Tisch, J.W.G., and Marangos, J.P. Probing Proton Dynamics in Molecules on an Attosecond Time Scale, *Science* **312**, 424–427 (2006). DOI: 10.1126/science.1123904
11. Wörner, H. J., Bertrand, J. B., Kartashov, D. V., Corkum, P. B. & Villeneuve, D. M. Following a chemical reaction using high-harmonic interferometry. *Nature* **466**, 604–607 (2010). DOI: doi:10.1038/nature09185
12. Goulielmakis, E., Loh, Z-H., Wirth, A., Santra, R., Rohringer, N., Yakovlev, V.S., Zherebtsov, S., Pfeifer, T., Azzeer, A.M., Kling, M.F., Leone, S.R., and Krausz, F. Real-time observation of valence electron motion. *Nature* **466**, 739–743 (2010). DOI: doi:10.1038/nature09212
13. Haessler, S., Caillat, J., Boutu, W., Giovanetti-Teixeira, C., Ruchon, T., Auguste, T., Diveki, Z., Breger, P., Maquet, A., Carré, B., Taïeb, R., and Salières, P. Attosecond imaging of molecular electronic wavepackets, *Nature Physics* **6**, 200 (2010). DOI: doi:10.1038/nphys1511
14. Blaga C.I., Xu J., DiChiara, A.D., Sistrunk, E., Zhang, K., Agostini, P., Miller, T.A., DiMauro, L.F., and Lin, C.D. Imaging ultrafast molecular dynamics with

laser-induced electron diffraction, *Nature* **483**, 194 (2012). DOI: doi:10.1038/nature10820

15. Itatani, J., Levesque, J., Zeidler, D., Niikura, H., Pépin, H., Kieffer, J.C., Corkum, P.B., and Villeneuve, D.M. Tomographic imaging of molecular orbitals, *Nature* **432**, 867 (2004). DOI: doi:10.1038/nature03183
16. Lein, M. Molecular imaging using recolliding electrons, *J. Phys. B: At. Mol. Opt. Phys*. **40**, R135 (2007). DOI: 10.1088/0953-4075/40/16/R01
17. Meckel, M., Staudte, A., Patchkovskii, S., Villeneuve, D.M., Corkum, P.B., Dörner, R., and Spanner, M. Signatures of the continuum electron phase in molecular strong-field photoelectron holography, *Nature Physics* **10**, 594 (2014). DOI: doi:10.1038/nphys3010
18. Sandor, P., Tagliamonti, V., Zhao, A., Rozgonyi, T., Ruckenbauer, M., Marquetand, P., and Weinacht, T. Strong Field Molecular Ionization in the Impulsive Limit: Freezing Vibrations with Short Pulses, *Phys. Rev. Lett.* **116**, 063002 (2016). DOI: http://dx.doi.org/10.1103/PhysRevLett.116.063002
19. Alnaser, A.S., Kubel, M., Siemering, R., Bergues, B., Kling, N.G., Betsch, K.J., Deng, Y., Schmidt, J., Alahmed, Z.A., Azzeer, A.M., Ullrich, J., Ben-Itzhak, I., Moshammer, R., Kleineberg, U., Krausz, F., de Vivie-Riedle, R., and Kling, M.F. Subfemtosecond steering of hydrocarbon deprotonation through superposition of vibrational modes, *Nat. Commun.* **5**, 3800 (2014). DOI: doi:10.1038/ncomms4800
20. Miura, S., Ando, T., Ootaka, K., Iwasaki, A., Xu, H., Okino, T., Yamanouchi, K., Hoff, D., Rathje, T., Paulus, G.G., Kitzler, M., Baltuška, A., Sansone, G., Nisoli, M., Carrier-envelope-phase dependence of asymmetric C-D bond breaking C_2D_2 in an intense few-cycle laser field, *Chem. Phys. Lett.* **61**, 595(2014). DOI: doi:10.1016/j.cplett.2014.01.045
21. Xie, X., Roither, S., Schöffler, M., Lötstedt, E., Kartashov, D., Zhang, L., Paulus, G.G., Iwasaki, A., Baltuška, A., Yamanouchi, K., and Kitzler, M., Electronic Predetermination of Ethylene Fragmentation Dynamics, *Phys. Rev. X* **4**, 021005 (2014). DOI: http://dx.doi.org/10.1103/PhysRevX.4.021005
22. Xie, X., Doblhoff-Dier, K., Xu, H., Roither, S., Schöffler, M.S., Kartashov, D., Erattupuzha, S., Rathje, T., Paulus, G.G., Yamanouchi, K., Baltuška, A., Gräfe, S., and Kitzler, M. Selective Control over Fragmenation Reactions in Polyatomic Molecules Using Impulsive Laser Alignment, *Phys. Rev. Lett*, **112**, 163003 (2014). DOI: http://dx.doi.org/10.1103/PhysRevLett.112.163003
23. Menon, S.V., Nibarger, J.P., and Gibson, G.N. A framework for understanding molecular ionization in strong laser fields, *J. Phys. B: At. Mol. Opt. Phys*., **35**, 2961 (2002). DOI: http://dx.doi.org/10.1088/0953-4075/35/13/309
24. Johnsson, P., Lopez-Martens, R., Kazamias, S., Mauritsson, J., Valentin, C., Remetter, T., Varju, K., Gaarde, M.B., Mairesse, Y., Wabnitz, H., Salieres, P., Balcou, Ph., Schafer, K.J., and L'Huillier, A. Attosecond Electron Wave Packet

Dynamics in Strong Laser Fields, *Phys. Rev. Lett*. **95**, 013001 (2005). DOI: http://dx.doi.org/10.1103/PhysRevLett.95.013001

25. Kling, M.F., Siedschlag, Ch., Verhoef, A.J., Khan, J.I., Schultze, M., Uphues, Th., Ni, Y., Uiberacher, M., Drescher, M., Krausz, F., and Vraking, M.J.J. Control of Electron Localization in Molecular Dissociation, *Science* **312**, 246 (2006). DOI: 10.1126/science.1126259
26. McFarland, B.K., Farrell, J.P., Bucksbaum, P.H., and Guhr, M., High Harmonic Generation from Multiple Orbitals in N_2, *Science* **322**, 1232 (2008). DOI: doi:10.1126/science.1162780
27. Bergues, B., Kübel, M., Johnson, N.G., Fischer, B., Camus, N., Betsch, K.J., Herrwerth, O., Senftleben, A., Sayler, A.M., Rathje, T., Pfeifer, T., Ben-Itzhak, I., Jones, R.R., Paulus, G.G. Krausz, F., Moshammer, R., Ullrich, J., and Kling, M.F., Attosecond tracing of correlated electron-emission in non-sequential double ionization, *Nat. Commun*. **3**, 813 (2012). DOI: doi:10.1038/ncomms1807
28. Baltuška A., Udem, Th., Uiberacker, M., Hentschel, M., Goulielmakis, E., Gohle, Ch., Holzwarth, R., Yakovlev, V.S., Scrinzi, A., Hänsch, T.W., and Krausz, F., Attosecond control of electronic processes by intense light fields, *Nature* **421**, 611 (2003). DOI: doi:10.1038/nature01414
29. Reckenthaeler, P., Centurion, M., Werner, F., Trushin, S.A., Krausz, F., and Fill, E.F., Time-Resolved Electroni Diffraction from Selectively Aligned Molecules, *Phys. Rev. Lett*. **102**, 213001 (2009). DOI: http://dx.doi.org/10.1103/PhysRevLett.102.213001
30. Mignolet, B., Gijsbertsen, A., Vrakking, M.J.J., Levine, R.D., and Remacle, F. Stereocontrol of attosecond time-scale electron dynamics in ABCU using ultrafast laser pulses: a computational study, *Phys. Chem. Chem. Phys*. **13**, 8331 (2011). DOI: 10.1039/C1CP20094A
31. Breidbach, J. and Cederbaum, L.S., Migration of holes: Formalism, mechanisms, and illustrative applications, *J. Chem. Phys*. **118**, 3983 (2003). DOI: http://dx.doi.org/10.1063/1.1540618
32. Remacle, F. and Levine, R.D., An electronic time scale in chemistry, *Proc. Nat. Acad. Sci*. **103**, 6793 (2006). DOI: 10.1073/pnas.0601855103
33. Kuś, T., Mignolet, B., Levine, R.D. and Remacle, F. Pump and Probe of Ultrafast Charge Reorganization in Small Peptides: A Computational Study through Sudden Ionizations, *J. Phys. Chem. A* **117**, 10513 (2013). DOI: 10.1021/jp407295t
34. Perelomov, A.M., Popov, V.S., and Terent'ev, M.V. Ionization of Atoms in an Alternating Electric Field, *Sov. Phys. JETP*, **23**, 924 (1966).
35. Keldysh, L.V., Ionization in the Field of a Strong Electromagnetic Wave, *Sov. Phys. JETP* **20**, 1307 (1965).
36. Faisal, F.H.M. Multiple absorption of laser photons by atoms, *J. Phys. B: At. Mol. Phys.,* **6**, L89 (1973). DOI: http://dx.doi.org/10.1088/0022-3700/6/4/011
37. Reiss, H.R., Effect of an intense electromagnetic field on a weakly bound system, *Phys. Rev. A*, **22**, 1786 (1980). DOI: http://dx.doi.org/10.1103/PhysRevA.22.1786

38. Corkum, P.B. Plasma perspective on strong field multiphoton ionization, *Phys. Rev. Lett*. **71**, 1994 (1993). DOI: http://dx.doi.org/10.1103/PhysRevLett.71.1994
39. Lewenstein, M., Kulander, K.C., Schafer, K.J. and Bucksbaum, P.H., Rings in above-threshold ionization: A quasiclassical analysis, *Phys. Rev. A* **51**, 1495 (1995). DOI: http://dx.doi.org/10.1103/PhysRevA.51.1495
40. Ivanov M.Yu., Brabec, T. and Burnett, N. Coulomb corrections and polarization effects in high-intensity high-harmonic emission, *Phys. Rev. A*., **54**, p. 742-745 (1996). DOI: http://dx.doi.org/10.1103/PhysRevA.54.742
41. Joachain, C.J., Sylstra, N.J. and Potvilege, R.M. Atoms in Intense Laser Fields (Cambridge University Press, Cambridge, 2012)
42. Zavvriyev, A., Bucksbaum, P.H., Muller H.G., and Schumacher, D.W., Ionization and dissociation of H_2 in intense laser fields at 1.064 □m and 355 nm *Phys. Rev. A* **42**, 5500 (1990). DOI: http://dx.doi.org/10.1103/PhysRevA.42.5500
43. Zuo, T. and Bandrauk, A.D. Charge-resonance-enhanced ionization of diatomic molecular ions by intense lasers *Phys. Rev. A* **52**, R2511 (1995). DOI: http://dx.doi.org/10.1103/PhysRevA.52.R2511
44. Wu, J., Kunitski, M., Pitzer, M., Schmidt, L.Ph.H., Jahnke, T., Magrakvelidze, M., Madsen, C.B., Madsen, L.B., Thumm, U., and Dörner, R. Electron-Nuclear Energy Sharing in Above-Threshold Multiphoton Dissociative Ionization of H_2 *Phys. Rev. Lett*. **111**, 023002 (2013). DOI: http://dx.doi.org/10.1103/PhysRevLett.111.023002
45. Lein, M., Kreibich, T., Groos, E.K.U., and Engel, V. Strong-field ionization dynamics of a model H_2 molecule *Phys. Rev. A* **65**, 033403 (2002). DOI: http://dx.doi.org/10.1103/PhysRevA.65.033403
46. Staudt, A., Patchkovskii, S., Pavičić, D., Akagi, H., Smirnova, O., Zeidler, D., Meckel, M., Villeneuve, D.M., Dörner, R., Ivanov, M.Yu., and Corkum, P.B., Angular Tunneling Ionization Probability of Fixed-in-Space H_2 Molecules in Intense Laser Pulses *Phys. Rev. Lett*. **102**, 033004 (2009). DOI: http://dx.doi.org/10.1103/PhysRevLett.102.033004
47. Ben-Itzhak, I., Wang, P.Q., Sayler, A.M., Carnes, K.D., Leonard, M., Esry, B.D., Alnaser, A.S., Ulrich, B., Tong, X.M., Litvinyuk, I.V., Maharjan, C.M., Ranitovic, P., Osipov, T., Ghimire, S., Chang, Z., and Cocke, C.L. Elusive enhanced ionization structure for H_2^+ in intense ultrashort laser pulses *Phys. Rev. A* **78**, 063419 (2008). DOI: http://dx.doi.org/10.1103/PhysRevA.78.063419
48. Tong, X.-M., Zhao, Z. and Lin, C.D. Theory of molecular tunneling ionization. *Phys. Rev. A* **66**, 033402 (2002). DOI: http://dx.doi.org/10.1103/PhysRevA.66.033402
49. Brabec, T., Côté, M., Boulanger, P., and Ramunno, L. Theory of Tunnel Ionization in Complex Systems *Phys. Rev. Lett*. **95**, 073001 (2005). DOI: http://dx.doi.org/10.1103/PhysRevLett.95.073001
50. Lezius, M., Blanchet, B., Ivanov, M. Yu., and Stolow, A. Polyatomic molecules in strong laser fields: Nonadiabatic multielectron dynamics J. Chem. Phys. **117**,

1575 (2002).
DOI: http://dx.doi.org/10.1063/1.1487823
51. Talebpour, A., , Chien, C-Y., Chin, S.L., The effects of dissociative recombination in multiphoton ionization of O_2 *J. Phys. B: At. Mol. Opt. Phys.* **29**, L677 1996. DOI: http://dx.doi.org/10.1088/0953-4075/29/18/2002
52. Talebpour, A., Larochelle, S., and Chin, S.L. Suppressed tunneling ionization of the D_2 molecule in an intense Ti:sapphire laser pulse *J. Phys. B: At. Mol. Opt. Phys*. **31**, L49 1998. DOI: http://dx.doi.org/10.1088/0953-4075/31/2/003
53. Guo, C., Li, M., Nibarger, J.P., and Gibson, G.N., Single and double ionization of diatomic molecules in strong laser fields *Phys. Rev. A* **58**, R4271 1998. DOI: http://dx.doi.org/10.1103/PhysRevA.58.R4271
54. DeWitt, M.J., Wells, E., and Jones, R.R., Ratiometric Comparison of Intense Field Ionization of Atoms and Diatomic Molecules, *Phys. Rev. Lett*. **87**, 153001 2001.
DOI: http://dx.doi.org/10.1103/PhysRevLett.87.153001
55. Wells, E., DeWitt, M.J., and Jones, R.R., Comparison of intense-field ionization of diatomic molecules and rare-gas atoms *Phys. Rev. A* **66**, 013409 2002. DOI: http://dx.doi.org/10.1103/PhysRevA.66.013409
56. Akagi, H., Otobe, T., Staudte, A., Shiner, A., Turner, F., Dörner, R., Vileneuve, D.M. and Corkum, P.B., Laser Tunnel Ionization from Multiple Orbitals in HCl, *Science* **325**, 1364 (2009). DOI: 10.1126/science.1175253
57. Wu, J., Schmidt, L.Ph.H., Kunitski, M., Meckel, M., Voss S., Sann, H., Kim, H., Jahnke, T., Czasch, A., and Dörner, R. Multiorbital Tunneling Ionization of the CO Molecule, *Phys. Rev. Lett.* **108**, 183001 (2012). DOI: http://dx.doi.org/10.1103/PhysRevLett.108.183001
58. Wu, Z., Wu, C., Liu, X., Deng, Y., Gong, Q., Song, D., and Su, H. Double Ionization of Nitrogen from Multiple Orbitals *J. Phys. Chem. A*. **114**, 6751 (2010). DOI: 10.1021/jp1018197
59. Kotur, M., Weinacht, T.C., Zhou, C., and Matsika, S., Strong-Field Molecular Ionization from Multiple Orbitals, *Phys. Rev. X* 1, 021010 (2011). DOI: http://dx.doi.org/10.1103/PhysRevX.1.021010
60. Znakovskaya, I., von Den Hoff, P., Zherebtsov, S., Wirth, A., Herrwerth, O., Vrakking, M.J.J., de Vivie-Riedle, R. and Kling, M.F. Attosecond Control of Electron Dynamics in Carbon Monoxide *Phys. Rev. Lett.* **103**, 103002 (2009). DOI: http://dx.doi.org/10.1103/PhysRevLett.103.103002
61. Rohringer, N. and Santra R., Multchannel coherence in strong-field ionization *Phys. Rev. A* **79**, 053402 (2009). DOI: http://dx.doi.org/10.1103/PhysRevA.79.053402
62. Smirnova, O., Patchkovskii, S., Mairesse, Y., Dudovich, N. and Ivanov, M.Y. Strong-field control and spectroscopy of attosecend electron-hole dynmaics in molecules *Proc. Natl. Acad. Sci. USA* **106**, 16556 (2009). DOI: 10.1073/pnas.0907434106
63. Farrell, J.P., Petretti, S., Foerster, J., McFarland, B.K., Spector, L.S., Vanne, Y.V., Decleva, P., Bucksbaum, P.H., Saenz, A., and Guehr, M. Strong field ionization to Multiple Electronic States in Water *Phys. Rev. Lett.* **107**, 083001

(2011).
DOI: http://dx.doi.org/10.1103/PhysRevLett.107.083001
64. Geißler, D., Rozgonyi, T., González-Vazquez, J., González, L., Marquetand, P., and Weinacht, T.C., Pulse-shape-dependent strong-field ionization viewed with velocity-map-imaging, *Phys. Rev. A*., **84**, 053422 (2011). DOI: http://dx.doi.org/10.1103/PhysRevA.84.053422
65. Geißler, D., Rozgonyi, T., González-Vazquez, J., González, L., Nichols, S., and Weinacht, T.C., Creation of multihole molecular wave packets via strong-field ionization *Phys. Rev. A* **82** (2010). DOI: http://dx.doi.org/10.1103/PhysRevA.82.011402
66. Wörner, H.J., Bertrand, J.B., Hockett, P., Corkum, P.B., and Villeneuve, D.M. Controlling the Interference of Multiple Molecular Orbitals in High-Harmonic *Generation Phys. Rev. Lett*. **104**, 233904 (2010). DOI: http://dx.doi.org/10.1103/PhysRevLett.104.233904
67. Alnaser, A.S., Voss, S., tong, X.-M., Maharjan, C.M., Ranitovic, P., Ulrich, B., Osipov, T., Shan, B., Chang, Z., and Cocke, C.L. Effects of molecular structure on ion disintegration patterns in ionization of O_2 and N_2 by short laser pulses. *Phys. Rev. Lett*. **93**, 113003 (2004). DOI: http://dx.doi.org/10.1103/PhysRevLett.93.113003
68. Von den Hoff, P., Znakovskaya, I., Zherebtsov, S., Kling, M.F., and di Vivie-Riedle, R., Effects of multi orbital contributions in the angular dependent ionization of molecules in intense few-cycle laser pulses. *Appl. Phys. B* **98**, 659–666 (2010). DOI: 10.1007/s00340-009-3860-x
69. Lin, C.D., Le A.-T., Chen, Z., Morishita, T., and Lucchese, R., Strong-field rescattering physics-self-imaing of a molecule by its own electrons *J. Phys. B: At. Mol. Opt. Phys.* **43** 122001 (2010). DOI: http://dx.doi.org/10.1088/0953-4075/43/12/122001
70. Huismans, Y., Rouze, A., Gijsbertsen, A., Jungmann, J.H., Smolkowska, A.S., Logman, P.S.W.M., Lépine, F., Cauchy, C., Zamith, S., Marchenko, T., Bakker, J.M., Berden, G., Redlich, B., van der Meer, A.F.G., Muller, H.G., Vermin, W., Schafer, K.J., Spanner, M., Ivanov, M.Yu., Smirnova, O., Bauer, D., Popruzhenko, S.V., and Vrakking, M.J.J. *Science* **331**, 61 (2011). DOI: 10.1126/science.1198450
71. Hansen, J.L., Nielsen, J.H., Madsen, C.B., Lindhardt, A.T., Johansson, M.P., Skrydstrup, T., Madsen, L.B. and Stapelfeldt, H. Control and femtosecond time-resolved imaging of torsion in a chiral molecule *J. Chem. Phys*. **136**, 204310 (2012). DOI: http://dx.doi.org/10.1063/1.4719816
72. Wells, E., Rallis, C.E., Zohrabi, M., Siemering, R., Jochim, B., Andrews, P.R., Ablikim, U., Gaire, B., De, S., Carnes, K.D., Bergues, B., de Vivie-Riedle, R., Kling, M.F., and Ben-Itzhak, I., Adaptive strong-field control of chemical dynamics guided by three-dimensional momentum imaging *Nat. Comm*. **4**, 2895 (2013). DOI: doi:10.1038/ncomms3895
73. Freeman, R.R., Bucksbaum, P.H., Milchberg, H., Darack, S., Schumacher, D., and Geusic, M.E. Above-threshold ionization with subpicosecond laser pulses

Phys. Rev. Lett. **59**, 1092 (1987). DOI: http://dx.doi.org/10.1103/PhysRevLett.59.1092

74. Siemering, R., Njoya, O., Weinacht, T., and de Vivie-Riedle, R. Field-dressed orbitals in strong-field molecular ionization, *Phys. Rev. A* **49**, 042515 (2015). DOI: 10.1103/PhysRevA.02.04215
75. Rallis, C.E., Burwitz, T.G., Andrews, P.R., Zohrabi, M., Averin, R., De, S., Bergues, B., Jochim, B., Voznyuk, A.V., Gregerson, N., Gaire, B., Znakovskaya, I., McKenna, J., Carnes, K.D., Kling, M.F., Ben-Itzhak, I., and Wells, E., *Rev. Sci. Instrum*., **85**, 113105 (2014). DOI: http://dx.doi.org/10.1063/1.4899267
76. Xie, X., Lotstedt, E., Roither, S., Schöffler, M., Kartashov, D., Midorikawa, K., Baltuška, A., Yamanouchi, K., and Kitzler, M., Duration of an intense laser pulse can determine the breakage of multiple chemical bonds, *Scientific Reports* **5**, 12877 (2015). DOI: 10.1038/srep12877.
77. Lezius, M., Blanchet, V., Rayner, D.M., Villeneuve, D.M., Stowlow, A., and Ivanov, M.Yu., Nonadiabatic Multielectron Dynamics in Strong Field Molecular Ionization *Phys. Rev. Lett*. **86**, 51 (2001). DOI: http://dx.doi.org/10.1103/PhysRevLett.86.51
78. Kotur, M., Zhou, C., Matsika, S., Patchkovskii, S., Spanner, M., and Weinacht, T.C. Neutral-Ionic State Correlations in Strong-Field Molecular Ionization *Phys. Rev. Lett*. **109**, 203007 (2012). DOI: http://dx.doi.org/10.1103/PhysRevLett.109.203007
79. Sándor, P., Zhao, A., Rozgonyi, T, and Weinacht, T., Strong field molecular ionization to multiple ionic states: direct versus indirect pathways *J. Phys. B: At. Mol. Opt. Phys.* **47**, 124021 (2014). DOI: http://dx.doi.org/10.1088/0953-4075/47/12/124021
80. Werner, H.-J., Knowles, P.J., Knizia, G., Manby, F.R,. Schütz, M., Celani, P., Korona, T,. Lindh, R., Mitrushenkov, A., and Rauhut, G., MOLPRO, version 2012.1, a package of *ab initio* programs, 2012. http://www.molpro.net/
81. Smirnov, B.M. and Chibisov, M.I., The Breaking Up of Atomic Particles by an Electric Field and by Electron Collisions, *Sov. Phys. JETP* **22**, 585 (1966).
82. Barth, I., Hege, H.-C., Ikeda, H., Kenfack, A., Koppitz, M., Manz, J., Marquardt, F., and Paramonov, G.K. Concerted quantum effects of electronic and nuclear fluxes in molecules *Chem. Phys. Lett.* **481**, 118 (2009). DOI: 10.1016/j.cplett.2009.09.011
83. Wittmann, T., Horvath, B., Helml, W., Schätzel, M.G., Gu, X., Cavalieri, A.L., Paulus, G.G., and Kienberger, R. Single-shot carrier–envelope phase measurement of few-cycle laser pulses *Nat. Phys*. **5**, 357 (2009). DOI: 10.1038/nphys1250
84. Rathje, T., Johnson, N.G., Möller, M., Süßmann, F., Adolph, D., Kübel, M., Kienberger, R., Kling, M.F., Paulus, G.G., and Sayler, A.M. Review of attosecond resolved measurement and control via carrier–envelope phase tagging with above-threshold ionization *J. Phys. B: At. Mol. Opt. Phys. B* **45**, 074003 (2012). DOI: http://dx.doi.org/10.1088/0953-4075/45/7/074003

85. Sayler, A.M., Rathje, T., Müller, W., Kürbis, Ch., Rühle, K., Stibenz, G., and Paulus, G.G. Real-time pulse length measurement of few-cycle laser pulses using above-threshold ionization *Opt. Express* **19**, 4464 (2011). DOI: 10.1364/OE.19.004464
86. Eppink A.T.J.B. and Parker, D.H. Velocity map imaging of ions and electrons using electrostatic lenses: Application in photoelectron and photofragment ion imaging of molecular oxygen *Rev. Sci. Instrum.* **68**, 3477 (1997). DOI: http://dx.doi.org/10.1063/1.1148310
87. Whitaker, B.J., Imaging in Molecular Dynamics: Technology and Applications (A User's Guide) (Cambridge University Press, Cambridge, 2003).
88. Kling, N.G., Paul, D., Gura, A., Laurent, G., De, S., Li, H.; Wang, Z., Ahn, B., Kim, C.H., Kim, T.K., Litvinyuk, I.V., Cocke, C.L., Ben-Itzhak, I., Kim, D., and Kling, M.F. Thick-lens velocity-map imaging spectrometer with high resolution for high-energy charged particles, *JINST* 9, P05005 (2014). DOI: http://dx.doi.org/10.1088/1748-0221/9/05/P05005
89. Bordas, C., Paulig, F., Helm, H., and Huestis, D.L. Photoelectron imaging spectrometry: Principle and inversion method *Rev. Sci. Instrum*. **67**, 2257 (1996). DOI: http://dx.doi.org/10.1063/1.1147044

Acknowledgment: Augustana University personnel and equipment were funded by National Science Foundation Grant No. 1404185 and National Science Foundation/EPSCoR Grant No. 0903804. JRML operations and personnel were supported by the Chemical Sciences, Geosciences and Biosciences Division, Office of Basic Energy Sciences, Office of Science, U.S. Department of Energy. The PULSAR laser was provided by Grant No. DE-FG02-09ER16115 from the same funding agency. M.F.K., R.dV-R and R.S. are grateful for support by the German Science Foundation via the cluster of excellence Munich-Centre for Advanced Photonics. B. J. is also supported in part by the Department of Energy Office of Science Graduate Fellowship Program (DOE SCGF), made possible in part by the American Recovery and Reinvestment Act of 2009, and administered by ORISE-ORAU under contract no. DE-AC05-06OR23100.

Author Contributions: The experiments were carried out by BJ, MZ, AV, JBM, DGS, KJB, BB, TS, NGK, TGB, KDC, IBI, MFK and EW. The data analysis and interpretation were done by BJ, RS, AV, JBM, DGS, MFK, IBI, EW and RdV-R. RS and RdV-R provided theoretical analysis and calculations. BJ, RS, KDC, IBI, RdV-R and EW wrote the manuscript. All of the authors reviewed the manuscript and offered comments.

The authors declare no competing financial interests.

3.3 Angular dependent tunnel ionization from an excited state

As mentioned before non-linear molecules have to be described by more than one rotation and while the hydrocarbon series acetylene (C_2H_2), ethylene (C_2H_4) and ethane (C_2H_6) have a clearly relevant molecular axis, this is not an universal case for more complex molecules like CHD and its derivates. So a soft aligning step is the excitation of the molecule with a pump pulse and later ionization from the electronic excited state by a probe pulse. Assuming the molecules are randomly oriented before the arrival of the pump pulse, the first laser will introduce a cosine squared distribution for the excited molecules with respect to the angle θ (see fig. 3.3 (b)). This is the case, because the transition probability is proportional to the squared matrix element of the perturbation [18], in this case the two components of the pump pulse, the one parallel to the Transition Dipole Moment (TDM), which will excite the molecule and the perpendicular component which will not excite the molecule. Thus the molecules with a TDM along the laser polarization axis are excited preferentially. Figure 3.3 (left) sketches the situation for AT before and after the pump pulse (blue) interaction, with the resulting cosine squared distribution shown at the bottom right. In addition, the rotation around φ has to be taken into account ranging from 0°to 360°, uniformly, which leads to more round distributions. Pump and probe pulse are related by the polarization angle α. For a given delay time this angle is scanned between 0°and 180°. The probe pulse is responsible for the observed ionization. For a given α, the tunnel ionization probability $\tilde{T}(\alpha)$ is calculated as:

$$\tilde{T}(\alpha) = \sum_{\varphi,\theta} \frac{1}{N} \tilde{T}(\varphi,\theta) \cos^2(\alpha - \theta) \tag{3.7}$$

where $\tilde{T}(\varphi,\theta)$ is the tunneling probability $T(S)$ for a molecule rotated by φ and θ with reference to the TDM and N the corresponding normalization factor.

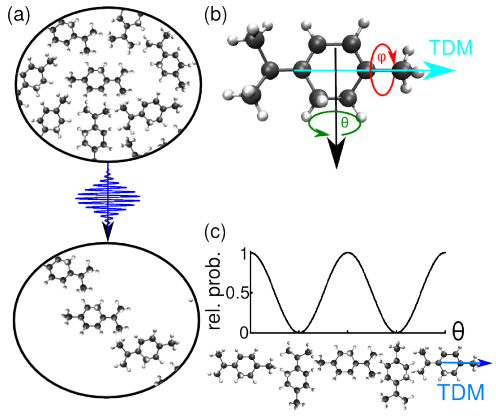

Figure 3.3: (a) A random ensemble of α-terpinene molecules. The pump laser pulse (blue) selects molecules for which the transition dipole moment (TDM) aligns with the laser polarization. (b) Illustration of the two angles describing the orientation between the molecule and the direction of the incoming pump and probe laser light. φ describes the rotation around the molecular transition dipole moment (TDM) axis and θ the rotation around an axis perpendicular to the TDM axis. (c) The resulting cosine squared distribution for the alignment of the excited molecules is shown.

The case of CHD and its derivates is also interesting, because all three molecules have very similar orbitals in the undisturbed state, but the spacial arrangement of the double bonds in AT and AP leads to an anisotropy in the tunnel ionization from the first excited state. The reason for this is, that the energy of the field dressed orbitals differs whether a double bond is present in the field direction or not. Figure 3.4 shows the ionization pulse and molecule for the largest contrast in the angular dependent tunnel ionization of α-terpinene (AT). For CHD and α-phellandrene (AP) the sp^2 C-H bonds (indicated by dark red circles) line up in both cases, but in AT this is only the case for $\alpha = 90°$.

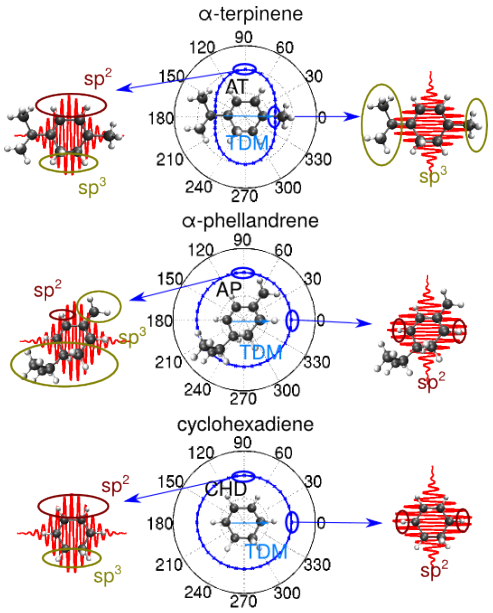

Figure 3.4: Calculated angular-dependent ionization yields $\tilde{T}(\alpha)$ for AT, AP, and CHD shown in the middle column. CHD shows the most isotropic angular dependence, AP is almost isotropic , and AT is anisotropic. On the left- and right-hand sides, the molecules are shown along with the ionization pulse for two selected angles ($\alpha = 0°$and $\alpha = 90°$). The molecular transition dipole moment is oriented exactly along the pump-pulse polarization vector. The selected angles correspond to the axis of anisotropy for AT. For both α values AP and CHD have sp^2 C-H bonds (indicated by dark red circles) along the direction of the probe pulse. In contrast, AT has only sp^3 C-H bonds (indicated by olive circles) along the direction of the probe laser for $\alpha = 0°$, while for $\alpha = 90°$again sp^2 C-H bonds are present.

On the next pages the article “Field-dressed orbitals in strong-field molecular ionization” published in *Physical Review A* is reprinted with permission from *Phys. Rev. A* **92**, 042515 (2015).

PHYSICAL REVIEW A **92**, 042515 (2015)

Field-dressed orbitals in strong-field molecular ionization

Robert Siemering,[1] Oumarou Njoya,[2] Thomas Weinacht,[2] and Regina de Vivie-Riedle[1]
[1]*Department Chemie, Ludwig-Maximilians-Universität München, Butenandt Strasse 11, 81377 München, Germany*
[2]*Department of Physics and Astronomy, Stony Brook University, 100 Nicolls Road, Stony Brook, New York 11794-3800, USA*
(Received 20 April 2015; published 30 October 2015)

We demonstrate the importance of considering the shape of field-dressed molecular orbitals in interpreting angle-dependent measures of strong-field ionization from excited states. Our calculations of angle-dependent ionization for three homologous polyatomic molecules with very similar valence orbitals show that one has to take into account the shape of the field-dressed orbitals rather than the field-free orbitals in order to rationalize the experimental measurements.

DOI: 10.1103/PhysRevA.92.042515 PACS number(s): 31.15.ae, 33.80.Wz

Strong-field molecular ionization is at the forefront of current research on molecular structure and dynamics, particularly on attosecond time scales [1,2]. It is the first step in high-harmonic generation, which is used to generate attosecond light pulses, and it can be used to probe excited-state molecular dynamics as there are no dark states and one is not sensitive to the exact photon energy [3–8]. Furthermore, angle-resolved measurements of strong-field ionization have been shown to be sensitive to molecular structure and to reveal information about molecular orbitals from which electrons are removed during the ionization process [9–13].

Earlier work on small molecules demonstrated that angle-resolved strong-field ionization experiments showed angle-dependent yields that followed the calculated shapes of the highest occupied molecular orbital (HOMO) [14–17]. Other examples demonstrated the contributions from a superposition of the HOMO and the lowest unoccupied molecular orbital (LUMO) [18–20]. Molecular Ammosov-Delone-Krainov calculations of the angle-dependent ionization based on the calculated molecular or Dyson orbitals gave good agreement with the measured yields [21]. However, comparisons between calculation and experiment for larger systems have not been as favorable [22]. Furthermore, recent measurements on a series of molecules with similar molecular orbitals yielded different angle-dependent yields [23]. A recently developed method to calculate angular-dependent ionization probabilities based on electronic structure theory [20] seems flexible enough for larger systems.

In this work we demonstrate that it is the field-dressed molecular orbitals that provide insight into the angle dependence of the ionization yield. If the oscillations of the laser field are slow enough that the electrons in the molecule rearrange themselves as the field increases and decreases each half cycle, then the removal of an electron takes place from a Stark-shifted molecular orbital [24] and the shape of this orbital determines the angle dependence of the ionization yield.

We perform detailed calculations of the angle-dependent yield for three molecules from a homologous family: α-terpinene (AT), α-phellandrene (AP), and cyclohexadiene (CHD), which have calculated (measured) ionization potentials of 7.7 (7.6) eV, 8.0 eV, and 8.1 (8.2) eV, respectively. The calculations are for the molecules excited to their first bright neutral excited state, since this provides a natural method for aligning the molecules in experiment. In addition, the signal directly records the ionization probability of the molecule without a mapping step to the generated fragments as is often necessary in strong-field few-cycle experiments [25]. The calculations are compared with the measured yields and show remarkable agreement given the fact that the experiments have significant multiphoton character whereas the calculations are for pure tunnel ionization.

Measurements are performed using an amplified ultrafast titanium sapphire laser system in conjunction with an effusive molecular beam and time-of-flight mass spectrometer. The laser system produces 30-fs pulses with an energy of 1 mJ at a repetition rate of 1 kHz. Pump pulses at a central wavelength of 262 nm and a duration of 50 fs are generated via third-harmonic generation and focused in the molecular beam (to an intensity of about 0.3 TW/cm^2) to promote a fraction of the molecules to their first bright excited state. The molecules are probed with a more intense pulse at a central wavelength of 780 nm, focused to intensities between 5 and 10 TW/cm^2. The polarization of the pump pulses is varied with respect to the probe pulses by using a half wave plate, allowing us to vary the direction of the field of the ionization pulse relative to the transition dipole moment of the molecules. Molecular fragment ions are collected in a time-of-flight mass spectrometer. We measure the parent ion yield as a function of pump probe delay and polarization.

We calculated the angle-dependent ionization rates for the first optically excited states of CHD, AT, and AP. We performed quantum chemical calculations for the ground and the first three excited states with the MOLPRO program package [26] at the complete active space self-consistent field (CASSCF) (4,4) level of theory using the 6-31++G** basis set. The calculations were carried out with and without an external dipole field, which was added to the one-electron Hamiltonian to simulate the interaction with the strong-ionization field. The orientation of the molecules relative to the pump and probe polarization axes was included in the simulations.

The first angle φ is the rotation around the molecular transition dipole moment (TDM) axis and the second angle θ is the rotation around an axis perpendicular to the TDM axis, e.g., perpendicular to or in the molecular plane. These two angles are sufficient to describe all possible orientations between the molecule and the polarization vector of the incoming light fields. Both angles were varied in 10° steps.

The ionization probability of a molecule in a laser field can be modeled in terms of the induced electron flux through the barrier of the combined molecular and external electric field [27] (atomic units $m = \hbar = e = 1$ are used throughout

 ©2015 American Physical Society

the paper). This can be expressed as

$$W(t) = \int_S j(r,t)dS,$$
$$j(r,t) = -\frac{i}{2}[\psi(r,t)\nabla\psi(r,t)^* - \psi(r,t)^*\nabla\psi(r,t)]. \quad (1)$$

Here $j(r,t)$ is the electron flux density and $\psi(r,t)$ the electronic wave function in the presence of the electric field inducing the electron flux $W(t)$. For the surface S it is convenient to choose a plane perpendicular to the direction of the electric field. In our case S is located at the outer turning points of the electronic wave function. Here the wave function enters the classical forbidden region where tunneling occurs. The electronic wave functions, evaluated by a quantum chemical program package, are typically real and their flux density [Eq. (1)] is zero.

In Refs. [18,20] we showed that this problem can be overcome by evaluating the electron flux for the electron density $\rho(r,t)$ with the help of the divergence theorem and the continuity equation as proposed by [28]. We can then rewrite Eq. (1) as

$$W(t) = -\int_{V'} \nabla j(r,t)dV' = \frac{d}{dt}\int_{V'} \rho(r,t)dV', \quad (2)$$

with V' being the part of the total volume V in which the electronic wave function $\psi(r)$ is defined and which is spanned by the surface S and a vector perpendicular to S pointing away from the nuclei. In order to calculate the tunneling probability $T(S)$, we need the electron density with (at final time t_f) and without the external field (at initial time t_i). Therefore, we integrate Eq. (2) over time and obtain

$$T(t;S) = \int_{V'} \rho(r,t_f)dV' - \int_{V'} \rho(r,t_i)dV'. \quad (3)$$

In the present case, the tunneling probability $T(t;S)$ for the first optically excited state is sought. For CHD, low-lying Rydberg states in the Franck-Condon (FC) region have already been discussed in the literature [29,30]. We found low-lying Rydberg states in the FC region for the substituted CHD derivatives as well. In all three molecules the first excited state has Rydberg character and corresponds to an excitation from the HOMO to the LUMO (Rydberg). The optically active state is the second excited state, a $\pi\pi^*$ excitation (from the HOMO to the LUMO+1). Tunneling occurs mostly from the frontier orbitals and for our analysis we take into account the LUMO and the LUMO+1 orbitals from the state-averaged CASSCF calculation. Contributions from the HOMO are negligible.

To treat ionization from more than one orbital we solve the working equations derived above for a linear combination of the selected molecular orbitals. This implies a basis transformation rewriting the two orbitals (e.g., LUMO and LUMO+1) in the Slater determinant into the orbitals LUMO+LUMO+1 and LUMO–LUMO+1, allowing for coherent ionization of the electron from both orbitals [18,20].

This method is further extended to calculate tunnel ionization from excited states. Assuming the molecules are randomly oriented before the arrival of the pump pulse, the pump pulse introduces a $\cos^2$ distribution for the excited molecules with respect to the angle θ. Thus the molecules with a TDM along the laser polarization axis are excited preferentially. In addition, the rotation around φ has to be taken into account ranging from 0° to 360°, uniformly.

The pump and probe pulse are related by the polarization angle α. For a given delay time this angle is scanned between 0° and 180°. The probe pulse is responsible for the observed ionization. For a given α, the tunnel ionization probability $\tilde{T}(\alpha)$ is calculated as

$$\tilde{T}(\alpha) = \sum_{\varphi,\theta} \frac{1}{N} \tilde{T}(\varphi,\theta)\cos^2(\alpha - \theta), \quad (4)$$

where $\tilde{T}(\varphi,\theta)$ is the tunneling probability $T(S)$ for a molecule rotated by φ and θ with reference to the TDM and N the corresponding normalization factor.

The measured and calculated values for the angle-dependent ionization are shown in Fig. 1. The data are recorded for zero time delay. Similar observations have been obtained for different time delays and are discussed in detail in Ref. [23]. The angular dependence seen in the ionization yield for AT varies slightly with intensity, with the anisotropy decreasing with decreasing probe intensity, but persisting for even the lowest intensities where signal is observed [23]. While the measurements were carried out in a regime of mixed multiphoton and tunnel character, the calculations focus on tunnel ionization after $\pi\pi^*$ excitation, neglecting the multiphoton character in the experimental ionization. This explains the slight deviations from experiment but illustrates that tunnel ionization is key to the observed anisotropic behavior. Although the π and π^* orbitals of all three molecules have a very similar shape, differences in the angle-dependent tunnel ionization (ADTI) are observed, in theory as well as in experiment. The tunnel ionization for CHD is almost perfectly isotropic. The same is observed for AP, while, surprisingly, AT shows a distinct anisotropy.

To understand this behavior, we analyze the field-dressed molecular orbitals and discuss the reason for the observed anisotropy in detail for the case of AT. The strong probe pulse (Fig. 2, red) ionizes the excited-state molecules and the angle dependence is recorded. Figure 2 shows the ionization pulse and molecule for two values of α, 0° and 90°, for which there is the largest contrast in the ADTI of AT. For clarity, we show the molecules whose TDM are oriented exactly along the pump pulse polarization. We observe the following differences: For CHD and AP the sp^2 C-H bonds (indicated by dark red circles) line up along the polarization axis of the ionization pulse for both α values, while in AT this is only the case for $\alpha = 90°$. For $\alpha = 0°$ an sp^3 C-H bond (olive circle) exists along the probe direction.

sp^2 bonds are more easily polarized than sp^3 bonds due to their π-orbital character. Polarizability is an important factor in tunnel ionization with strong fields. If the excited state prepared with the pump pulse becomes polarized in the strong field of the probe pulse, then there will be more ionization. If the polarization depends on the angle α, then the strong-field ionization yield will also depend on the angle. Depending on the molecule, strong-field interaction can significantly mix and distort the orbitals in a way that depends on the angle of the field relative to the molecule [20]. In the case of the small organic molecules, it is important to consider the presence of low-lying Rydberg orbitals (see Fig. 3 for AT), already in

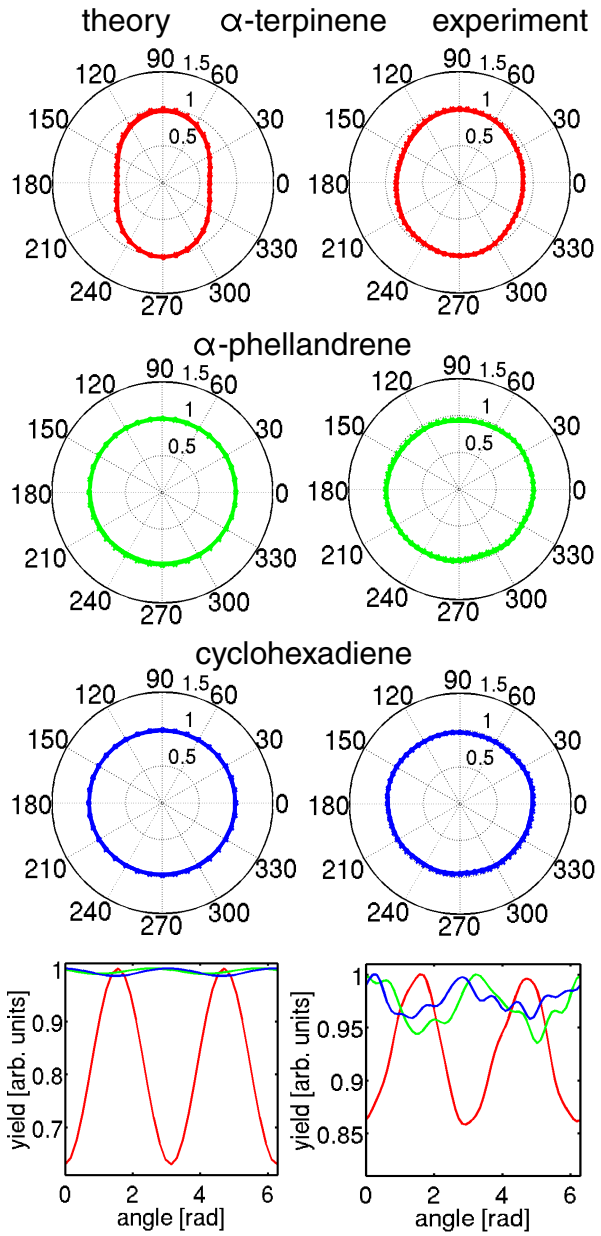

FIG. 1. (Color online) Calculated (left) and measured (right) angle-dependent ionization yields for α-terpinene (red), α-phellandrane (green), and cyclohexadiene (blue). Measurements are presented for zero time delay between pump and probe pulses. Similar results were obtained for small positive delays between pump and probe pulses. The bottom two panels show the calculated (left) and measured (right) ionization yields as a function of angle between pump and probe pulses for all three molecules. Experimental uncertainties are about 2% of the yields.

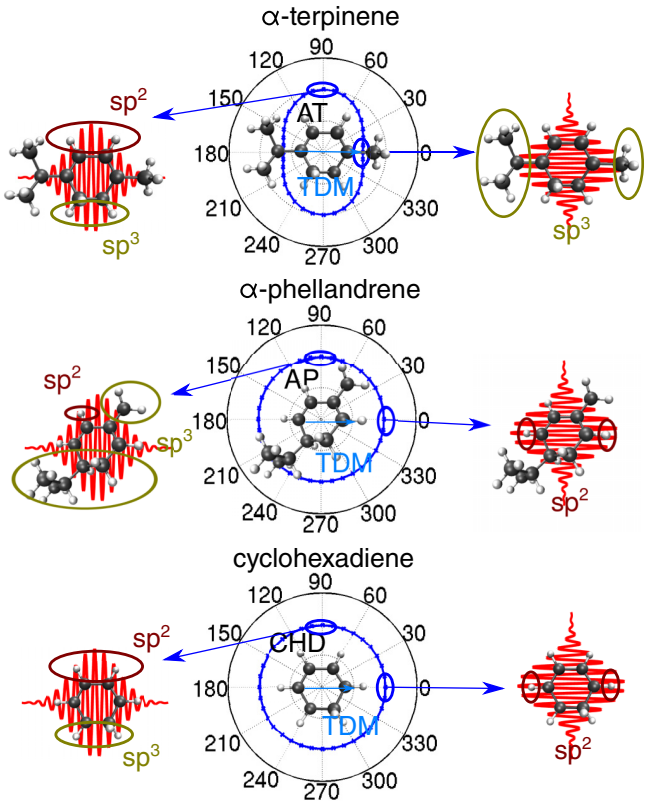

FIG. 2. (Color online) Calculated angular-dependent ionization yields $\tilde{T}(\alpha)$ for AT, AP, and CHD shown in the middle column. CHD shows the most isotropic angular dependence, AP is almost isotropic, and AT is anisotropic. On the left- and right-hand sides, the molecules are shown along with the ionization pulse for two selected angles between the pump and probe pulses ($\alpha = 0°$ and 90°). The molecular transition dipole moment is oriented exactly along the pump-pulse polarization vector. The selected angles correspond to the axis of anisotropy for AT. For both α values AP and CHD have sp^2 C-H bonds (indicated by dark red circles) along the direction of the probe pulse. In contrast, AT has only sp^3 C-H bonds (indicated by olive circles) along the direction of the probe laser for $\alpha = 0°$, while for $\alpha = 90°$ again sp^2 C-H bonds are present.

the field-free molecules. This is different for most diatomics. Rydberg orbitals are diffuse and easy to polarize, thus they will enhance tunnel ionization. The degree of orbital mixing and its angle dependence is determined in large part by whether sp^3 or sp^2 orbitals line up along the laser polarization. sp^3 bonds will mix less with Rydberg orbitals compared with sp^2 bonds. AT has sp^2 orbitals only perpendicular to the TDM and thus a larger difference in the perpendicular vs parallel ADTI signal than the other two molecules. This interpretation is based upon an analysis of field-dressed orbitals. Orbital mixing induced by the ionization pulse is shown for the most interesting case of AT in Fig. 3.

For all α values the strong field stabilizes the originally delocalized LUMO (Rydberg, blue line) orbital into a localized version pointing into the direction of the light field. In the case where the laser direction coincides with the direction of an sp^2 (or sp) C-H bond, an additional, originally-higher-lying Rydberg orbital (red line) is stabilized close to the energy of the π orbital (black line). This stabilization leads to an equivalent occupation of the π orbital and LUMO+1 orbitals in the excited-state configuration. This scenario is shown for $\alpha = 90°$. Our calculations show that the mixing in of the Rydberg character leads to a large tunneling rate for the LUMO+1 in

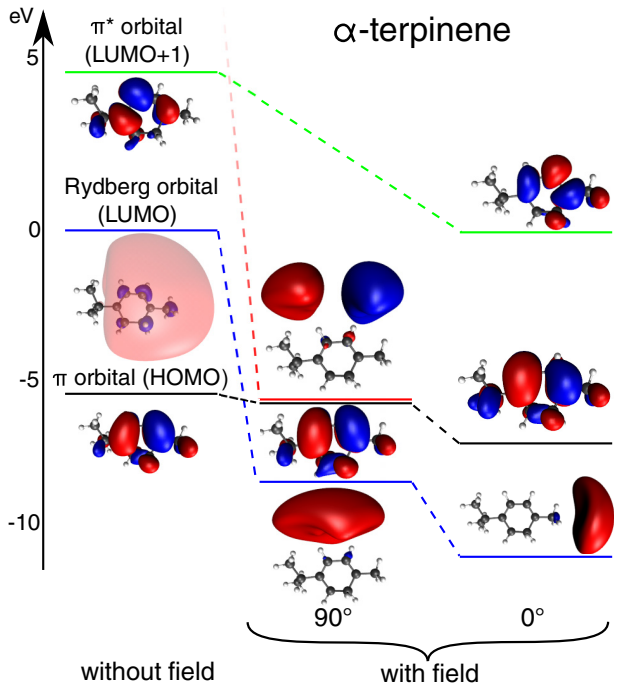

FIG. 3. (Color online) State-averaged CASSCF molecular orbitals from which an electron is removed for α-terpinene, giving rise to anisotropy in the angular ionization rate. Without field the π orbital is the HOMO (black line), the Rydberg orbital is the LUMO (blue line) and the $\pi*$ orbital is the LUMO+1 (green line). We use dashed lines to indicate the correlations of the orbitals with and without field. For all α values the light field stabilizes the originally delocalized LUMO (Rydberg) orbital into a localized version pointing in the direction of the light field. When the laser direction coincides with the direction of an sp^2 (or sp) C-H bond, an additional, originally-higher-lying Rydberg orbital (red line) is stabilized close in energy to the π orbital. This scenario is shown for $\alpha = 90°$. For $\alpha = 0°$ the laser direction coincides with the direction of the sp^3 C-H bond and the additional higher-lying Rydberg orbital is not stabilized.

that direction. The laser-stabilized π orbital contributes very little to the angle-dependent ionization rate. For $\alpha = 0°$ the situation is changed. Now the laser direction coincides with the direction of the sp^3 C-H bond and the additional higher-lying Rydberg orbital is not stabilized, therefore not occupied and thus leading to less ionization probability in this direction. For CHD and AP the $\alpha = 0°$ case is similar to the $\alpha = 90°$ case and the LUMO+1 always has Rydberg character. As the tunneling also depends on the energy of the orbital, the low-lying field-dressed HOMO–1 orbital with strong Rydberg character does not participate.

We have considered the role of Stark-shifted or field-dressed molecular orbitals in describing strong-field ionization of polyatomic molecules from the first excited state. Our calculations of the angle-dependent ionization yield agree well with measurements and indicate that in contrast to smaller less polarizable molecules, field-dressed orbitals need to be taken into account in order to capture the measured angle-dependent yields.

For some molecules, particularly small ones that are not very polarizable (such as N_2), the field-free orbitals and states are not affected as much by the strong field. This is different from the case of the small organic molecules we considered. Here the field can significantly mix and distort the orbitals in a way that depends on the angle of the field relative to the molecule. The reason lies in the low-lying Rydberg orbitals that exist already in the field-free molecules for all three systems. The observed differences are determined in large part by whether sp^3 or sp^2 orbitals line up along the polarization axis of the ionization field.

R.d.V.-R. and R.S. gratefully acknowledge financial support from the Deutsche Forschungsgemeinschaft through the SFB749 and the cluster of excellence Munich-Centre for Advanced Photonics (MAP). T.W. gratefully acknowledges support from the Department of Energy under Grant No. DEFG02-08ER15983.

[1] M. Y. Ivanov, M. Spanner, and O. Smirnova, J. Mod. Opt. **52**, 165 (2005).
[2] Y. Mairesse *et al.*, Phys. Rev. Lett. **104**, 213601 (2010).
[3] T. Popmintchev, M.-C. Chen, P. Arpin, M. M. Murnane, and H. C. Kapteyn, Nat. Photon. **4**, 822 (2010).
[4] M. F. Kling and M. J. Vrakking, Annu. Rev. Phys. Chem. **59**, 463 (2008).
[5] Z. Chang and P. Corkum, J. Opt. Soc. Am. B **27**, B9 (2010).
[6] P. Agostini and L. F. DiMauro, Rep. Prog. Phys. **67**, 813 (2004).
[7] R. Kienberger, M. Uiberacker, M. F. Kling, and F. Krausz, J. Mod. Opt. **54**, 1985 (2007).
[8] W. Li, A. A. Jaroń-Becker, C. W. Hogle V. Sharma, X. Zhou, A. Becker, H. C. Kapteyn, and M. M. Murnanea, Proc. Natl. Acad. Sci. U.S.A. **107**, 20219 (2010).
[9] L. Holmegaard *et al.*, Nat. Phys. **6**, 428 (2010).
[10] T. K. Kjeldsen, C. Z. Bisgaard, L. B. Madsen, and H. Stapelfeldt, Phys. Rev. A **68**, 063407 (2003).
[11] J. Itatani, J. Levesque, D. Zeidler, H. Niikura, H. Pépin, J. C. Kieffer, P. B. Corkum, and D. M. Villeneuve, Nature (London) **432**, 867 (2004).
[12] I. V. Litvinyuk, K. F. Lee, P. W. Dooley, D. M. Rayner, D. M. Villeneuve, and P. B. Corkum, Phys. Rev. Lett. **90**, 233003 (2003).
[13] A. S. Alnaser, C. M. Maharjan, X. M. Tong, B. Ulrich, P. Ranitovic, B. Shan, Z. Chang, C. D. Lin, C. L. Cocke, and I. V. Litvinyuk, Phys. Rev. A **71**, 031403 (2005).
[14] A. Fleischer, H. J. Wörner, L. Arissian, L. R. Liu, M. Meckel, A. Rippert, R. Dörner, D. M. Villeneuve, P. B. Corkum, and A. Staudte, Phys. Rev. Lett. **107**, 113003 (2011).
[15] D. Pavicic, K. F. Lee, D. M. Rayner, P. B. Corkum, and D. M. Villeneuve, Phys. Rev. Lett. **98**, 243001 (2007).
[16] A. S. Alnaser, S. Voss, X. M. Tong, C. M. Maharjan, P. Ranitovic, B. Ulrich, T. Osipov, B. Shan, Z. Chang, and C. L. Cocke, Phys. Rev. Lett. **93**, 113003 (2004).

[17] O. Smirnova, S. Patchkovskii, Y. Mairesse, N. Dudovich, and M. Y. Ivanov, Proc. Natl. Acad. Sci. U.S.A. **106**, 16556 (2009).
[18] I. Znakovskaya, P. von den Hoff, S. Zherebtsov, A. Wirth, O. Herrwerth, M. J. J. Vrakking, R. de Vivie-Riedle, and M. F. Kling, Phys. Rev. Lett. **103**, 103002 (2009).
[19] H. Akagi, T. Otobe, A. Staudte, A. Shiner, F. Turner, R. Dörner, D. M. Villeneuve, and P. B. Corkum, Science **325**, 1364 (2009).
[20] P. von den Hoff, I. Znakovskaya, S. Zherebtsov, M. F. Kling, and R. de Vivie-Riedle, Appl. Phys. B **98**, 659 (2009).
[21] Z. X. Zhao, X.-M. Tong, and C.-D. Lin, Phys. Rev. A **67**, 043404 (2003).
[22] M. Kotur, T. C. Weinacht, C. Zhou, and S. Matsika, Phys. Rev. X **1**, 021010 (2011).
[23] O. Njoya, S. Matsika, and T. Weinacht, ChemPhysChem **14**, 1451 (2013).
[24] D. Dimitrovski, C. P. J. Martiny, and L. B. Madsen, Phys. Rev. A **82**, 053404 (2010).
[25] E. Wells *et al.*, Nat. Commun. **4**, 2895 (2013).
[26] H.-J. Werner, P. J. Knowles, G. Knizia, F. R. Manby, M. Schütz, P. Celani, T. Korona, R. Lindh, A. Mitrushenkov, and G. Rauhut, MOLPRO, version 2012.1, a package of *ab initio* programs, 2012.
[27] B. M. Smirnov and M. I. Chibisov, Sov. Phys. JETP **22**, 585 (1966).
[28] I. Barth, H.-C. Hege, H. Ikeda, A. Kenfack, M. Koppitz, J. Manz, F. Marquardt, and G. K. Paramonov, Chem. Phys. Lett. **481**, 118 (2009).
[29] P. E. Share, K. L. Kompa, S. D. Peyerimhoff, and M. C. van Hemert, Chem. Phys. **120**, 411 (1988).
[30] D. Geppert and R. de Vivie-Riedle, Chem. Phys. Lett. **404**, 289 (2005).

4 Control of nuclear dynamics

A major goal of laser chemistry is to control reactions with tailored light fields. This goes beyond excitation of vibrational modes or monitoring nuclear motions during a chemical reaction to actively steer the atoms to specific bond cleavage or bond rearrangement or to suppress or enhance specific reaction pathways [91]. The laser field then takes over the role of a reactive ingredient or a catalyst. The main parameters of the laser field, that can be manipulated, are the shape, the relative phase, the absolute phase, also called carrier envelope phase (CEP) and to a lesser extend the frequency [92–95]. In the experiments the CEP can be measured in coincidence for each shot with a beam splitter, while the shape is formed with a dazzler that can alter the spectral phase and amplitude [96, 97].

4.1 Suppression of a barrier with a laser

The first example is the isomerization of acetylene (HCCH) to vinylidene (CCHH) in the dication of the molecule. The bond strength is weakened in the dicationic state of the molecule, so the barriers of the proton migration is lower and the molecule is prone to fragmentation, which allows to detect the geometry of the molecule via the different fragments. The C-C bond cleavage leads to 2 CH^+ when still in the acetylene formation and to C^+ and CH_2^+ from the vinylidene one. In the experiment these different channels could be detected with 3 dimensional velocity map imaging (VMI). As the optimization of a laser pulse for a given target takes many iterations in optimized control experiments (OCE) it is important that the measurement, that ultimately defines the optimization goal, can be interpreted fast enough. This can be problematic if the raw data of the experimental measurement leads to sub optimal control results, because then not only the acquisition time but also the time to analyze the image is needed every iteration. Therefore a rapid inversion algorithm is necessary to use 3D VMI information as the target from the 2D measurements. As the laser polarization axis has a cylindrical symmetry the inversion requires an inverse Abel transformation [98]. In this experiment the "onion-peeling" or "back-projection" method from ref. [99] was chosen, because it was faster than other tested methods and did not need manual selection of initial parameters. For smaller systems a comparable theoretical description could be derived with optimal control theory (OCT), but acetylene has seven internal degrees of freedom (excluding translation and rotation). As OCT utilizes a full nuclear wave function, the computational resources can not handle seven dimensional wave functions in a timely manner, therefore a two or three dimensional subsystem would be needed for it. The alternative to keep the full dimensional space are semi-classical trajectories, which treat nuclear motions classically (equation 4.1) and energies and gradients quantum mechanically (equation 4.2).

$$-\nabla_r E_i = m\ddot{R} \tag{4.1}$$

$$\hat{H}\Psi_i = E_i\Psi_i \tag{4.2}$$

While this method could only optimize the laser for one possible starting condition at a time, it can be used to investigate the effect of the experimentally discovered laser fields on all trajectories by including it in the one electron Hamilton operator of equation 4.2 (for $\hat{H}_{\text{el}}$ see eq. 2.2).

$$\hat{H} = \hat{H}_{\text{el}} + \hat{V}_{\text{dip}} \tag{4.3}$$

This ansatz does not include ionization, so this step was approximated by starting the trajectory distribution in the dicationic state with the laser field near the first envelope peak. A point of comparison between the experiment and the calculation is the kinetic energy release (KER) of the CH_2^+ fragments. The experimental pulses have been optimized to increase the isomerization, measured as the ratio of CH_2^+ to CH^+ fragments. The optimized pulses have a lower KER contribution in experimental measures and in the calculated trajectories than the unoptimized Fourier-transform limited pulse. The calculations for these trajectories in this work used a modified version of the Newton-X code [44, 100]. Analyzing the trajectories show that the time interval between two peaks in the optimized pulses is in agreement with the time of the isomerization. This multi-peak structure with similar time delays is a main feature of different optimized pulses, so it stands to reason, that the second peak lowers the barrier of the vinylidene dissociation channel, allowing molecules with lower kinetic energy to pass it. On the next pages the article "Adaptive strong-field control of chemical dynamics guided by three-dimensional momentum imaging" published in *Nature Communications* is reprinted with permission from *Nat. Commun.* **4**, 2895 (2013).

nature COMMUNICATIONS

ARTICLE

Received 20 Aug 2013 | Accepted 7 Nov 2013 | Published 6 Dec 2013

DOI: 10.1038/ncomms3895

Adaptive strong-field control of chemical dynamics guided by three-dimensional momentum imaging

E. Wells[1], C.E. Rallis[1], M. Zohrabi[2], R. Siemering[3], Bethany Jochim[1], P.R. Andrews[1], U. Ablikim[2], B. Gaire[2,†], S De[2,†], K.D. Carnes[2], B. Bergues[4], R. de Vivie-Riedle[3], M.F. Kling[2,4] & I. Ben-Itzhak[2]

Shaping ultrafast laser pulses using adaptive feedback can manipulate dynamics in molecular systems, but extracting information from the optimized pulse remains difficult. Experimental time constraints often limit feedback to a single observable, complicating efforts to decipher the underlying mechanisms and parameterize the search process. Here we show, using two strong-field examples, that by rapidly inverting velocity map images of ions to recover the three-dimensional photofragment momentum distribution and incorporating that feedback into the control loop, the specificity of the control objective is markedly increased. First, the complex angular distribution of fragment ions from the $n\omega + C_2D_4 \rightarrow C_2D_3^+ + D$ interaction is manipulated. Second, isomerization of acetylene ($n\omega + C_2H_2 \rightarrow C_2H_2^{2+} \rightarrow CH_2^+ + C^+$) is controlled via a barrier-suppression mechanism, a result that is validated by model calculations. Collectively, these experiments comprise a significant advance towards the fundamental goal of actively guiding population to a specified quantum state of a molecule.

[1] Department of Physics, Augustana College, Sioux Falls, South Dakota 57197, USA. [2] J.R. Macdonald Laboratory, Department of Physics, Kansas State University, Manhattan, Kansas 66506, USA. [3] Department für Chemie, Ludwig-Maximilians-Universität München, Butenandt-Strasse 11, D-81377 München, Germany. [4] Max Planck Institute of Quantum Optics, Hans-Kopfermann-Str. 1, D-85748 Garching, Germany. † Present addresses: Lawrence Berkeley National Laboratory, One Cyclotron Road, Berkeley, CA 94720, USA. (B.G.); Saha Institute of Nuclear Physics, 1/AF Bidhannagar, Kolkata 700064, India (S.D.). Correspondence and requests for materials should be addressed to E.W. (email: eric.wells@augie.edu).

© 2013 Macmillan Publishers Limited. All rights reserved.

Chemical reaction dynamics can be monitored on time-scales of the electronic and nuclear motions[1–7], thanks to advances in laser technology[7–9]. These advances have led to increasing interest in using ultrafast laser pulses to manipulate chemical processes via direct control of the electronic and nuclear dynamics[7,10]. Active manipulation of the dynamics, however, is a challenging problem: rapid internal vibrational redistribution often thwarts simple approaches; the laser-modified potential energy surfaces (PESs) are complex; and the intense laser-molecule interaction must not destroy the target system before it reaches its desired final state. For these reasons and others, a priori selection of suitable laser-pulse characteristics remains an intractable problem for all but the simplest reactions. Adaptive femtosecond control has proved to be a powerful alternative strategy[11–14].

In adaptive femtosecond control, a learning algorithm uses experimental feedback to change the parameters defining the laser pulse shape and thereby iteratively approaches the desired control objective, effectively solving the Schrödinger equation in real time[12]. This approach circumvents the need for detailed knowledge of the nonlinear response of the molecule to the laser field, but the complexity of the resulting optimal pulses often obscures the mechanism driving the control. Disentangling the pulse complexities to arrive at mechanistic insight remains relatively rare (for example refs 14–16), especially in the strong-field regime and in experiments that lack precise spectroscopic feedback signals. Improving the understanding of the control mechanism provides fundamental information about the complex laser-molecule dynamics, thus revealing behaviour that will build the physical intuition necessary to properly parameterize the large multi-dimensional phase space defining the pulse shape[17,18].

The learning algorithm often needs several thousand trial pulses to converge on a solution, and therefore often a simple product yield (for example, time-of-flight mass spectrometry) is employed to obtain rapid feedback. Although these signals can be obtained quickly, the control target is often ambiguous. Moreover, most successful examples of reverse engineering the pulse characteristics involve the interplay between careful parameterization of the search space and detailed spectroscopic feedback[14,15,19], whereas similar attempts using ion yields have been less successful[18]. Various multi-dimensional ion imaging techniques can provide spectroscopic level discernment[20,21], but they have been too slow for adaptive control and have not been implemented so far.

In this Article, we demonstrate the use of a rapid three-dimensional (3D) momentum imaging technique that is incorporated directly into the feedback loop for adaptive control of molecular dynamics. Two primary examples are presented. In the first, image-based feedback allows manipulation of the angular distributions of photofragments arising from strong-field ionization of ethylene, a non-linear molecule with a rich spatial pattern. This example demonstrates the ability of 3D image-based feedback to target and control objectives that are not typically accessible using standard time-of-flight or spectroscopic techniques. In the second example, we control the isomerization dynamics in the doubly charged ions of acetylene. Beyond the control itself, the 3D image-based feedback has stimulated theoretical calculations that identify the barrier-suppression mechanism responsible for increasing the isomerization yield. Furthermore, this control solution has proved robust, with different searches reaching essentially similar pulse characteristics despite different pulse parameterization schemes. On the basis of this range of initial results, we surmise that the use of multi-dimensional momentum feedback opens new avenues for exploration using adaptive control, especially in complex systems or when spectroscopic feedback is impractical.

Results

Experiment. As detailed in the Methods section, the image-based feedback was obtained by employing velocity map imaging (VMI)[22] in combination with a rapid inversion algorithm for online 3D feedback. Although past work has combined strong field pulse shaping with imaging[23–25], and a few previous efforts[26–29] used VMI for adaptive control, they were exclusively based on raw images, in which the 3D momentum distributions were projected onto the two-dimensional (2D) detector plane. The azimuthal ambiguity inherent in such raw, 2D images complicated the extraction of a robust feedback signal[26]. Previous inversion methods to obtain slices through the 3D momentum distribution were often too slow to be practical for adaptive control or depended critically on selecting initial parameters (such as the correct basis set for transformation) before the inversion. By implementing a rapid onion-peeling algorithm[30], the inversion time for a $1{,}050 \times 1{,}024$ pixel image was reduced to less than one second, thus enabling 3D momentum feedback for adaptive control.

Ethylene. Our first control example applies 3D image-based feedback to strong-field ionization of ethylene, specifically the complex angular dependence of $C_2D_3^+$ ions produced by deuterium atom elimination ($n\omega + C_2D_4 \rightarrow C_2D_3^+ + D$). This process produces the inner four-lobed structure, shown in Fig. 1a, whereas the outer ring structure has a momentum that matches a similar structure on the D^+ VMI data, suggesting that it is associated with the double ionization channel ($n\omega + C_2D_4 \rightarrow C_2D_3^+ + D^+$). As the lobes associated with $C_2D_3^+ + D$ are neither perpendicular nor parallel to the polarization direction, extracting this weak channel from time-of-flight mass spectrometry would be difficult. Even the use of raw, 2D VMI is problematic, as azimuthal contributions from the dominant outer double-ionization ring would obscure the inner structure. The 3D momentum feedback allows extraction of the angle-resolved yield from the regions shown in Fig. 1a, which subsequently define the control objective.

The control objective, $\alpha \equiv N_I/N_{II}$, was defined in terms of a ratio of the yields (N) in the two regions (labelled I and II) shown in Fig. 1a. Optimizing α, or selecting laser pulse shapes to shift the angular distributions towards the polarization direction, led to a 65% enhancement of the control objective. This increase was 13 times greater than the level of random fluctuations in the experiment (σ). The resulting angular distribution is shown in Fig. 1b. Moving the angular distribution away from the polarization angle (that is, optimizing α^{-1}) as shown in Fig. 1b, proved harder, with an enhancement of 22% (6σ).

Acetylene. The second example of the 3D image-based control technique involves strong-field isomerization of acetylene dications. Isomerization is monitored by examining the CH_2^+ and CH^+ ion images from the laser-induced fragmentation of the molecule. Previous coincidence measurements[31,32] indicated that CH_2^+ ions are associated with a vinylidene-like configuration of the dication, whereas CH^+ ions are the result of double ionization leading to a symmetric $CH^+ + CH^+$ breakup from the acetylene configuration. The migration of the hydrogen in the former process imparts a significant angular momentum to the molecule, producing a nearly isotropic distribution of ions[32]. The symmetric breakup of acetylene-like $[HCCH]^{2+}$, however, occurs predominately along the laser polarization direction. The CH_2^+ and CH^+ angular distributions obtained in our experiments are displayed in Fig. 2, showing the probability density as a function of both the fragment kinetic energy release (KER) and $\cos\theta$, where θ is the angle between the ion momentum

© 2013 Macmillan Publishers Limited. All rights reserved.

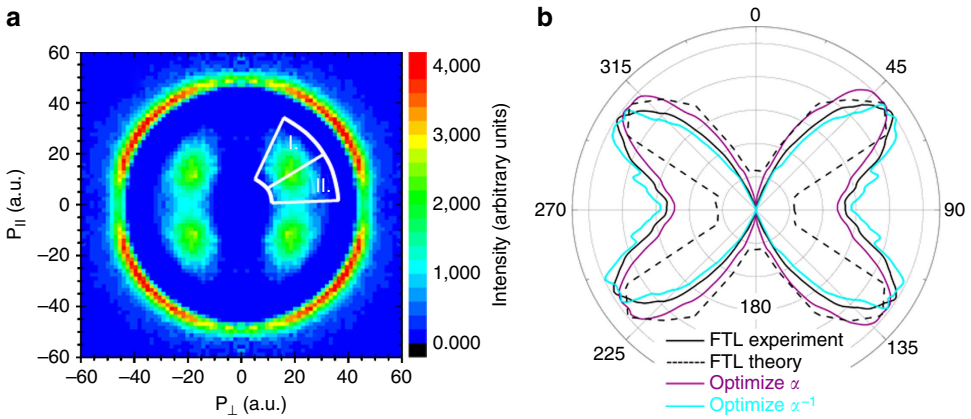

Figure 1 | $C_2D_3^+$ photofragment image and angular distribution. (**a**) Measured momentum distribution (in atomic units) of $C_2D_3^+$ fragments following ionization by near FTL 45 fs duration laser pulses centred at 782 nm with a peak intensity of 2×10^{15} W cm^{-2}. The laser polarization direction is vertical in all panels. The more intense outer structure has a similar shape and momentum to that observed in the D^+ VMI data, and is therefore assumed to be associated with the $C_2D_3^+ + D^+$ channel. The inner structure has no similar momentum matching partner, and is thus associated with $C_2D_4^+ \rightarrow C_2D_3^+ + D$. The white lines define the two regions from which yields were extracted to determine α, the control objective. (**b**) A comparison of the measured angular distributions for strong-field ionization by different optimized pulses leading to $C_2D_4^+ \rightarrow C_2D_3^+ + D$. Violet represents the distribution obtained by maximizing α and cyan arises from maximizing α^{-1}. In these experiments, α increased by 65% over the value with a FTL pulse. To put this number in context, we note that over the duration of the search process, the fitness value obtained with FTL pulses fluctuated with a standard deviation (σ) of 5% around the average value, and thus the enhancement of σ relative to the value obtained with the near-FTL pulse level equates to 13σ. α^{-1} was increased by 22% or 6σ. In black is the comparison between experimental (solid) and theoretical (dashed) angle-resolved ionization probabilities for the $C_2D_4^+ \rightarrow C_2D_3^+ + D$ process shown in Fig. 1a.

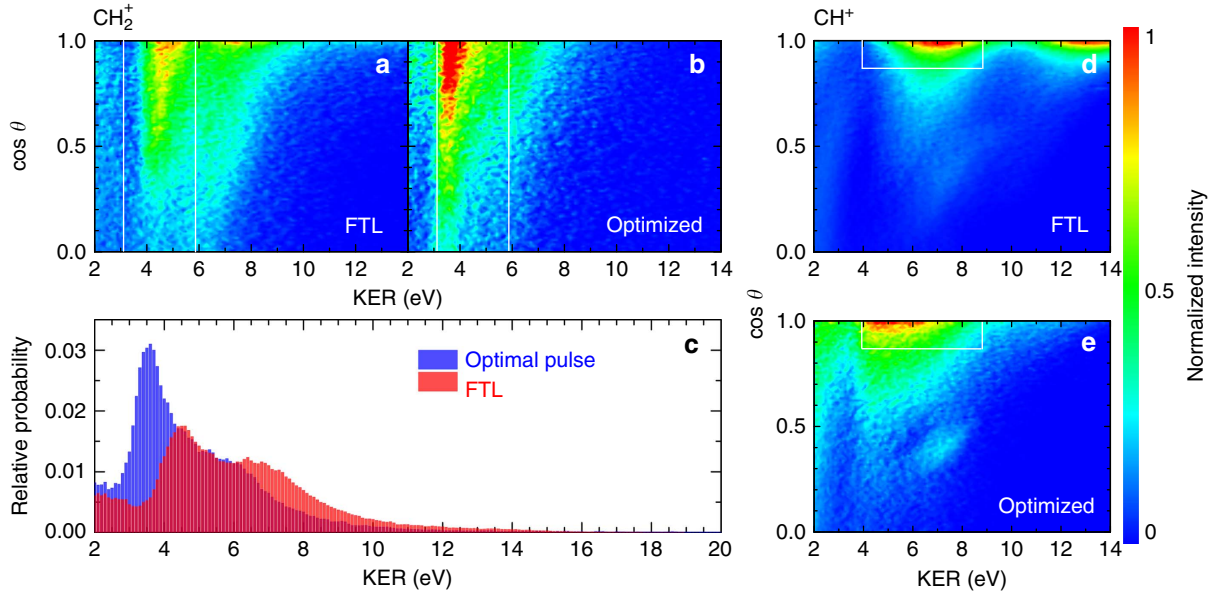

Figure 2 | CH_2^+ and CH^+ photofragment data. Measured density plots of dissociating CH_2^+ (**a** and **b**) and CH^+ (**d** and **e**) ions as a function of KER and cosθ for FTL pulses (**a** and **d**) and pulses optimized to enhance the CH_2^+ channel (**b** and **e**). The white boxes in the density plots define the regions used to obtain the CH_2^+ and CH^+ yields used in the control objective. As shown in (**c**), the probability of dissociation as a function of KER for CH_2^+ ions reveals that laser pulses tailored to enhance the angle-resolved CH_2^+/CH^+ ratio produce CH_2^+ ions with a KER distribution that peaks at more than 1 eV lower than the distribution obtained with FTL pulses. The FTL pulses have a centre wavelength of 778 nm, a FWHM duration of 45 fs and a focused intensity of $\approx 8 \times 10^{14}$ W cm^{-2}. Each density plot is normalized to the peak intensity for that particular exposure and displayed with the same linear colour scale (shown at right) for each image.

and the laser polarization axis. The earlier acetylene work[31,32] suggested that the regions shown by the white lines in Fig. 2a,b,d,e be used to define the vinylidene/acetylene ratio.

The KER distribution of CH_2^+ ions obtained with a Fourier-transform limited (FTL) pulse is peaked at 4.85 eV, consistent with previous coincidence measurements of the $C^+ + CH_2^+$ dissociative double-ionization channel, which show a sharply-peaked distribution near 5 eV that is nearly independent of cosθ (refs 31,32). The CH^+ fragments peaked at around 7 eV along the polarization direction are consistent with previous

© 2013 Macmillan Publishers Limited. All rights reserved.

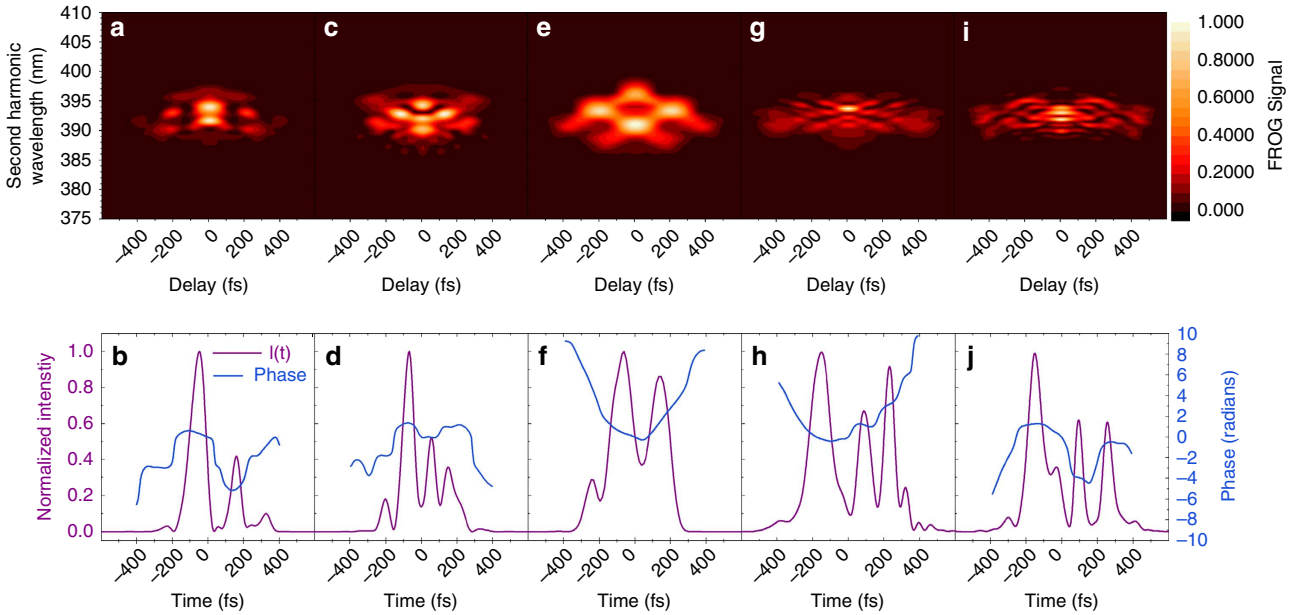

Figure 3 | Laser pulse characterization. SHG FROG[30] measurements (top) and the associated intensity and temporal phase (bottom) for different experimental trials. (**a**,**b**) Optimized pulse using phase-only frequency domain shaping at 68 μJ per pulse obtaining 55% enhancement of the CH_2^+/CH^+ ratio. (**c**,**d**) and (**e**,**f**) are similar but at 130 μJ and again at 68 μJ pulse energy, obtaining 92% and 44% enhancement, respectively. (**g**,**h**) Results from phase-only time-domain shaping at 60 μJ per pulse, obtaining 90% enhancement. The final pulse (**i**,**j**) is manually designed and achieved 40% enhancement.

measurements of the $C_2H_2^{2+}$ dissociation into $CH^+ + CH^+$, whereas the higher KER features are assumed to arise from higher charge states of the parent molecule.

When the learning algorithm was allowed to adjust the pulse shape, the angle-resolved target ratio of CH_2^+/CH^+ could be either almost doubled (40σ) or suppressed to half of the original value (25σ) over a range of laser pulse energies. Interestingly, the KER obtained with the pulse optimized to enhance the isomerization channel showed a downward shift to 3.6 eV and suppression of the high KER feature around 7 eV.

As illustrated in Fig. 3, measurement of these optimized pulses with a SHG FROG[33] showed that the individual pulse characteristics have little similarity aside from a need for multiple peaks spaced by 100–210 fs.

Discussion

The angle-resolved ethylene data, showing increased ionization when the polarization is aligned with the C–D bond, gives insight into the ionization process. In a molecular context, the angular distribution of the strong-field ionization events are often understood in terms of the molecular orbitals involved[34–39]. Early theoretical efforts concentrated on ionization from the HOMO[34], but later studies showed that when occupied valence orbitals have similar energies, both the HOMO and the HOMO-1 states can contribute to the ionization[35–38]. As the energy gap between orbitals decreases in polyatomic molecules, more orbitals are expected to contribute.

The pattern shown in Fig. 1a can be understood by extending the calculations of angle-resolved ionization rates of diatomic molecules, described in ref. 39, to polyatomic molecules. The neutral C_2D_4 molecules in our effusive jet source are randomly oriented, and thus the interaction between the laser field and the electronic wavefunction depends on their relative angle. When the laser polarization is either parallel or perpendicular to the C=C backbone, the HOMO, LUMO and HOMO-1 orbitals are only slightly distorted. When the laser polarization is aligned with the C–D bond direction, however, the electron density becomes much more pliable. The result is a strongly distorted Rydberg orbital located near the deuterium atom. In this configuration, the field easily shifts electron density in that direction and the ionization rate correspondingly increases. As shown in Fig. 1b, the measured and calculated angle-resolved ionization probabilities are in reasonable agreement for FTL pulses. From a control perspective, then, modification of the angular distribution of $C_2D_3^+$ fragments is related to the ability of the pulse to influence the location of this Rydberg orbital. Without image-based feedback, this task would be impossible. Moreover, the $C_2D_3^+$ images provide experimental verification of the theoretical predictions suggesting that multiple orbitals, including the distorted Rydberg orbital, have important roles in the ionization of unsaturated hydrocarbons.

In a larger sense, this example is significant because it illustrates the link image-based feedback can provide between tunnelling ionization and molecular structure. The lobe structures in this example should be present at appearance intensities because the tunnelling rates are highest where the electron cloud has the largest extent[34]. Dissociation channels such as $n\omega + C_2D_4 \rightarrow C_2D_3^+ + D$ that are energetically accessible at the lowest intensity are therefore the best channels for probing and learning how to control molecular structure. Extending this link to the pulse characteristics in this case is still under investigation. Enhancing α was accomplished via a pulse that had some modulation of the spectral intensity but was only slightly longer in duration than the FTL pulse. The pulse that maximized α^{-1} has complicated phase characteristics and a more complex structure.

In the acetylene experiment, however, the image-based feedback stimulated model calculations that yielded an understanding of the mechanism driven by the optimized laser pulse. To shed light on the molecular dynamics and time scales involved, we performed semiclassical on-the-fly calculations in full dimension

© 2013 Macmillan Publishers Limited. All rights reserved.

for the doubly charged acetylene ion. The simulation started just after the ionization event and included the $X^3\Sigma_g^-$ ground state and the first singlet state $^1\Delta_g$ of $C_2H_2^{2+}$. Interactions with both FTL and optimized laser fields were considered. The details for the full dimension trajectory calculations are given in the Methods section. To visualize the dynamics, the full dimension trajectories have been projected onto a 2D PES spanned by the most significant reaction coordinates. This reaction PES includes all critical points, such as minima and barriers along the pathway, and shows both fragmentation channels used as the defined control objective (CH_2^+/CH^+). The first coordinate corresponds to the H migration, which can be followed in the CCH angle. The second coordinate is the CC distance leading to either the $CH_2^+ + C^+$ or $CH^+ + CH^+$ fragmentations, depending on the CCH angle. The *ab initio* PES calculation, as well as the on-the-fly trajectories, used high level electron correlation theory and is shown in Fig. 4.

To reach $CH_2^+ + C^+$ fragmentation (e), a molecule starting from the linear configuration (a) has to pass the transition state (b). It forms a vinylidene-like local minimum geometry at (c) before dissociating over a second barrier (d) to the fragments (e). The second pathway leading to the CH^+-fragments includes mostly the CC-bond elongation and is reached after crossing the barrier (f). Two example trajectories for isomerization, projected onto the 2D surface, are shown in Fig. 4 for calculations with (violet line) and without (white line) the optimized laser field. The white trajectory oscillates for some time around the acetylene-like structure (a) before overcoming the barrier to the vinylidene-like geometry. These types of trajectories do not have enough energy to cross the dissociation barrier and either remain in this configuration or return to (a). The violet trajectory moves very swiftly from geometry (a) over the suppressed barrier (b) to (c) and finally dissociates to (d) without staying long at any given structure.

Most of the more than 1,000 trajectories without the optimized laser interaction stayed at structure (a) or moved between (a) and (c). Between 100 and 210 fs, trajectories with geometry (c) had the highest probability. This time period matches the time separation of the sub-pulses in the optimized field, and it appears that the second sub-pulse is timed to interact when most molecules are in configuration (c). The laser interaction shifts the PES, suppressing the dissociation barrier towards the CH_2^+ fragments, allowing molecules with lower kinetic energy to cross. The theoretical KER spectrum, shown in Fig. 5, supports this explanation and shows the same shift to a lower KER distribution as observed experimentally. Furthermore, the CH^+ fragments also show a shift to lower KER (see Fig. 2d,e), which can be interpreted as a lowering of the barrier between points (a) and (g) in the PES. This barrier, however, is higher than the barrier between (c) and (d), and thus dissociation from the vinylidene configuration is expected to be favored, consistent with the experimental observations.

To further examine this isomerization mechanism, we employed phase-only shaping with a time-domain pulse parameterization[18], rather than the standard frequency-domain parameterization used in the previously described experiments. In this scheme, our optimal pulse is built out of a series of Gaussian shaped pulses and the parameters controlled by the learning algorithm are the duration, amplitude and separation between the individual pulses. Using this parameterization and a

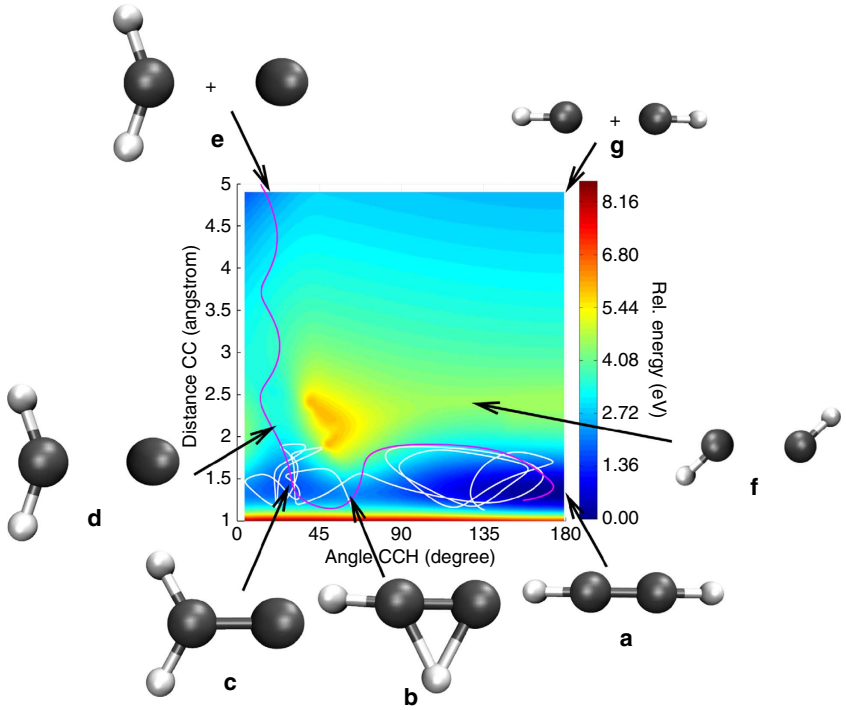

Figure 4 | $C_2H_2^{2+}$ PES and sample trajectories. The 2D PES of the acetylene dication for the two coordinates CCH angle and CC distance. Important geometries (labelled **a**–**g**) are marked on the surface with black arrows linked to corresponding ball-and-stick structures. Point (**a**) on the surface represents the initial linear acetylene state, (**b**) represents the intermediate transition state and (**c**) represents the vinylidene configuration of the $C_2H_2^{2+}$ dication. Dissociation from the vinylidene configuration is shown at points (**d**) and (**e**), whereas direct dissociation from the acetylene configuration proceeds through points (**f**) and (**g**). Two example trajectories are projected onto these coordinates. The white trajectory is calculated without additional laser interaction following the double ionization step and moves only between the structures (**a**) over (**b**) to (**c**). The violet trajectory includes the effect of the optimized laser pulse and progresses from configuration (**a**) over (**b**) to (**c**) and dissociates to (**d**) and finally (**e**) because the laser interaction suppresses the barrier in the region near configuration (**d**).

© 2013 Macmillan Publishers Limited. All rights reserved.

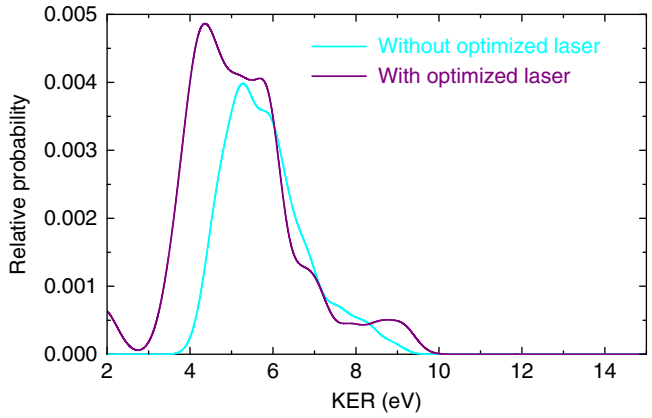

Figure 5 | Calculated KER spectrum for CH_2^+ fragments. In cyan is the probability as a function of KER derived from trajectories evolving without the optimized laser pulse, that is, the calculation assumes that a near-FTL pulse accomplishes the double ionization and the subsequent wavepacket propagation is field-free. In violet is the KER spectrum associated with trajectories evolving in the presence of the optimized laser pulse that modifies the PES. In both the experiment (see Fig. 2c) and calculations, the optimized pulse opens an additional contribution at lower KER.

set of three Gaussian pulses (see Fig. 3g,h), we were again able to double the CH_2^+/CH^+ ratio. The reduced parameter set also converges to a solution much faster (five generations) than the original frequency domain method ($\approx$20 generations). Importantly, the multiple-pulse solution appears general.

The Dazzler pulse shaper[40] can also be used to shape the pulse manually by adjusting laser parameters such as the chirp or pulse duration. Investigations along these lines produced some minimal variation in the CH_2^+ to CH^+ production ratio, but no simple pulse parameter could be manipulated to produce results comparable to those obtained using adaptive control. On the basis of the pulse-train features we observed in pulses optimized to enhance the isomerization ratio in acetylene, we manually designed a pulse with these important characteristics. Although it exceeded the transform-limited result, our pulse did not perform as well as the algorithm-based optimal pulse. The manually-constructed pulse train, shown in Fig. 3i,j), produced a CH_2^+/CH^+ ratio 40% higher than the FTL value at 60 μJ/pulse, whereas various optimized pulses reached 90% or a greater enhancement of the ratio. Still, this result demonstrates that the 3D VMI-based feedback contains enough clues about the control dynamics to interpret the essential features of the pulse, even without using complicated numerical methods such as principal control analysis[18,41,42]. This allowed the selection of a reduced parameter set that provided as much control as the larger original basis. Gaining enough mechanistic insight to understand how to choose a useful parameter space is a key step for improving control fidelity.

To verify the need for 3D momentum imaging feedback for achieving this result, we have performed the acetylene experiment using regions of the images designed to mimic a mass spectrometer with a small solid angle. In these experiments, an enhancement of the CH_2^+/CH^+ ratio was observed, but the result was an angular discrimination artifact, similar to what has been observed for the strong-field dissociative ionization of CO[26]. The use of the full momentum imaging as a feedback for the coherent control algorithm was thus crucial in finding the barrier-suppression mechanism.

Some of the most exciting examples of adaptive control (for example refs 14,15,43,44) depend on very specific optical feedback. Collectively, the examples described above show that 3D momentum imaging feedback brings similar capabilities to ion-based experiments. The twin benefits of this approach are illustrated in our experiments: first, 3D image-based control allows the selection of well-defined control targets; second, the abundant information contained in the feedback signal can give insight into the control mechanism. In the acetylene example, the adaptive search persistently arrived at the multi-pulse barrier-suppression isomerization mechanism despite different initial parameterizations of the search space. This insensitivity to the initial parameterization indicates a high degree of control fidelity. The ethylene examples illustrate how angle-resolved feedback is crucial for the control of polyatomic systems. The general applicability of full momentum-imaging-based feedback for the adaptive control of chemical reaction dynamics promises to uncover novel control mechanisms for even more complex chemical reactions. Furthermore, strong-field processes in atoms, clusters and nanoparticles may be selectively controlled, and the resulting images may provide richly detailed information about the control mechanisms.

Methods

General experimental details. The core of the experiment was a closed-loop system that produces shaped, intense ultrafast laser pulses, which ionize and fragment the target molecules, producing a feedback that drives the optimization of the pulse shapes. The intensity of these pulses was sufficient to ionize either acetylene or ethylene multiple times and produce transient modifications of their PESs. The resulting photofragments were imaged with a VMI apparatus. This ion image was processed online (as described later) and a particular 'fitness' value was extracted, which was used by the learning algorithm to produce a new set of pulse shapes for testing. The Dazzler pulse shaper may be operated in modes that shape either the spectral phase or amplitude independently or together. In these experiments, we only shaped the phase, and thus the pulse energies remained approximately constant over the duration of an experiment. The system was linked by a computer control that connected the AOPDF pulse shaper, the learning algorithm, the digital delay generator that triggered the high-voltage switch for the microchannel plates (MCPs) and the camera readout electronics. This is illustrated schematically in Fig. 6.

Rapid inversion. In this control scheme, accurate feedback from the velocity map image, in the form of an ion yield from a particular portion of the image, often depends critically on the conversion of the 2D raw image to a slice through the centre of the full 3D momentum distribution. An example is displayed in Fig. 7, which shows the raw and inverted images of CD_3^+ ions produced in a laser-ethylene interaction. Although the outer structure is visible in the raw image on the left, the inner structure is nearly completely obscured by an unwanted azimuthal contribution that can easily lead to sub-optimal control results[26].

Mathematically, given the cylindrical symmetry conveniently provided by the laser polarization axis, accomplishing the image inversion requires performing an inverse Abel transformation[22,45–47]. A number of numerical methods for solving this problem exist, but not all of them are useful for this rapid online inversion owing to the additional constraints of the adaptive control loop. First, as a typical experiment contains a few thousand trial pulses, the inversion cannot take much longer than the image acquisition time. Ideally, the inversion time will be much shorter. Second, as the image features are not known ahead of time, methods that require manual selection of initial parameters (such as an appropriate basis set) are difficult to implement. Finally, the inversion process should avoid introducing noise that compromises the feedback.

Inversion selection and speed tests. With these constraints in mind, it is worth reviewing a few options. Fourier–Hankel-based methods[48,49] can be quite rapid but can often result in increased noise, especially near the centre of the image where the Bessel function oscillates rapidly[22]. Several methods, such as BASEX[50] and pBASEX[51], take advantage of the fact that some functions have known inverse Abel transformations. These methods have several advantages, including a relocation of the centerline noise common to the Abel methods to the centre point of the image, relatively rapid computation and smooth final images. The main drawback for our application is that they require the selection of a basis set before the experiment. An alternative approach, which converges to the measured 2D projection by making iterative guesses about the 3D distribution, was developed by Vrakking[52] but is significantly slower. In recent years, several hybrid methods have appeared, including a polar onion peeling (POP)[53] approach that uses a basis set technique similar to BASEX, and an approach that combines BASEX-like features with the iterative approach[54]. These also had undesirable features for our online processing application, primarily the need to set initial values of some kind. In addition, the

© 2013 Macmillan Publishers Limited. All rights reserved.

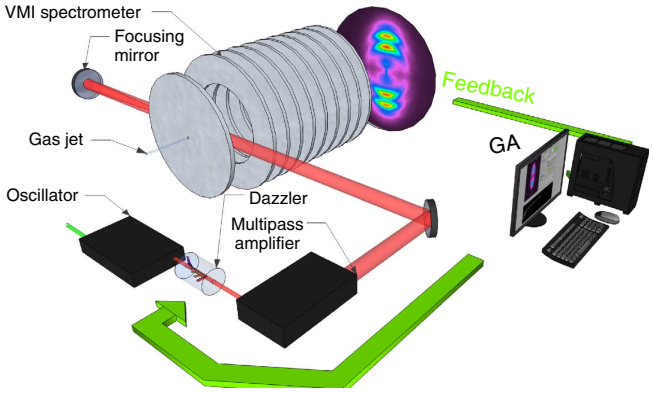

Figure 6 | Schematic diagram of the apparatus and the control loop. Laser pulses centered at approximately 780 nm were produced with a Ti:sapphire oscillator, shaped with an acousto-optical programmable dispersive filter[37] and then amplified to energies typically between 0.01 and 0.5 mJ per pulse by a multipass amplifier running at 2 kHz. The near-FTL pulses had durations of approximately 40–45 fs and, after they were focused by a ($f = 75$ mm) spherical mirror, achieved peak intensities of approximately 2×10^{16} W cm^{-2}. The pulses intersected an effusive jet of target gas, similar to the one described in ref. 42. The spectrometer electric fields were configured so that trajectories corresponding to a particular initial velocity arrived at the same position on the detector plane, even if the ions had been created at different locations within the laser focus[43]. The ions struck the detector MCP stack, producing an electron shower on a phosphor screen that was imaged by a CCD camera. The MCP assembly was fully powered only at times corresponding to the arrival of a single preselected ion species using a triggered high-voltage switch. The image was processed and the feedback delivered to the learning algorithm, which created the next set of pulse shapes to test.

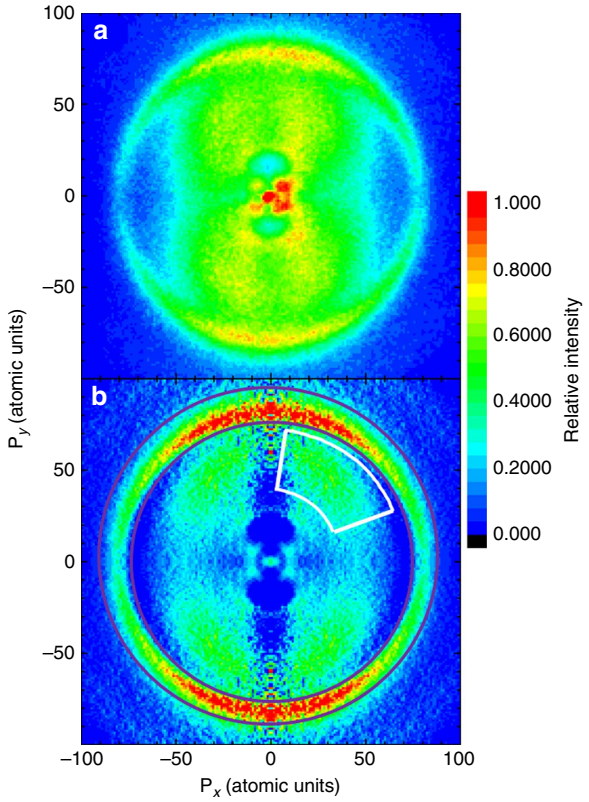

Figure 7 | Comparison of raw 2D and processed 3D images. The raw (**a**) and rapidly inverted (**b**) images for CD_3^+ ions. The inversion was accomplished with the 'onion-peeling' or 'back-projection' method described in this section. The purple and white boxed regions in (**b**) illustrate how different processes could be isolated from the CD_3^+ images and the corresponding yields used to define a control objective. On a 661×661 pixel test image, our algorithm could produce an inverted image in 50 ± 5 ms, compared with 1.5 s for pBASEX[51], 4.86 s for POP[53] and 174 s for the iterative procedure[52]. For a full-sized 1040×1054 pixel image, the inversion time was still only around 600 ms, well below the image acquisition time. Additional efficiency was gained by separating the image acquisition and analysis steps. Thus, while one image was being acquired, the previous image was being inverted. As the exposure time is almost always longer than the image processing time, the overall time for the experiment was not affected by the addition of the inversion step into the control loop.

POP algorithm produced negative values in our tests, which significantly complicates the determination of a yield-based fitness value.

For these reasons, we selected the well-known 'onion-peeling' or 'back-projection' method[22,30]. Although this technique does result in some centerline noise, it is typically less significant than with the Fourier–Hankel methods, and the noise can be reduced to minimal levels. Importantly, there are no initial parameters to be specified, other than the centre and size of the image. Our implementation was derived from the algorithm described by Bordas and co-workers[30], and the interested reader is directed to their excellent development of the mathematical formalism. Careful optimization of our implementation of this method reduced the computation time for our 661×661 pixel test image to 50 ms, shorter than any other method we tested. The overall image processing time is typically less than the duration of the image acquisition, and therefore the overall time of the experiment is not affected.

Pulse parameterization. In most of these experiments the spectral phase was controlled via sixteen 'genes' spread over the pulse bandwidth. The spectral phases between adjacent gene values are calculated by linear interpolation. The time-domain parameterization method allows the shaped pulse to be built out of a series of n Gaussian-shaped pulses[18]. In an example where the full pulse is composed of three component pulses, eight genes are needed: three amplitudes (a_1, a_2 and a_3), three pulse durations (w_1, w_2 and w_3) and two time delays (t_{12} and t_{13}). To obtain the phase mask needed to produce the desired laser intensity as a function of time while only controlling the spectral phase delay, we used the algorithm developed by Hacker and co-workers[55]. This algorithm rapidly estimates the needed phase mask using a process that iteratively employs a FFT-based approach.

FTL fitness determination. The degree of control is reported with respect to the value of the fitness function obtained with a FTL pulse. Experimentally, between each generation an FTL pulse is tested under the same conditions as the trial pulse. These results are averaged over the entire experiment to produce the baseline value that serves as a comparison for the shaped pulses. The fluctuations in the FTL fitness value obtained during each experiment define σ for that experiment.

Selection of regions of interest. Generally, images of various fragmentation channels are obtained with FTL pulses and these results are used to make an initial selection of a feature for optimization. In the acetylene example, previous results[31,32] were also used to inform our selection. Features will often shift in energy or angular distribution as different laser pulse shapes are applied, so selecting too restrictive of a region for use in calculating the fitness function can lead to difficulties with the search. In fact, too restrictive of a gate on the CH_2^+ image shown in Fig. 2a,b did lead to spurious results by excluding lower KER ions from the fitness calculation. In this particular case, however, extending the gate lower in KER than shown in Fig. 2a,b did not affect the results.

Ethylene calculations. As described more fully in ref. 39, the angular-dependent ionization probabilities for ethylene are calculated based on the electronic structure theory. To describe the interaction between the laser pulse and the molecule, the polarization is fixed and the molecule is rotated around that plane as well as out of the plane, that is, around the C = C bond direction. For each position, the electronic wave function is calculated in the presence of the electric field and the tunnelling probability is deduced for the various orbitals. Ionization from more than a single molecular orbital is treated using a linear combination of the selected orbitals.

Acetylene calculations. The 2D PES of $C_2H_2^{2+}$ ($X^3\Sigma_g^-$) was calculated on the CASSCF[8,10] level with a 6-311++G** basis set using the programme package MOLPRO[56]. The scan was carried out under relaxation of the remaining coordinates. The acetylene trajectories were calculated on the same level of theory

© 2013 Macmillan Publishers Limited. All rights reserved.

and utilized an adapted version of the NewtonX program package[57] for the on-the-fly interface to MOLPRO. Trajectories were calculated for the $X^3\Sigma_g^-$ and $1^1\Delta_g$ states. They show similar topography and can be reached in the ionization process. To include the effect of the remaining laser field after ionization, we first checked for possible interaction pathways via electronic excited states that could be used for laser-based control. No electronic excited states can be reached with the laser frequency (or are symmetry forbidden) for both the singlet and the triplet states of the dication. The possibility of two photon transitions was also considered following the approach of ref. 58, but could be excluded. For the FTL laser pulse we assumed a Wigner distribution in the Franck–Condon region of the molecule with excess energy from the laser distributed in the vibrational modes[59,60]. Here, we assumed that the first half of the laser pulse is needed for ionization. For the optimal laser pulse, we took the experimental field and assumed that ionization occurred around the maximum of the first sub-pulse. After ionization the trajectories started again from individual points of a Wigner distribution in the Franck–Condon region. The remaining laser pulse was then added to the one-electron Hamiltonian at the distinct time steps and was included in the on-the-fly dynamics.

References

1. Zewail, A. H. Femtochemistry: Atomic-Scale Dynamics of the Chemical Bond Using Ultrafast Lasers (Nobel Lecture). *Angew. Chem. Int. Ed.* **39,** 2586–2631 (2000).
2. Baker, S. *et al.* Probing Proton Dynamics in Molecules on an Attosecond Time Scale. *Science* **312,** 424–427 (2006).
3. Lee, H., Cheng, Y.-C. & Fleming, G. R. Coherence Dynamics in Photosynthesis: Protein Protection of Excitonic Coherence. *Science* **316,** 1462–1465 (2007).
4. Carbone, F., Kwon, O.-H. & Zewail, A. H. Dynamics of Chemical Bonding Mapped by Energy-Resolved 4D Electron Microscopy. *Science* **325,** 181–184 (2009).
5. Breusing, M., Ropers, C. & Elsaesser, T. Ultrafast Carrier Dynamics in Graphite. *Phys. Rev. Lett.* **102,** 086809 (2009).
6. Wörner, H. J., Bertrand, J. B., Kartashov, D. V., Corkum, P. B. & Villeneuve, D. M. Following a chemical reaction using high-harmonic interferometry. *Nature* **466,** 604–607 (2010).
7. Krausz, F. & Ivanov, M. Y. Attosecond Physics. *Rev. Mod. Phys.* **81,** 163–234 (2009).
8. Goulielmakis, E. *et al.* Real-time observation of valence electron motion. *Nature* **466,** 739–743 (2010).
9. Monmayrant, A., Weber, S. & Chatal, B. A newcomer's guide to ultrashort pulse shaping and characterization. *J. Phys. B At. Mol. Opt. Phys.* **43,** 103001 (2010).
10. Brixner, T. & Gerber, G. Quantum control of gas-phase and liquid phase femtochemistry. *ChemPhysChem.* **4,** 418–438 (2003).
11. Brif, C., Chakrabarti, R. & Rabitz, H. Control of quantum phenomena: past, present and future. *New J. Phys.* **12,** 075008 (2010).
12. Judson, R. S. & Rabitz, H. Teaching lasers to control molecules. *Phys. Rev. Lett.* **68,** 1500–1503 (1992).
13. Assion, A. *et al.* Control of chemical reactions by feedback-optimized phase-shaped femtosecond laser pulses. *Science* **282,** 919–922 (1998).
14. Herek, J. L., Wohlleben, W., Cogdell, R. J., Zeidler, D. & Motzkus, M. Quantum control of energy flow in light harvesting. *Nature* **417,** 533–535 (2002).
15. Daniel, C. *et al.* Deciphering the reaction dynamics underlying optimal control laser fields. *Science* **299,** 536–539 (2003).
16. Trallero, C., Pearson, B. J., Weinacht, T., Gillard, K. & Matsika, S. Interpreting ultrafast molecular fragmentation dynamics with *ab initio* electronic structure calculations. *J. Chem. Phys.* **128,** 124107 (2008).
17. Roslund, J. & Rabitz, H. Experimental quantum control landscapes: Inherent monotonicity and artificial structure. *Phys. Rev. A* **80,** 013408 (2009).
18. Wells, E. *et al.* Closed-loop control of intense-laser fragmentation of S_8. *Phys. Rev. A* **72,** 063406 (2005).
19. Hornung, T., Meier, R. & Motzkus, M. Optimal control of molecular states in a learning loop with a parameterization in frequency and time domain. *Chem. Phys. Lett.* **326,** 445–453 (2000).
20. Ullrich, J., Moshammer, R., Dorn, A., Dörner, R., Schmidt, L.Ph.H. & Schmidt-Böcking, H. Recoil-ion and electron momentum spectroscopy: reaction-microscopes. *Rep. Prog. Phys* **66,** 1463–1545 (2003).
21. Vredenborg, A., Roeterdink, W. G. & Jannssen, M. H. M. A photoelectron-photoion coincidence imaging apparatus for femtosecond time-resolved molecular dynamics with electron time-of-flight resolution of $\sigma = 18$ ps and energy resolution $\Delta E/E = 3.5\%$. *Rev. Sci. Instrum.* **79,** 063108 (2008).
22. Whitaker, B. J. *Imaging in Molecular Dynamics: Technology and Applications* (Cambridge University Press, 2003).
23. Geißler, D., Rozgonyi, T., González-Vázquez, González, L., Marquetand, P. & Weinacht, T. C. Pulse-shape-dependent strong-field ionization viewed with velocity-map imaging. *Phys. Rev. A* **84,** 053422 (2011).
24. Irimia, D. & Janssen, M. H. M. Toward elucidating the mechanism of femtosecond pulse shaping control in photodynamics of molecules by velocity map photoelectron and ion imaging. *J. Chem. Phys.* **132,** 234302 (2010).
25. Natan, A. *et al.* Quantum control of photodissociation by manipulation of bond softening. *Phys. Rev. A* **86,** 043418 (2012).
26. Jochim, B. *et al.* Velocity map imaging as a tool for gaining mechanistic insight from closed-loop control studies of molecular fragmentation. *Phys. Rev. A* **83,** 043417 (2011).
27. Chen, G.-Y., Wang, Z. W. & Hill, III W. T. Adaptive control of the CO_2 bending vibration: Deciphering field-system dynamics. *Phys. Rev. A* **79,** 011401(R) (2009).
28. Krug, M. *et al.* Coherent strong-field control of multiple states by a single chirped femtosecond laser pulse. *New J. Phys.* **11,** 105051 (2009).
29. Ghafur, O., Rouzée, A., Gijsbertsen, A., Siu, W. K., Stolte, S. & Vrakking, M. J. J. Impulsive orientation and alignment of quantum-state-selected NO molecules. *Nat. Phys.* **5,** 289–293 (2009).
30. Bordas, C., Faulig, F., Helm, H. & Huestis, D. L. Photoelectron imaging spectrometry: Principle and inversion method. *Rev. Sci. Instrum.* **67,** 2257–2268 (1996).
31. Alnaser, A. S. *et al.* Momentum-imaging investigations of the dissociation of D_2^+ and the isomerization of acetylene to vinylidene by intense short laser pulses. *J. Phys. B At. Mol. Opt. Phys.* **39,** S485–S492 (2006).
32. Hishikawa, A., Matsuda, A., Fushitani, M. & Takahashi, E. J. Visualizing Recurrently Migrating Hydrogen in Acetylene Dication by Intense Ultrashort Laser Pulses. *Phys. Rev. Lett.* **99,** 258302 (2007).
33. Trebino, R. *Frequency-Resolved Optical Gating: The Measurement of Ultrashort Laser Pulses* (Kluwer Academic, 2002).
34. Tong, X.-M., Zhao, Z. & Lin, C. D. Theory of molecular tunneling ionization. *Phys. Rev. A* **66,** 033402 (2002).
35. Alnaser, A. S. *et al.* Effects of molecular structure on ion disintegration patterns in ionization of O_2 and N_2 by short laser pulses. *Phys. Rev. Lett.* **93,** 113003 (2004).
36. McFarland, B. K. *et al.* High Harmonic Generation from Multiple Orbitals in N_2. *Science* **322,** 1232–1235 (2008).
37. Znakovskaya, I. *et al.* Attosecond control of electron dynamics in carbon monoxide. *Phys. Rev. Lett.* **103,** 103002 (2009).
38. Smirnova, O. *et al.* High harmonic interferometry of multi-electron dynamics in molecules. *Nature* **460,** 972–977 (2009).
39. Von den Hoff, P. *et al.* Effects of multi orbital contributions in the angular-dependent ionization of molecules in intense few-cycle laser pulses. *Appl. Phys. B* **98,** 659–666 (2010).
40. Verluise, F., Laude, V., Cheng, Z., Spielmann, C. H. & Tournois, P. Amplitude and phase control of ultrashort pulses by use of an acousto-optic programmable dispersive filter: pulse compression and shaping. *Opt. Lett.* **25,** 575–577 (2000).
41. White, J. L., Pearson, B. J. & Bucksbaum, P. H. Extracting quantum dynamics from genetic learning algorithms through principal control analysis. *J. Phys. B At. Mol. Opt. Phys.* **37,** L399–L405 (2004).
42. Jolliffe, I. T. *Principal Component Analysis,* 2nd edn. (Springer, 2002).
43. Kuroda, D. G., Singh, C. P., Peng, Z. & Kleiman, V. D. Mapping excited-state dynamics by coherent control of a dendrimer's photoemission efficiency. *Science* **326,** 263–267 (2009).
44. Roth, M. *et al.* Quantum Control of Tightly Competitive Product Channels. *Phys. Rev. Lett.* **102,** 253001 (2009).
45. Abel, N. H. *Oeuvres Completes*. (eds Sylow, E. & Lie, S.) (Johnson Reprint Corp., 1988).
46. Dasch, C. R. One-dimensional tomography: a comparison of Abel, onion-peeling, and filtered backprojection methods. *App. Opt.* **31,** 1146–1152 (1992).
47. Bracewell, R. N. *The Fourier Transform and its Applications* (McGraw-Hill, 1978).
48. Smith, L. M. & Keefer, D. R. Abel inversion using transform techniques. *J. Quant. Spectrosc. Radiat. Transfer* **39,** 367–373 (1988).
49. Castleman, W. *Digital Image Processing* (Prentice-Hall, 1979).
50. Dribinski, V., Ossadtchi, A., Mandelshtam, V. A. & Reisler, H. Reconstruction of Abel-transformable images: The Gaussian basis-set expansion Abel transform method. *Rev. Sci. Instrum* **73,** 2634–2642 (2002).
51. Garcia, G. A., Nahon, L. & Powis, I. Two-dimensional charged particle image inversion using a polar basis function expansion. *Rev. Sci. Instrum* **75,** 4989–4996 (2004).
52. Vrakking, M. J. J. An iterative procedure for the inversion of two-dimensional ion/photoelectron imaging experiments. *Rev. Sci. Instrum.* **72,** 4084–4089 (2001).
53. Roberts, G., Nixon, J., Lecointre, J., Wrede, E. & Verlet, J. Toward real-time charged-particle image reconstruction using polar onion-peeling. *Rev. Sci. Instrum.* **80,** 053104 (2009).
54. Renth, F., Riedel, J. & Temps, F. Inversion of velocity map ion images using iterative regularization and cross validation. *Rev. Sci. Instrum.* **77,** 033103 (2006).

© 2013 Macmillan Publishers Limited. All rights reserved.

55. Hacker, M., Stobrawa, G. & Feurer, T. Iterative Fourier transform algorithm for phase-only pulse shaping. *Opt. Express* **9,** 191–199 (2001).
56. Werner, H.-J. *et al.* MOLPRO, version 2006.1, a package of ab initio programs, http://www.molpro.net (2006).
57. Barbatti, M. *et al.* The on-the-fly surface-hopping program system Newton-X: Application to ab initio simulation of the nonadiabatic photodynamics of benchmark systems. *J. Photochem. Photobiol. A* **190,** 228–240 (2007).
58. Honig, B., Jortner, J. & Szöke, A. Theoretical Studies of Two-Photon Absorption Processes. I. Molecular Benzene. *J. Chem. Phys.* **46,** 2714–2727 (1967).
59. Ghafur, O., Siu, W., Johnsson, P., Kling, M. F., Drescher, M. & Vrakking, M. J. J. A velocity map imaging detector with an integrated gas injection system. *Rev. Sci. Instrum.* **80,** 033110 (2009).
60. Eppink, A. T. J. B. & Parker, D. H. Velocity map imaging of ions and electrons using electrostatic lenses: Application in photoelectron and photofragment ion imaging of molecular oxygen. *Rev. Sci. Instrum.* **68,** 3477–3484 (1997).

Acknowledgements

We acknowledge fruitful discussion of these results with Herschel Rabitz and Brett Esry. Augustana College personnel and equipment were funded by the National Science Foundation grant number 0969687 and National Science Foundation/EPSCoR grant number 0903804. JRML operations and personnel (including partial sabbatical leave funding for E.W.) were supported by the Chemical Sciences, Geosciences and Biosciences Division, Office of Basic Energy Sciences, Office of Science, U.S. Department of Energy. M.F.K., R.d.V.-R. and R.S. are grateful for support by the German Science Foundation via the Cluster of Excellence: Munich Center for Advanced Photonics. B.B. and M.F.K. received partial support from the DFG via the grants Kl-1439/2 and Kl-1439/3.

Author contributions

E.W., I.B.-I. and M.F.K. designed the experiment. C.E.R., B.B., P.R.A., M.F.K. and E.W. implemented the rapid inversion. C.E.R., P.R.A. and E.W. constructed the computer control for the experiment. The experiment was carried out by M.Z., C.E.R., B.J., P.R.A., U.A., B.G., S.D., K.D.C., I.B.-I. and E.W. The data analysis and interpretation were done by B.J., E.W., M.Z., M.F.K., R.d.V.-R., R.S. and I.B.-I. R.S. and R.d.V.-R. provided theoretical analysis and calculations. E.W., B.J., K.D.C., M.F.K., R.d.V.-R., R.S. and I.B.-I. wrote the manuscript, and all authors reviewed the manuscript and offered comments.

Additional information

Competing financial interests: The authors declare no competing financial interests.

Reprints and permission information is available online at http://npg.nature.com/reprintsandpermissions/

How to cite this article: Wells, E. *et al.* Adaptive strong-field control of chemical dynamics guided by three-dimensional momentum imaging. *Nat. Comm.* 4:2895 doi: 10.1038/ncomms3895 (2013).

© 2013 Macmillan Publishers Limited. All rights reserved.

4.2 CEP control of directional bond cleavage

Acetylene is a symmetric molecule, so at a first glance it does not seem likely to specifically control the reaction of the left H atom compared to the right H atom. But few-cycle pulses with well-defined waveforms [101] can directly manipulate the wave function of the molecule [102] and it is actually possible to do so. The electric field waveform of a few-cycle laser pulse in the time domain can be written as

$$E(t) = E_0(t)\cos(\omega t + \phi) \tag{4.4}$$

where E_0 is the envelope, ω the carrier frequency, and ϕ the phase between the carrier and the envelope, also called the carrier envelope phase (CEP). Figure 4.1 illustrates the CEP. When $\phi = 0\pi$ (fig. 4.1 green) the maximum of the electric field coincide with the maximum of the envelope. Changing the CEP (fig. 4.1 blue and red) shifts the maximum along the envelope and leads to a different intensity distribution of the field extrema. With an increasing number of optical cycles the difference in the intensity distribution becomes smaller and the influence of the CEP vanishes. Therefore only very short pulses can utilize the CEP.

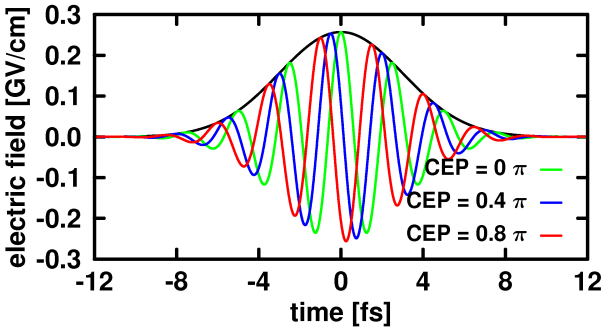

Figure 4.1: Several laser pulses with varying CEP but the same envelope (black), showing the difference in the intensity distribution coming from the absolute phase of the laser field.

The key to understanding why the CEP can control a symmetric reaction stems from a superposition of normal modes, that are used to describe the vibration of the molecule. Assuming there are two relevant normal modes, an infrared (IR) active mode $|n0\rangle$ and an Infrared (IR) inactive mode $|0m\rangle$, spanning a two dimensional space, then the laser can only interact with the IR active mode and imprint its CEP ϕ as factor $e^{-i\phi}$, implicitly including the time evolution factor $e^{-i\frac{E_{n/m}}{\hbar}t}$ in the normal modes. This is even true for a non-resonant excitation, although the population of the IR active mode will go to zero after the full laser pulse. If the molecule is ionized during the laser interaction, then the population of the IR active mode will not vanish in the cationic state. Furthermore the vibrational ground state $|00\rangle$ of the neutral molecule will form a wave packet on the cationic surface, that includes contributions from several cationic modes, but especially the IR inactive mode $|0m\rangle$ will be populated, too. The phase of this wave packet is independent from the CEP, so with the CEP dependent part of the IR active mode contribution, the resulting full wave packet has a basic part that can be written as:

$$\Psi_{\text{basic}} = |01\rangle + e^{-i\phi}|10\rangle \tag{4.5}$$

While almost all of the remaining wave packet shows no preference for either reaction, the basic part Ψ_{basic} leads to a CEP dependent asymmetry, that can be controlled by the sign of the IR active mode. Figure 4.2 visualize this critical basic part for a simple 2D model potential. The left and middle panel shows the $|01\rangle$ and $|10\rangle$ wave packet respectively, while the right panel depicts the positive linear combination $|01\rangle + |10\rangle$.

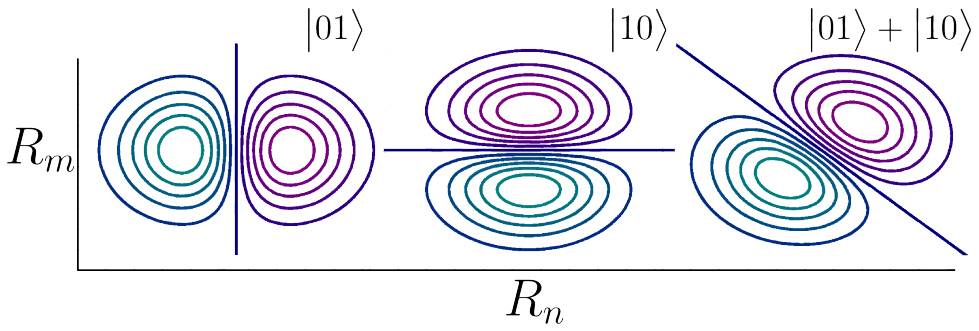

Figure 4.2: 2D representation of the nuclear wave packets $|01\rangle$ and $|10\rangle$ in the left and middle panel respectively. The right panel shows the positive linear combination $|01\rangle + |10\rangle$.

This direct manipulation of the nuclear wave packet with the CEP only works for very short, ideally single cycle, pulses, because the timing of the ionization imprints the phase of the laser to the wave packet. If the laser field has more time points with enough intensity to ionize the molecule, these points will form different wave packets that will average the asymmetry out. The effect relies on the wave function nature of the system and the simulation has to include this. Using the trajectory method from the first section 4.1 would not reproduce the results, because the classical treatment of the nuclear motion does not include the possibility of a phase difference in the wave packet. On the next pages the article "Subfemtosecond steering of hydrocarbon deprotonation through superposition of vibrational modes" published in *Nature Communications* is reprinted with permission from *Nat. Commun.* **5** 3800 (2014).

nature COMMUNICATIONS

ARTICLE

Received 21 Dec 2013 | Accepted 3 Apr 2014 | Published 8 May 2014

DOI: 10.1038/ncomms4800

Subfemtosecond steering of hydrocarbon deprotonation through superposition of vibrational modes

A.S. Alnaser[1,2,3], M. Kübel[4], R. Siemering[5], B. Bergues[2], Nora G. Kling[6], K.J. Betsch[2], Y. Deng[2], J. Schmidt[4], Z.A. Alahmed[3], A.M. Azzeer[3], J. Ullrich[7,8], I. Ben-Itzhak[6], R. Moshammer[7], U. Kleineberg[4], F. Krausz[2,4], R. de Vivie-Riedle[5] & M.F. Kling[2,4,6]

Subfemtosecond control of the breaking and making of chemical bonds in polyatomic molecules is poised to open new pathways for the laser-driven synthesis of chemical products. The break-up of the C-H bond in hydrocarbons is an ubiquitous process during laser-induced dissociation. While the yield of the deprotonation of hydrocarbons has been successfully manipulated in recent studies, full control of the reaction would also require a directional control (that is, which C-H bond is broken). Here, we demonstrate steering of deprotonation from symmetric acetylene molecules on subfemtosecond timescales before the break-up of the molecular dication. On the basis of quantum mechanical calculations, the experimental results are interpreted in terms of a novel subfemtosecond control mechanism involving non-resonant excitation and superposition of vibrational degrees of freedom. This mechanism permits control over the directionality of chemical reactions via vibrational excitation on timescales defined by the subcycle evolution of the laser waveform.

[1] Physics Department, American University of Sharjah, POB26666 Sharjah, UAE. [2] Max-Planck-Institut für Quantenoptik, D-85748 Garching, Germany. [3] Department of Physics & Astronomy, King-Saud University, Riyadh 11451, Saudi Arabia. [4] Department für Physik, Ludwig-Maximilians-Universität München, D-85748 Garching, Germany. [5] Department für Chemie und Biochemie, Ludwig-Maximilians-Universität München, 81377 München, Germany. [6] J. R. Macdonald Laboratory, Physics Department, Kansas-State University, Manhattan, Kansas 66506, USA. [7] Max-Planck-Institut für Kernphysik, D-69117 Heidelberg, Germany. [8] Physikalisch-Technische Bundesanstalt, D-38116 Braunschweig, Germany. Correspondence and requests for materials should be addressed to A.S.A. (email: aalnaser@aus.edu) or to M.F.K. (email: matthias.kling@lmu.de).

© 2014 Macmillan Publishers Limited. All rights reserved.

The nuclear kinematics that are responsible for making and breaking chemical bonds occur on femtosecond timescales[1]. The steering of chemical reactions has been demonstrated for a variety of systems in the gas and condensed phase using modulated light fields[2–6], with the amplitude, phase and polarization used as a control parameter. Breaking of the hydrogen bonds is one of the most important dynamic reactions in the chemistry related to biology, combustion and catalysis, motivating considerable efforts to monitor and ultimately control the process. It has been studied in great detail, where efficient strong-field-induced proton ejection was reported[7–14]. Dynamic charge localization[11] and concerted fragmentation[12] scenarios were suggested to explain the origin of the high kinetic energies of the ejected protons. These studies corroborated the need for ultrashort light pulses, consisting of a few cycles, for steering the deprotonation process. As an additional challenge, the aforementioned control schemes do not provide means for a bond-specific manipulation of the deprotonation in symmetric hydrocarbons.

Few-cycle pulses with well-defined waveforms[15] offer a new quality of control on direct manipulation of the wavefunction of a molecular system[16]. Few-cycle waveforms with adjustable carrier-envelope-phase (CEP) have permitted control of charge localization in the ionization and dissociation of diatomic molecules on a subfemtosecond timescale[17–21]. The approach has also been successful in altering the yields of ionization and fragmentation in hydrocarbons[13]. Despite its relevance to stereochemistry, that is, the rearrangements of atoms in a molecule, full control of the deprotonation of hydrocarbons, including the directional steering of the emission of the protons, has, however, not been reported.

Here, we demonstrate the subfemtosecond control of the proton-ejection direction from acetylene molecules with the waveform of near-single-cycle laser pulses. On the basis of quantum dynamical calculations, we show that the demonstrated directional control does not originate from electronic motion effects considered so far[16]. Rather, the mechanism is based on the manipulation of the phases of individual components of the multi-mode vibrational wave packet by the laser field in the neutral molecule and cation. While control of vibrational superpositions and their phase after resonant excitation has been performed in the context of molecular vibrational qubits[22,23], the superposition between vibrational modes is formed through a non-resonant process in our study and is controlled on an attosecond timescale. The process described here constitutes a novel mechanism for steering the reactions of complex molecules.

Results

Laser-induced deprotonation of the acetylene dication. The electric field waveform of (transform-limited) few-cycle light pulses can be described as $E(t) = E_0(t)\cos(\omega t + \phi)$, where $E_0(t)$ is the amplitude envelope, ω the carrier angular frequency and ϕ is the CEP. The CEP offers a way to tailor the electric field waveform on subfemtosecond timescales and has proven to be a powerful parameter for steering electron motion[16].

In our present experimental studies on the CEP control of the deprotonation of acetylene, we employ CEP-tagged reaction microscopy (REMI)[24] (for details see the Methods section). The interaction of acetylene molecules with intense few-cycle pulses results in the dissociative ionization and isomerization of the molecule yielding a variety of reaction products[7]. One of the reactions that we concentrate on here is the deprotonation of acetylene after two consecutive ionization steps, see Fig. 1a, where a 1D cut of the potential energy surfaces (PES) is shown. After

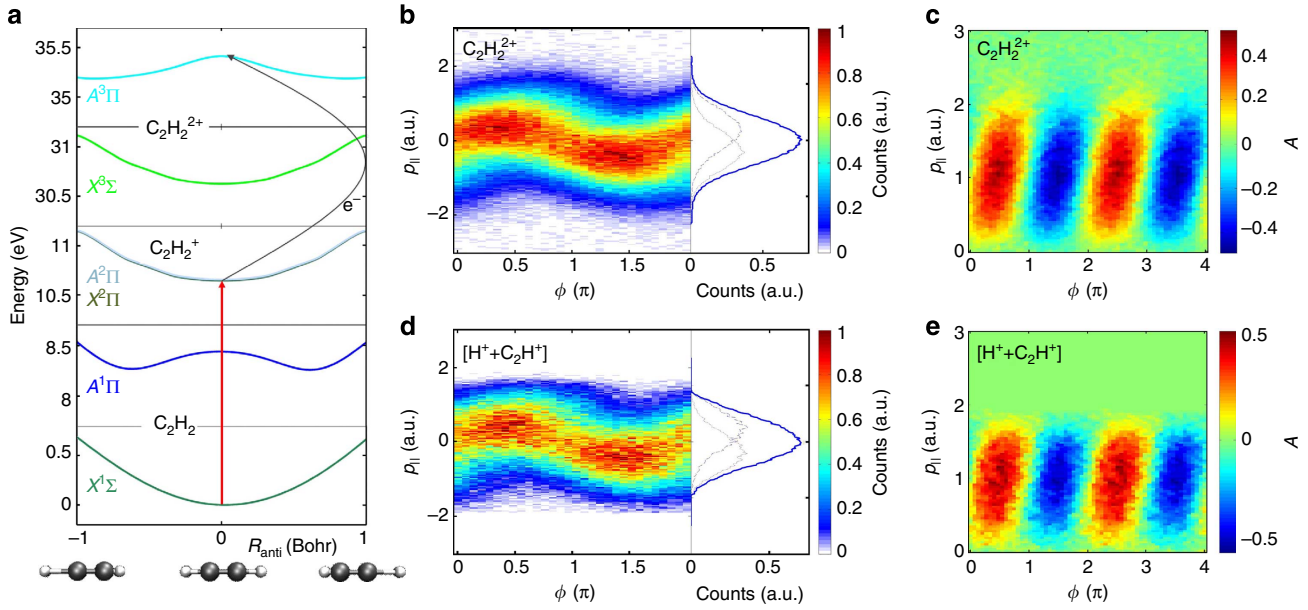

Figure 1 | Generation of the acetylene dication and the deprotonation fragments. (**a**) 1-D cut of potential energy curves of the considered states in the ionization and deprotonation: ground ($X^1\Sigma_g^+$) and first excited state ($A^1\Pi_u$) of the neutral molecule, the cation ground ($X^2\Pi_u$) and degenerate first excited state ($A^2\Pi_u$), and the dication ground ($X^3\Sigma_g^-$) and first excited state ($A^3\Pi_u$) along the anti-symmetric stretching coordinate R_{anti} at $R_{sym} = 0$. The red vertical line indicates the tunnelling ionization and the grey curved line marks the second ionization step by electron recollision. (**b**) Density plot of the acetylene dication longitudinal recoil momentum as a function of the experimental CEP, ϕ, for 4 fs pulses at an intensity of 2×10^{14} W cm^{-2}. CEP-integrated momenta are shown in the right panel. The dashed (dotted) lines shown correspond to CEP's with maximum positive (negative) asymmetry in the ion emission, respectively. (**c**) Density plot for the asymmetry parameter, $A(p_{||},\phi)$, for $C_2H_2^{2+}$ ions. (**d**) Density plot of the vector momentum sum of the recoil of the two (H^+,C_2H^+) deprotonation fragments. (**e**) Density plot of the asymmetry parameter for the momentum sum of the deprotonation fragments (H^+,C_2H^+).

© 2014 Macmillan Publishers Limited. All rights reserved.

population of the first excited state of $C_2H_2^{2+}$, the dication breaks up into H^+ and C_2H^+ fragments, which are detected with the REMI in coincidence.

To confirm the population scenario of the dication, which involves ionization by the laser field followed by subsequent recollisional ionization and excitation (Fig. 1a), high-resolution spectra of the longitudinal (along the laser polarization axis) momentum $p_{||}$ for the doubly charged $C_2H_2^{2+}$ recoil ions as a function of the CEP for 4-fs laser pulses at a peak intensity of 2×10^{14} W cm^{-2} were recorded and are shown in Fig. 1b. Clear modulation of the dication's momentum with the CEP is visible.

To enhance the visibility of CEP-effects, it is useful to define an asymmetry parameter, $A(p_{||},\phi)$, as

$$A(p_{||},\phi) = \frac{N_{pos}(p_{||},\phi) - N_{neg}(p_{||},\phi)}{N_{pos}(p_{||},\phi) + N_{neg}(p_{||},\phi)} \quad (1)$$

with $N_{pos}(p_{||}, \phi)$ and $N_{neg}(p_{||}, \phi)$ representing the yields for positive and negative momentum components $p_{||}$, respectively. The 2-dimensional map in Fig. 1c for the dication shows high-amplitude asymmetry. Corroborated by previous studies on atoms[25] and diatomic molecules[26], the dependence of the recoil-ion momentum on the CEP indicates that the doubly charged ion, at this laser intensity, is formed via an electron recollision process. Here, the free electron created in the first tunnelling event is guided by the laser field, and, for certain CEPs, the electron will return with sufficient energy to ionize the $C_2H_2^+$ ion. Because of momentum conservation during ionization, the momentum sum of the two ionized electrons is equal and opposite to the measured recoil momentum of the $C_2H_2^{2+}$ ion (neglecting the small momentum contribution of the absorbed photons).

The data in Fig. 1b,c indicate that—for the near-single cycle pulses used in the experiment—the electron recollision and the corresponding double ionization and excitation of $C_2H_2^{2+}$ are controlled by the light waveform. This is analogous to previous findings on the non-sequential double ionization of argon with 4-fs pulses[25], where it was shown that electron recollision can be limited to a single event by using sufficiently short, CEP-controlled laser pulses.

Exploiting the applied coincident multi-particle detection scheme, the deprotonation channel has been identified by the coincidence of the H^+ and C_2H^+ fragments following the dissociation of the dication. We can investigate the dependence of their yield on the CEP. Figure 1d,e shows the CEP-dependent momentum sum, p_{sum}, of the coincident H^+ and C_2H^+ fragments parallel to the laser field and the asymmetry that is derived from these data.

A clear CEP dependence is visible in Fig. 1d,e exhibiting the same oscillatory behaviour as seen for the dication. The similarity of the two plots indicates that the recollision process is responsible for the recoil momentum of both the dication and the centre of mass motion of the reaction products after deprotonation.

Directional laser-waveform control of the deprotonation. As a signature of the deprotonation we investigate H^+ fragments from coincident creation of H^+ and C_2H^+ upon the break-up of the dication. Figure 2a,b shows the momentum and asymmetry for H^+ ions. The directional control of the deprotonation reaction becomes visible when analysing the asymmetry of the H^+ emission, which is shown in Fig. 2b. Figure 2c shows the asymmetry parameter $A(\phi)$ that has been integrated over all momenta of the H^+ fragments. The observed preferential CEP-dependent ejection of protons to the left and right of the laser polarization axis illustrates the subfemtosecond steering of the hydrogen ejection.

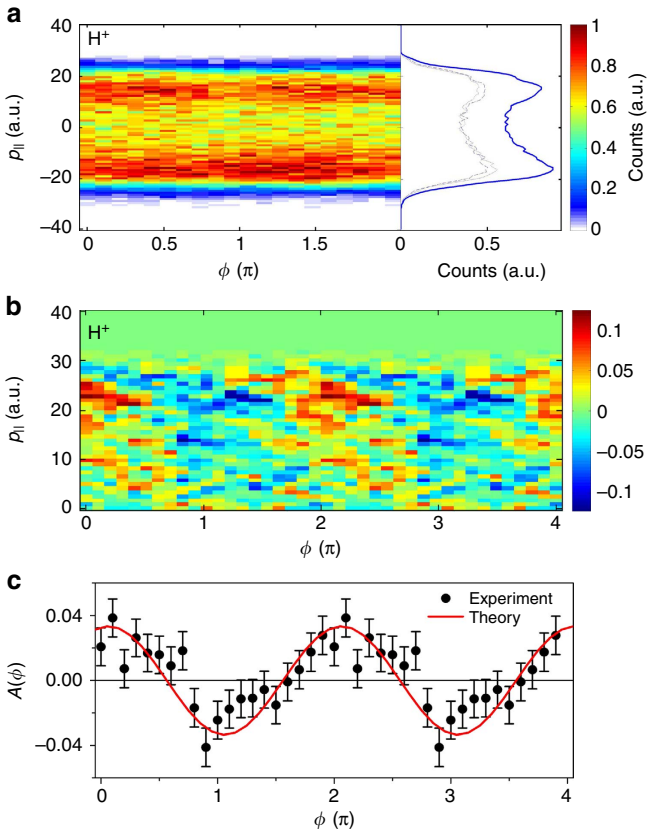

Figure 2 | Subfemtosecond directional control of deprotonation. (**a**) Density plot of the momentum of H^+ fragments as a function of CEP. CEP-integrated momenta are shown in the right panel. The dashed (dotted) lines shown correspond to CEP with maximum positive (negative) asymmetry in the ion emission, respectively. (**b**) Density plot for the asymmetry parameter, $A(p_{||},\phi)$, for the H^+ fragments. (**c**) The asymmetry parameter, $A(\phi)$, integrated over all momenta for H^+ ions. The error bars were derived via error propagation using the s.d. in the ion yields with positive and negative momenta. The clear oscillation in the asymmetry for the directional emission of H^+ fragments as a function of CEP under the given laser conditions demonstrates the CEP-control of the hydrogen emission direction. Also shown is the calculated asymmetry (solid red line) obtained from our quantum dynamical calculations (see text for details), which has been shifted in absolute CEP for best overlap with the experimental data since the absolute CEP is not known from the experiment.

Discussion

To account for the asymmetric deprotonation, the well-known Tannor-Rice control scheme exploiting excited state dynamics[27] might appear to be a first candidate. However, for the current case, where the involved electronic state potentials are symmetric with respect to the deprotonation direction, an additional asymmetry has to be introduced by the laser field. We have performed quantum dynamical calculations to model the relevant molecular dynamics. The details of our calculations are given in the Methods section. The deprotonation of the dication is described in the basis of the symmetric $|0m>$ and anti-symmetric C-H stretching $|n0>$ modes with m, n being the number of vibrational quanta, and $|0m>$ and $|n0>$ implicitly including the respective time evolution factor $e^{-i\frac{E_{m(n)}}{\hbar}t}$. Around the minimum of PES, these modes correspond to the normal modes and their respective overtones. A linear combination of these modes, $1/\sqrt{2}(|0m\rangle \pm |n0\rangle)$, will induce a wave packet

© 2014 Macmillan Publishers Limited. All rights reserved.

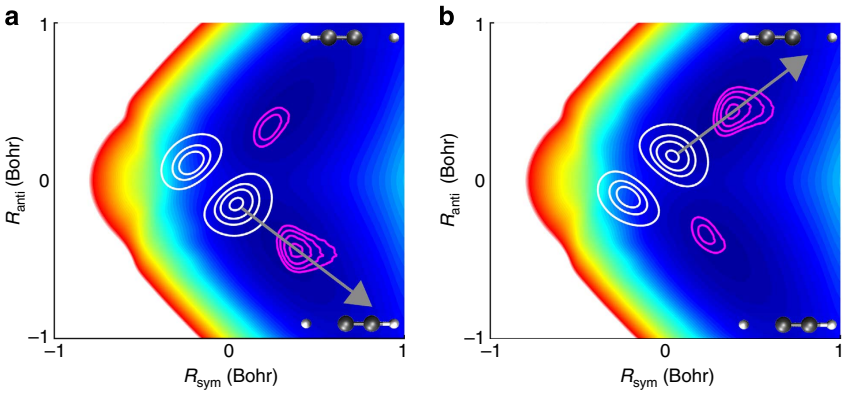

Figure 3 | The relevant first excited state of the dication for deprotonation. The state ($A^3\Pi_u$) is shown as a 2D-surface plotted against the symmetric and anti-symmetric stretching coordinates. The arrows in **a** and **b** indicate the two directions, into which protons can be emitted. To illustrate the control process, we plotted two wave packets representing the ideal superposition of $1/\sqrt{2}(|01\rangle - |10\rangle)$ (**a**) and $1/\sqrt{2}(|01\rangle + |10\rangle)$ (**b**). The initial wave packets are shown by white topographic lines, a snapshot of the same wave packet after 2.4 fs in magenta. The negative superposition (**a**) yields dominant cleavage of the left C-H bond, while the positive superposition (**b**) yields dominant cleavage of the right C-H bond.

motion along either one of the C-H stretching coordinates. When such a wave packet experiences a repulsive potential either the deprotonation of the left or the right H-atom is initiated. Two-dimensional (2D) PES along the normal mode coordinates (R_{sym}, R_{anti}) are calculated for the neutral, cationic, dicationic ground and excited states. The first excited state, the $A^3\Pi_u$ state, of the dication turns out to be the important state for the reaction (see Fig. 1a and Methods section) and its 2D surface is shown in Fig. 3.

From the stretching modes, only the anti-symmetric mode $|10>$ is IR-active, and the incident light field is not resonant with the vibrational transitions. To prepare the required superposition, it is sufficient to address and control only the anti-symmetric $|10>$ mode, via IR transitions. For the given light field, this happens in the neutral and cation. The symmetric mode contributions in the vibrational wave packet occur solely due to the ionization steps. The time-dependent population of the anti-symmetric mode $|10>$ follows the electric field evolution of the few-cycle pulse (see Methods section). The CEP of the pulse imprints a certain phase (φ_{CEP}) on the addressed anti-symmetric mode $|10>(|10>e^{-i\varphi_{CEP}t})$. When the few-cycle pulse is able to modify the phase of the anti-symmetric stretching mode, the sign in the superposition of the symmetric and anti-symmetric modes can be varied with the CEP and exhibits a modulation with a periodicity of 2π.

To mimic the effect of the second ionization including the recolliding electron, the cationic wave packet is projected onto the dication. During the second ionization step, the intensity of the remaining light field is too low to significantly enhance the control of the asymmetric stretching mode $|10>$ components. The main role of the recolliding electron is to provide the energy that is sufficient to reach the excited triplet state $A^3\Pi_u$. The energy of the recolliding electron can be evaluated for the given laser parameters to about 33 eV, corresponding to 3.17 U_p[28] with the ponderomotive potential $U_p = I/(4\omega^2)$ (in atomic units) that depends on the laser intensity I and the angular frequency ω. An electron energy of 25 eV is enough to reach the $A^3\Pi_u$ state of the dication. Because of the significant differences in the potential shape of the dicationic $A^3\Pi_u$ state and the cationic ground state (Fig. 1a), higher vibrational quanta ($|n0>$ and $|0m>$) up to the dissociation limit become now the dominant components of the vibrational wave packet and dissociation of the C-H bond can occur[13]. The preparation of the CEP-dependent features in the vibrational wave packet takes place in the neutral and cation, and is transferred to the dication in the second ionization. We observe that the propagation of the vibrational wave packet in the dication to either one of the dissociative channels ($H^+ + CCH^+$ and $HCC^+ + H^+$, see Fig. 3) can be manipulated by the CEP. Evaluation of the fraction of the wave packet correlating with the individual dissociation channels provides the theoretical asymmetry plotted in Fig. 2c. The theoretical curve shows excellent agreement with the experimental data, which lends support to the described novel subfemtosecond control mechanism.

The presented experimental and theoretical data support a new and very general coherent-control scheme, where the direction of proton ejection in a symmetric hydrocarbon is steered through manipulating the phases of the individual components of the vibrational wave packet. The CEP control-induced mechanism is substantially different from all previous studies, where electronic wave packets dominated the outcomes of the molecular dynamics[16], in the context of which the enhancement of the asymmetry through selection of vibrational states has been reported[29,30]. While in the current proof-of-principle experiment, the degree of control was rather limited, it can be enhanced by using near-single cycle waveforms that are resonant with the optically active mode. With the advent and current development towards the generation of ultrashort, phase-stable light pulses in the mid-infrared[31], substantial improvement of control is within reach. We expect the control scheme to be widely applicable to a variety of chemical processes, where the reactions of not only asymmetric but also symmetric molecules can be manipulated.

Methods

Experimental set-up. Linearly polarized laser pulses with a central wavelength of 750 nm, an energy of 150 μJ and a full width at half maximum of the temporal intensity envelope of 4 fs are generated at a repetition rate of 10 kHz in an amplified laser system. The laser intensity was kept stable on the level of 10%. The CEP of each laser pulse was recorded by sending a fraction of the laser beam (20 μJ) into a single-shot stereographic above-threshold ionization (Stereo-ATI) phase meter[32]. A detailed description of the CEP measurement and CEP tagging techniques can be found in ref. 33. In brief, the time-of-flight spectra of electrons emitted along both directions of the laser polarization axis are recorded on either side of the apparatus. For each laser shot, the CEP is inferred from the asymmetry between the left and the right TOF spectra. Note that the CEP is measured up to a constant offset in the phase meter.

In a recent study, we showed that slow drifts of the laser intensity can markedly affect the results of phase-tagged ionization yield measurements with long acquisition time[34]. To correct for any effects of small drifts of the laser parameters on the CEP measurement, we have applied the procedure outlined in ref. 34, which had been tested to give reliable phase-tagged ion yields for the non-sequential

© 2014 Macmillan Publishers Limited. All rights reserved.

double ionization of argon. The uncertainty in determining the CEP was on the order of 300 mrad during the entire measurement.

A fraction (up to 15 μJ) of the remaining part of the laser beam is focused with a spherical mirror ($f = 25$ cm) into a well-localized (1 mm width) and cold supersonic gas jet of acetylene molecules in the centre of a REMI. Ions and electrons created in the laser focus (40 μm diameter) can be extracted by an electric field towards time- and position-sensitive MCP detectors at the left and right side of the instrument, respectively. In the current experiments, only ion signals were recorded. The ions' impact positions were determined utilizing a two-dimensional delay line anode mounted behind the MCP. Pulses from the ends of the x and y delay lines and a time signal from the microchannel plate were registered by a multi-hit time-to-digital converter and recorded in event mode. From these data, off-line analysis provided the 3D vector momentum of each ionic fragment at the instant of double ionization. The deprotonation fragments are identified and isolated from other fragments by applying tight momentum sum conditions using the coincidence high-resolution PIPICO (Photo-Ion Photo-Ion) spectra[7].

Statistical evaluation of the asymmetry data. To assess the statistical significance of the observed asymmetry, the data were subjected to a statistical test. Asymmetry curves were generated from the data for 1,000 different random re-orderings of the simultaneously recorded CEP values, that is, the CEP measured for an event was randomly associated with a different event before calculating the asymmetry. Any re-ordering should destroy the correlation of the data with the CEP, and those data can therefore be regarded as providing an upper limit for the noise of the measurement. The amplitude of the asymmetry oscillation was extracted from each test curve by a sinusoidal fit of the resulting asymmetry curve and plotted against the R^2 value in Fig. 4, which is defined as:

$$R^2 = 1 - \frac{\sum_i [A(\phi_i) - f(\phi_i)]^2}{\sum_i [A(\phi_i) - \bar{A}]^2} \quad (2)$$

where $\bar{A}$ denotes the mean value of the asymmetry over all bins and $f(\phi_i)$ the fitted asymmetry for bin i. The point corresponding to the true experimental data (non-randomized CEP ordering) is displayed as a blue point indicated by an arrow. It can be seen that this point shows a significantly larger goodness of the fit compared with the randomized test data. Therefore, despite its small amplitude, we conclude that the observed directional emission of protons is statistically significant.

Quantum chemistry methods. PES for ground and excited states of the neutral, cation and dication states of acetylene were calculated on the CASSCF[10,10], [9,10] and [8,10] level of theory, respectively, using the program package MOLPRO[35] with the 6-311++G** basis set as well as the dipole moments and transition dipole moments. Two-dimensional PES were calculated along the symmetric and anti-symmetric stretching coordinate with a step size of 0.05 a.u.. The PES were interpolated to 256 × 256 points for the evaluation of the vibrational eigenstates and the propagation of the vibrational wave packets. In the neutral molecule, only the IR-transitions play a role since the first excited state is separated by 7.8 eV (vertically) or 6.2 eV (adiabatically) and does not influence the ground state wave packet.

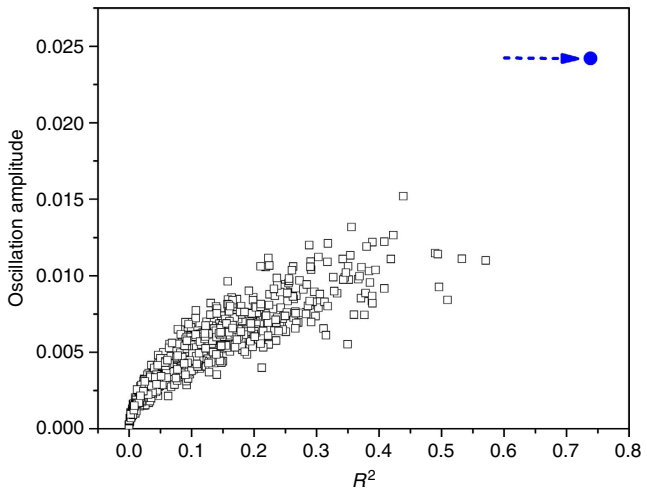

Figure 4 | Statistical evaluation of the asymmetry. In the measured data, the CEPs were randomized and the resulting asymmetry curve was fitted by a sinusoidal to extract the amplitude. This was repeated 1,000 times and the fitted amplitudes and R^2 values (see text) for each are plotted. The true experimental data are displayed as a blue point indicated by an arrow, demonstrating the statistical significance of the observed CEP-dependence.

Wave packet propagation. The Chebychev propagator was used to solve the time-dependent Schrödinger equation. The time-dependent Schrödinger equation for the neutral molecule under the influence of the light field reads:

$$(H_n + \mu_{nn}\varepsilon(t))\Psi_n(t) = \tilde{\Psi}_n(t) \quad (3)$$

with H_n the Hamiltonian of $X^1\Sigma_g^+$, μ_{nn} the associated dipole moment and $\varepsilon(t)$ the near-single cycle laser field.

The light field $\varepsilon(t)$ was included in the dipole approximation:

$$\varepsilon(t) = E_0 \exp\left[-2\left(\frac{t - t_1}{\mathrm{FWHM}/\sqrt{2\ln 2}}\right)^2\right]\cos(\omega_0(t - t_1)) \quad (4)$$

and was characterized by a full width at half maximum of 4 fs with a cycle-averaged intensity of 2×10^{14} W cm^{-2}. The light field was discretized with a time step of 0.024 fs. The part of the laser interaction experienced by the neutral molecule has a duration of 4.8 fs (200 time steps) in correspondence to the time when the intensity maximum is reached and the system is ionized. During that period, the initial superposition is formed. All ionization steps are approximated by setting the vibrational wave packet onto the corresponding ionic state.

In the first ionization step, the vibrational wave packet of the neutral molecule is transferred to the lowest cation states. The first two electronic states ($X^2\Pi_u$ and $A^2\Pi_u$) in the cation are nearly degenerate and we assume an equal distribution over both states in the ionization of the neutral molecule. A second type of interaction with the laser field via electronic transitions back and forth between the states is possible and included for completeness in the total Hamiltonian given below. However, the transition dipole moment between those states is almost non-existent along the deprotonation modes and its effect is negligible. The time-dependent Schrödinger equation for the cation reads:

$$\begin{pmatrix} H_1 + \mu_{11}\varepsilon(t) & -\mu_{12}\varepsilon(t) \\ -\mu_{21}\varepsilon(t) & H_2 + \mu_{22}\varepsilon(t) \end{pmatrix}\begin{pmatrix} \Psi_1(t) \\ \Psi_2(t) \end{pmatrix} = \begin{pmatrix} \tilde{\Psi}_1(t) \\ \tilde{\Psi}_2(t) \end{pmatrix} \quad (5)$$

with H_1, H_2 the Hamiltonians of $X^2\Pi_u$, $A^2\Pi_u$ of the cation, μ_{11}, μ_{22} the associated dipole moments, and μ_{12} the almost zero transition dipole moment.

The dissociation of the wave packet in the excited triplet state $A^3\Pi_u$ of the dication was propagated for 480 fs with time steps of 0.24 fs. The part of the wave packet leaving the PES (Fig. 3) on the top/bottom corresponds to the right/left deprotonation. Its amount is quantified by summing up all parts during the propagation

Mechanism of the CEP control. The neutral molecule experiences the part of the light field from time t_0 to t_1 (see Fig. 5a). The population of, for example, the

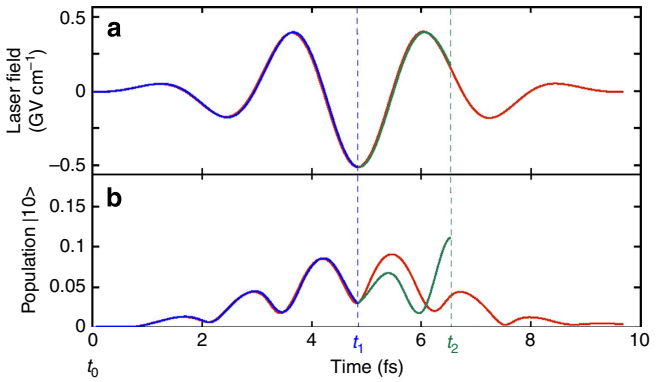

Figure 5 | Laser-field control of asymmetric hydrogen bond breaking. (**a**) Electric field waveform of the near-single-cycle laser pulse used in the calculations (red line). The parts of the field that act on the neutral and cation are displayed as blue and green lines, respectively. (**b**) Population of the IR-active mode |10>. The population induced in the neutral molecule is shown as blue line. At the peak of the laser field (t_1), the |10> population is transferred to the cation and its evolution is shown as the green line. Recollisional excitation, 1.7 fs (t_2) later, transfers the population to the $A^3\Pi_u$ state of the dication, from where dissociation can occur. Now the eigenfunctions constituting the vibrational wave packet are continuum wavefunctions. Without ionization, interaction with the entire field would induce only a transient population shown as red line, which vanishes with the end of the laser pulse.

© 2014 Macmillan Publishers Limited. All rights reserved.

anti-symmetric mode $|10>$ (Fig. 5b) follows the electric field of the few-cycle pulse. The CEP of the few-cycle pulse imprints a certain phase (φ_{CEP}) on the eigenfunction of $|10>(|10>e^{-i\varphi_{CEP}t})$, which leads through superposition with the $|01>$ mode (populated in the ionization) to the directional deprotonation. Ionization is assumed to happen at maximal field strength (see blue line at t_1 in Fig. 5b). From the evolution of the $|10>$ population, it becomes obvious that the ionization step is crucial to populate the $|10>$ mode as the interaction with the complete non-resonant light field would induce neither population (shown in red) nor phase information transfer. The first ionization transfers the vibrational wave packet to the cation. The major part of the wave packet is still the $|00>$ component with no directional preference. However, because of the slight difference in the shape of the neutral and cationic potential energy curves now also the IR inactive mode $|01>$ is slightly populated with a system dependent, but uncontrollable phase $e^{-i\frac{E_{01}}{\hbar}t}$. The population of the IR-active mode $|10>$ is further increased by the interactions with the remaining light field (Fig. 5b, green line) and the imprinted phase in the superposition, defining the direction of the wave packet oscillation, is strengthened. The cation experiences the part of the light field from time t_1 to t_2 (Fig. 5a). Contributions from higher vibrational quantum numbers may occur, but play a minor role. The prepared wave packet retains the memory of direction, when transferred to the dication in the final step.

References

1. Zewail, A. H. Laser femtochemistry. *Science* **242,** 1645–1653 (1988).
2. Brixner, T. & Gerber, G. Quantum control of gas-phase and liquid-phase femtochemistry. *ChemPhysChem.* **4,** 418–438 (2003).
3. Brif, C., Chakrabarti, R. & Rabitz, H. Control of quantum phenomena: past, present and future. *New J. Phys.* **12,** 075008 (2010).
4. Judson, R. S. & Rabitz, H. Teaching lasers to control molecules. *Phys. Rev. Lett.* **68,** 1500–1503 (1992).
5. Assion, A. *et al.* Control of chemical reactions by feedback-optimized phase-shaped femtosecond laser pulses. *Science* **282,** 919–922 (1998).
6. Daniel, C. *et al.* Deciphering the reaction dynamics underlying optimal control laser fields. *Science* **299,** 536–539 (2003).
7. Alnaser, A. S. *et al.* Momentum-imaging investigations of the dissociation of D_2^+ and the isomerization of acetylene to vinylidene by intense short laser pulses. *J. Phys. B* **39,** S485–S492 (2006).
8. Hoshina, K., Furukawa, Y., Okino, T. & Yamanouchi, K. Efficient ejection of H_3^+ from hydrocarbon molecules induced by ultrashort intense laser fields. *J. Chem. Phys.* **129,** 104302 (2008).
9. Itakura, R. *et al.* Two-body Coulomb explosion and hydrogen migration in methanol induced by intense 7 and 21fs laser pulses. *J. Chem. Phys.* **127,** 104306 (2007).
10. Xu, H., Okino, T., Nakai, K. & Yamanouchi, K. Ultrafast hydrogen migration in hydrocarbon molecules driven by intense laser fields. in *Progress in Ultrafast Intense Laser Science VII* 35–52 (Springer, 2011).
11. Markevitch, A. N., Romanov, D. A., Smith, S. M. & Levis, R. J. Coulomb explosion of large polyatomic molecules assisted by nonadiabatic charge localization. *Phys. Rev. Lett.* **92,** 063001 (2004).
12. Roither, S. *et al.* High energy proton ejection from hydrocarbon molecules driven by highly efficient field ionization. *Phys. Rev. Lett.* **106,** 163001 (2011).
13. Xie, X. *et al.* Attosecond-recollision-controlled selective fragmentation of polyatomic molecules. *Phys. Rev. Lett.* **109,** 243001 (2012).
14. Okino, T., Watanabe, A., Xu, H. & Yamanouchi, K. Ultrafast hydrogen scrambling in methylacetylene and methyl-d_3-acetylene ions induced by intense laser fields. *Phys. Chem. Chem. Phys.* **14,** 10640–10646 (2012).
15. Baltuška, A. *et al.* Attosecond control of electronic processes by intense light fields. *Nature* **421,** 611–615 (2003).
16. Kling, M. F., von den Hoff, P., Znakovskaya, I. & de Vivie-Riedle, R. (Sub-) femtosecond control of molecular reactions via tailoring the electric field of light. *Phys. Chem. Chem. Phys.* **15,** 9448–9467 (2013).
17. Kremer, M. *et al.* Electron localization in molecular fragmentation of H_2 by carrier-envelope phase stabilized laser pulses. *Phys. Rev. Lett.* **103,** 213003 (2009).
18. Betsch, K. J. *et al.* Controlled directional ion emission from several fragmentation channels of CO driven by a few-cycle laser field. *Phys. Rev. A* **86,** 063403 (2012).
19. Xu, H. *et al.* Carrier-envelope-phase-dependent dissociation of hydrogen. *New J. Phys.* **15,** 023034 (2013).
20. Sansone, G. *et al.* Electron localization following attosecond molecular photoionization. *Nature* **465,** 763–766 (2010).
21. Siu, W. *et al.* Attosecond control of dissociative ionization of O_2 molecules. *Phys. Rev. A* **84,** 063412 (2011).
22. Tesch, C. M. & de Vivie-Riedle, R. Quantum computation with vibrationally excited molecules. *Phys. Rev. Lett.* **89,** 157901 (2002).
23. de Vivie-Riedle, R. & Troppmann, U. Femtosecond lasers for quantum information technology. *Chem. Rev.* **107,** 5082–5100 (2007).
24. Johnson, N. G. *et al.* Single-shot carrier-envelope-phase-tagged ion-momentum imaging of nonsequential double ionization of argon in intense 4-fs laser fields. *Phys. Rev. A* **83,** 013412 (2011).
25. Bergues, B. *et al.* Attosecond tracing of correlated electron-emission in non-sequential double ionization. *Nat. Commun.* **3,** 813 (2012).
26. Kübel, M. *et al.* Non-sequential double ionization of N_2 in a near-single-cycle laser pulse. *Phys. Rev. A* **88,** 023418 (2013).
27. Tannor, D. J., Kosloff, R. & Rice, S. A. Coherent pulse sequence induced control of selectivity of reactions: exact quantum mechanical calculations. *J. Chem. Phys.* **85,** 5805 (1986).
28. Lein, M. Molecular imaging using recollision electrons. *J. Phys. B* **40,** R135–R173 (2007).
29. Anis, F. & Esry, B. D. Enhancing the intense field control of molecular fragmentation. *Phys. Rev. Lett.* **109,** 133001 (2012).
30. Lan, P., Takahashi, E. J., Liu, K., Fu, Y. & Midorikawa, K. Carrier envelope phase dependence of electron localization in the multicycle regime. *New J. Phys.* **15,** 063023 (2013).
31. Cerullo, G., Baltuška, A., Mücke, O. D. & Vozzi, C. Few-optical-cycle light pulses with passive carrier-envelope phase stabilization. *Laser & Photon. Rev.* **5,** 323–351 (2011).
32. Wittmann, T. *et al.* Single-shot carrier-envelope phase measurement of few-cycle laser pulses. *Nat. Phys.* **5,** 357–362 (2009).
33. Rathje, T. *et al.* Review of attosecond resolved measurement and control via carrier-envelope phase tagging with above-threshold ionization. *J. Phys. B* **45,** 074003 (2012).
34. Kübel, M. *et al.* Carrier-envelope-phase tagging in measurements with long acquisition times. *New J. Phys.* **14,** 093027 (2012).
35. Werner, H. J. *et al. Molpro, Version 2006.1, a Package of Ab-Initio Programs* (2006).

Acknowledgements

We are grateful for support by the DFG via the grant Kl-1439/3 and the Cluster of Excellence: Munich Center for Advanced Photonics (MAP). A.S.A. acknowledges support from the American University of Sharjah. N.G.K., I.B. and M.F.K. were partially supported by the Chemical Sciences, Geosciences, and Biosciences Division, Office of Basic Energy Sciences, Office of Science, U.S. Department of Energy under DE-FG02-86ER13491 and the NSF under CHE-0822646. We are also grateful for support from the King-Saud University in the framework of the MPQ-KSU-LMU collaboration and the visiting professorship program.

Author contributions

A.S.A. and M.F.K. conceived the experiment. A.S.A., M.K., N.G.K., K.J.B. and Y.D. carried out the measurements; the data analysis and interpretation were done by A.S.A., M.K., B.B, N.G.K., K.J.B., R.S., R.d.V.-R. and M.F.K.; R.S. and R.d.V.-R. performed the calculations; part of the REMI was provided by and used in cooperation with R.M. and J.U.; the 10-kHz laser system was provided by and used in cooperation with J.S. and U.K.; Z.A.A., A.M.A., I.B. and F.K. contributed to the discussion of the results; the manuscript was prepared by A.S.A., M.K., R.S., B.B., F.K., R.d.V.-R. and M.F.K, and was discussed among all authors.

Additional information

Competing financial interests: The authors declare no competing financial interests.

Reprints and permission information is available online at http://npg.nature.com/reprintsandpermissions/

How to cite this article: Alnaser, A. S. *et al.* Subfemtosecond steering of hydrocarbon deprotonation through superposition of vibrational modes. *Nat. Commun.* 5:3800 doi: 10.1038/ncomms4800 (2014).

© 2014 Macmillan Publishers Limited. All rights reserved.

4.3 CEP control of bond rearrangement

The CEP control scheme of the nuclear wave packet introduced in the previous section 4.2 is not specific for the asymmetric dissociation of H atoms in acetylene, it is a universal method instead, that can be applied to different reactions and molecules. The following examples include the C-H bond breaking and bond rearrangement in acetylene and the bigger molecule allene (C_3H_4). While the explanation of the control with the superposition in the nuclear wave packet remains the same, the isomerization in acetylene and allene have additional points to consider. In acetylene the wave packet is formed with the *cis*- and *trans*-bending modes, while the final isomerization is described in reactive coordinates. For the degrees of freedom in the bigger allene molecule three normal modes are needed for the initial wave packet to form, so the superposition is $|00m\rangle + e^{-i\phi}(|0n_20\rangle + |n_100\rangle)$ instead of $|0m\rangle + e^{-i\phi}|n0\rangle$. Figure 4.3 shows the normal modes for the deprotonation of acetylene and for the hydrogen migration reaction in acetylene and allene and the reactive coordinates that are used for the isomerization in the upper part (a), (b) and (c). The lower part (d), (e) and (f) shows the Potential Energy Surface (PES) for the reaction in the dication in their respective coordinates.

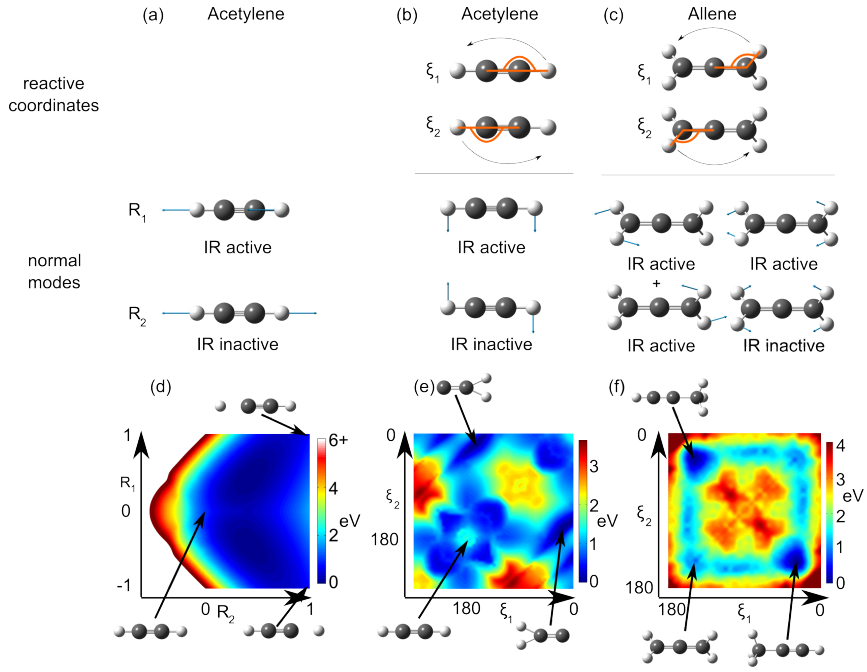

Figure 4.3: Reactive coordinates and normal modes used in the theoretical description of the deprotonation of acetylene and the hydrogen migration reactions in acetylene and allene. The wave packet formation for the deprotonation in acetylene and for the hydrogen migration in acetylene and allene is calculated on two- or three-dimensional potential energy surfaces (PES) along the normal modes shown in panel (a), (b) and (c). The reactive coordinates (ξ_1, ξ_2) represent the CCH bond angles (shown in orange) and are used to describe the wave packet propagation leading to isomerization by hydrogen migration from the left to the right or from the right to the left. For the deprotonation only the normal modes are used as reaction coordinates. The PES of the $A^3\Pi$ state of the acetylene dication is shown in (d) and (e), on which deprotonation and isomerization occurs. The PES is plotted as a function of the two normal modes or reactive coordinates, respectively. The initial form of the molecule the two deprotonated and the two isomerized configurations are indicated. The $B^3\Pi$ state PES of the allene dication that is relevant for the isomerization reaction which leads to H_3^+ formation is shown in (f).

On the next pages the article "Steering Proton Migration in Hydrocarbons Using Intense Few-Cycle Laser Fields" published in *Physical Review Letters* is reprinted with permission from *Phys. Rev. Lett.* **116**, 193001 (2016).

PRL 116, 193001 (2016) PHYSICAL REVIEW LETTERS week ending 13 MAY 2016

Steering Proton Migration in Hydrocarbons Using Intense Few-Cycle Laser Fields

M. Kübel,[1,*] R. Siemering,[2] C. Burger,[1] Nora G. Kling,[1,3] H. Li,[1,4] A. S. Alnaser,[4,5] B. Bergues,[4] S. Zherebtsov,[1,4] A. M. Azzeer,[6] I. Ben-Itzhak,[3] R. Moshammer,[7] R. de Vivie-Riedle,[2,†] and M. F. Kling[1,4,‡]

[1]*Department of Physics, Ludwig-Maximilians-Universität Munich, D-85748 Garching, Germany*
[2]*Department of Chemistry and Biochemistry, Ludwig-Maximilians-Universität Munich, D-81377 München, Germany*
[3]*J.R. Macdonald Laboratory, Physics Department, Kansas-State University, Manhattan, Kansas 66506, USA*
[4]*Max Planck Institute of Quantum Optics, D-85748 Garching, Germany*
[5]*Physics Department, American University of Sharjah, P.O. Box 26666, Sharjah, United Arab Emirates*
[6]*Department of Physics & Astronomy, King-Saud University, Riyadh 11451, Saudi Arabia*
[7]*Max Planck Institute of Nuclear Physics, D-69117 Heidelberg, Germany*

(Received 17 August 2015; published 12 May 2016)

Proton migration is a ubiquitous process in chemical reactions related to biology, combustion, and catalysis. Thus, the ability to manipulate the movement of nuclei with tailored light within a hydrocarbon molecule holds promise for far-reaching applications. Here, we demonstrate the steering of hydrogen migration in simple hydrocarbons, namely, acetylene and allene, using waveform-controlled, few-cycle laser pulses. The rearrangement dynamics is monitored using coincident 3D momentum imaging spectroscopy and described with a widely applicable quantum-dynamical model. Our observations reveal that the underlying control mechanism is due to the manipulation of the phases in a vibrational wave packet by the intense off-resonant laser field.

DOI: 10.1103/PhysRevLett.116.193001

The rearrangement of hydrocarbon bonds via the migration of a hydrogen atom can result in major deformations of molecular architecture and, thus, alter the molecule's chemical properties. Examples include keto-enol tautomerism where the migration of a proton changes an aldehyde into an alcohol. Isomerization reactions of that kind have been the subject of numerous studies [1,2]. Of particular interest was to determine the so-called isomerization time, which has been measured to be within several tens of fs in small hydrocarbons [3–6]. The phenomenon has also been observed in larger molecules, such as protonated triglycine [7]. Tracing of the hydrogen migration from different locations within the molecule has been made possible via isotope labeling; see, e.g., Refs. [8–10]. The ability to exert control over the migration could lead to advancement in topics such as the efficiency of catalytic reactions [11] and combustion reactions regarding fuel and energy research [12]. Furthermore, light-induced control of hydrogen migration may open new reaction pathways which cannot materialize by other means.

Despite its direct relevance to applied chemistry, studies regarding the control of the hydrogen migration process have been scarce and have been limited to theory [13,14] for a long time. However, recent progress has been made in coherently controlling isomerization reactions using fundamental parameters of ultrafast strong-field laser sources. Xie *et al.* varied the pulse duration and intensity to explore the isomerization of ethylene [15] and reported control of the total fragmentation yields of various hydrocarbons [16].

Here, we demonstrate steering of the direction of the hydrogen migration using the electric field waveform of intense few-cycle laser pulses. This approach goes beyond earlier work on toluene [17] and methanol [18] using two-color pulses with a duration of tens of fs. In contrast, the duration of our few-cycle laser pulses is significantly shorter than the time scale of the isomerization dynamics, therefore, avoiding charge-resonance-enhanced ionization [19] occurring at large internuclear distances [20]. Moreover, an influence of electron localization-assisted enhanced ionization on the dissociation reactions, recently demonstrated for acetylene theoretically [21,22] and experimentally [23], is also avoided. In comparison to earlier experiments using longer pulses, our experiment, therefore, allows the study of the pure predetermination of a molecular reaction in the sense that the laser field initiates a reaction but is not present during the actual reaction.

The electric field of a few-cycle laser pulse can be described in the time domain as $E(t) = E_0(t)\cos(\omega t + \phi)$, where $E_0(t)$ is the envelope, ω the carrier frequency, and ϕ is the phase between the carrier and the envelope [carrier envelope phase (CEP)]. The CEP determines the electric field waveform on a subfemtosecond time scale and has proven to be a powerful parameter for controlling electron motion in various systems [20,24–26]. It has also recently been shown to apply to the control of nuclear wave packets [27].

In the present work, we show that the CEP of a few-cycle laser pulse further permits us to steer complex photochemical reactions involving structural rearrangements towards a desired outcome. This goes beyond steering the directional ion emission from a molecule undergoing a simple dissociation reaction, such as deprotonation [27,28]. Using a reaction microscope (REMI) [29], we observe asymmetric

 © 2016 American Physical Society

emission of carbon ions from acetylene and trihydrogen ions from allene as a function of the CEP of the driving laser pulses. The results are interpreted in terms of a quantum mechanical model where the direction of hydrogen migration results from the phases of a superposition of vibrational modes manipulated by the laser CEP.

The experimental setup will be described in detail elsewhere. Briefly, hydrogen migration in acetylene and allene is induced and controlled by intense, CEP-stable 4-fs laser pulses at a carrier wavelength of 750 nm and 10-kHz repetition rate. The near-single-cycle pulses are obtained from the SMILE laser system at the Ludwig-Maximilians-Universität (LMU), which is based on the Femtolasers Femtopower HR CEP4 amplified laser system. The CEP of the laser is stabilized using the feed-forward technique [30] and measured using either a stereo-ATI phase meter [31] (in the acetylene experiments) or an f-2f interferometer [32] (in the allene experiments).

In the REMI, the linearly polarized laser pulses are focused ($f = 17.5$ cm) into a cold gas jet of neutral hydrocarbon molecules. A homogeneous electric field is used to direct all ions generated in the laser focus onto a time- and position-sensitive multihit capable detector providing the three-dimensional momentum distributions of multiple ions in coincidence.

To study the strong-field steering of hydrogen-bond rearrangements in acetylene, we focus on its isomerization to vinylidene (CCH_2). This channel necessarily involves the migration of one of the protons from one side of the molecule to the other. Vinylidene formation is clearly identified by the dissociation of the dication into C^+ and CH_2^+ fragments that obey momentum conservation (neglecting the small momenta of the emitted electrons). The distinct separation between the fragments from the acetylene and vinylidene breakups, which have similar mass and momenta, is challenging and feasible so far only by coincidence detection methods [29,33].

Figure 1(a) shows the momentum along the laser propagation axis (p_x) versus the momentum along the laser polarization (p_z) for C^+ ions produced in the breakup of the vinylidene dication. The nearly isotropic momentum distribution of the C^+ ions can be understood as a consequence of the hydrogen migration preceding dissociation of vinylidene along the C—C bond [33]. For C^+ momenta in the indicated range -42 a.u. $< p_z < -28$ a.u., the C^+ ions arrive at the ion detector almost simultaneously with the coincident CH_2^+ fragments, which impedes their coincident detection. Hence, only events with momenta outside the range 28 a.u. $< |p_z| <$ 42 a.u. are considered for evaluating the CEP dependence of the C^+ emission direction. The emission direction of the C^+ ion following the cleavage of the C—C bond is directly indicative of whether the left proton in acetylene has migrated to the right side (along the laser polarization), or vice versa. The yields of C^+ ions emitted to the right $R(\phi)$ or left $L(\phi)$ as a function of the CEP are, therefore, a measure of the influence of the CEP on

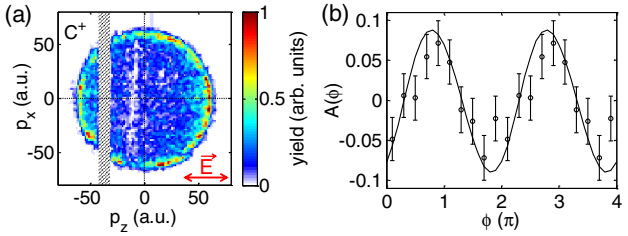

FIG. 1. Strong-field steering of hydrogen migration in acetylene. (a) Measured CEP-averaged momentum distribution for C^+ ions emitted from vinylidene dications following hydrogen migration in acetylene induced by 4-fs laser pulses with an intensity $I \approx 1.3 \times 10^{14}$ W/cm^2. The shaded area is cut out for technical reasons (see text). The red arrow indicates the axis of laser polarization. (b) CEP-dependent asymmetry parameter for the C^+ yield shown in (a), evaluated for a cone of 80° around the polarization axis of the laser. Since the absolute value of the CEP is not known from the experiment, the phase is given relative to the asymmetry parameter recorded for $C_2H_2^+$ recoil ions (see text). The solid line depicts the calculated asymmetry curve for an intensity of 1.5×10^{14} W/cm^2, shifted along the CEP axis for best agreement with the experiment.

the hydrogen migration. To quantify the CEP dependence, we introduce the asymmetry parameter as

$$A(\phi) = [L(\phi) - R(\phi)]/[L(\phi) + R(\phi)]. \quad (1)$$

The CEP dependence of the asymmetry parameter $A_{C^+}(\phi)$ recorded for C^+ ions and plotted in Fig. 1(b) demonstrates the steering of the direction of proton migration in acetylene.

For allene ($H_2C_3H_2$) molecules, the hydrogen motion is monitored through the formation of trihydrogen ions (H_3^+). This reaction channel is identified by the dissociation of the allene dication into H_3^+ and C_3H^+ fragments. Even though allene's isomer propyne (HC_3H_3) is stable in the neutral state and contained in low concentrations in commercially available allene gas bottles, H_3^+ formation has been found to result predominantly from the isomerization of allene [8].

The results for the H_3^+ formation from allene are displayed in Fig. 2. The momentum distribution recorded for H_3^+ [Fig. 2(a)] is nearly isotropic, which is consistent with the findings of Refs. [4,8]. The CEP dependence of the asymmetry parameter $A_{H_3^+}(\phi)$ demonstrates the steering of the direction of proton migration in allene. Interestingly, we find in our experiments that the asymmetry in the H_3^+ formation from allene exhibits a pronounced sensitivity to the laser intensity [34].

The CEP axes in Figs. 1(b) and 2(b) are given relative to the phase of the asymmetry parameters [see Eq. (1)] measured for the recoil cations of either molecule produced by single ionization. This makes a comparison of the phases of the asymmetry parameters recorded for hydrogen migration in acetylene and allene possible, indicating that $A_{C^+}(\phi)$ and $A_{H_3^+}(\phi)$ assume maxima for similar but not identical CEP values. The experimental data are further compared to predictions from our quantum mechanical calculations.

PRL 116, 193001 (2016) PHYSICAL REVIEW LETTERS week ending 13 MAY 2016

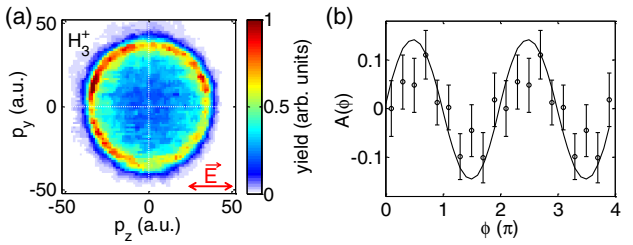

FIG. 2. Strong-field steering of hydrogen migration in allene. (a) CEP-averaged momentum distribution and (b) CEP-dependent asymmetry parameter for H_3^+ ions emitted from propyne dications following hydrogen migration in allene. The red arrow in (a) indicates the axis of laser polarization. The CEP dependence of the H_3^+ emission is evaluated for a cone of 80° around the polarization axis of the laser and at a peak intensity of $\approx 2.9 \times 10^{14}$ W/cm^2. The phase is given relative to the asymmetry parameter recorded for $C_3H_4^+$ recoil ions (see text). The measured asymmetry curve (symbols) is compared to the one calculated (solid line) for an intensity of 3.0×10^{14} W/cm^2, shifted along the CEP axis by the same value as the theory curve in Fig. 1(b).

Because the absolute CEP in the experiment is not known, the predicted curve for C^+ emission from acetylene was shifted along the CEP for best agreement with the experiment. The prediction for H_3^+ emission from allene was shifted by the same amount and lines up with the measured asymmetry. Moreover, the amplitudes of the calculated asymmetries agree reasonably well with the measured ones, lending support to the model described in the following.

In general, any nuclear motion can be expressed in the basis of all normal modes. We use normal modes to describe the molecule laser interaction and reactive coordinates for the description of the subsequent hydrogen migration. The subsets of normal modes relevant for the initiation of the reactions are illustrated in Fig. 3. For acetylene [Fig. 3(a)], the IR-active cis-bending mode $|n0\rangle$ and the IR-inactive trans-bending mode $|0m\rangle$ form a 2D basis $|nm\rangle$, where m, n are the number of vibrational quanta. Here, the respective time evolution factor $\exp[-i(E_{m/n}/\hbar)t]$ is implicitly included, and the relative phase of the eigenfunctions is set to compensate any phase offset relative to the CEP. For allene [Fig. 3(b)], three normal modes (IR-active rocking and antisymmetric bending and IR-inactive symmetric bending) are required to describe the initiation of isomerization by the laser field.

The interaction of the molecules with the external laser field is calculated by solving the time-dependent Schrödinger equation (TDSE) using the Chebychev propagator. The TDSE for the neutral molecule under the influence of the light field reads

$$[H_n + \mu_{nn}\epsilon(t)]\Psi_n(t) = i\hbar\frac{d}{dt}\Psi_n(t), \qquad (2)$$

where H_n is the Hamiltonian of $X^1\Sigma_g^+$, μ_{nn} is the associated dipole moment, and $\Psi_n(t)$ is the nuclear wave function.

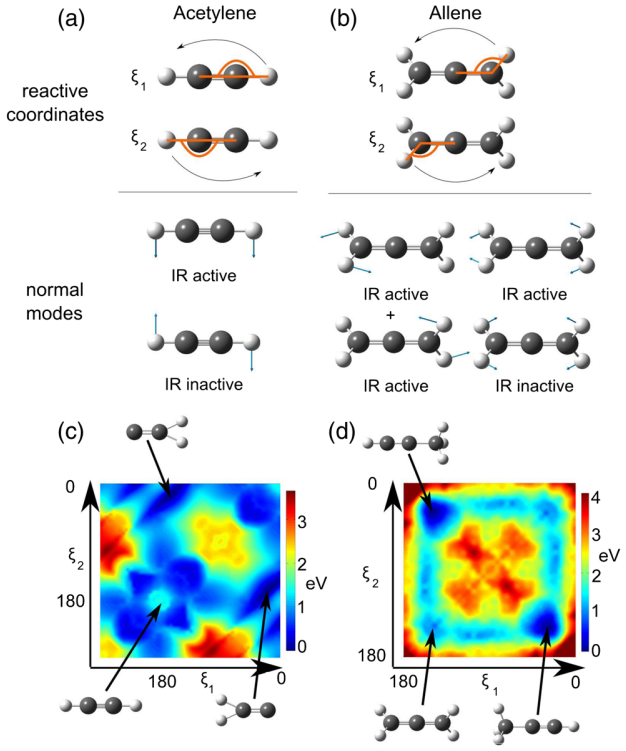

FIG. 3. Reactive coordinates and normal modes used in the theoretical description of the hydrogen migration reactions in acetylene and allene. The wave packet formation in acetylene (allene) is calculated on two- (three-) dimensional potential energy surfaces (PES) along the normal modes shown in panel (a) [(b)]. The reactive coordinates (ξ_1, ξ_2) represent the CCH bond angles (shown in orange) and are used to describe the wave packet propagation leading to isomerization by hydrogen migration from the left to the right or from the right to the left. (c) The PES of the $A^3\Pi$ state of the acetylene dication, on which isomerization occurs. The binding energy is plotted as a function of the two reactive coordinates. The initial form of the molecule and the two isomerized configurations are indicated. (d) Same as (c) for the $B^3\Pi$ state of the allene dication relevant for the isomerization reaction which leads to H_3^+ formation.

The light field $\epsilon(t)$ is included in the dipole approximation and is characterized by a full width at half maximum of the intensity envelope of 4 fs.

The excitation and ionization mechanism is explained exemplarily for acetylene. The laser only addresses the IR-active modes $|n0\rangle$, in which it creates a wave packet $e^{-i\phi}|n0\rangle$. This wave packet forms temporarily even if the laser pulse is nonresonant to the vibration, and the phase ϕ of the vibrational wave packet matches the laser CEP. For our simulations, we consider that the molecule is ionized at the peak intensity of the laser pulse. This approximation leads to a slight overestimation of the asymmetry amplitude, which is consistent with Figs. 1(b) and 2(b). Without the ionization, the molecule would remain in the vibrational ground state after the laser pulse has passed.

As the eigenfunctions of the molecular cation are slightly different from the ones of the neutral molecule, the

ionization leads to population of several cationic modes, including the IR-inactive ones $|0m\rangle$. This population process by ionization is independent of the CEP. The CEP-dependent part of the full wave packet is, therefore, predominantly given by the basic superposition of the fundamental IR-active and the IR-inactive modes,

$$\Psi_{\text{basic}} = |01\rangle + e^{-i\phi}|10\rangle. \quad (3)$$

For interpretation of the control mechanism, it is sufficient to concentrate on Ψ_{basic} because it is responsible for the asymmetric isomerization occurring in the dication. The dication is populated 3/4 of an optical cycle after the first ionization, which allows enough time for electron recollision [35]. The (full) wave packet is projected onto the reactive, excited dicationic state, which is the lowest excited state we find to support isomerization.

In the second simulation step, the isomerization dynamics in the reactive state is described on two-dimensional PES along two reactive coordinates illustrated in Fig. 3. These coordinates describe the CCH bond angles leading to isomerization. To calculate the isomerization, we project the wave packet Ψ_{modes} expressed in normal modes onto the wave packet ψ_{reac} expressed in reactive coordinates. The projection is performed via the respective eigenfunctions of the dication ground state

$$\psi_{\text{reac}} = \sum_{i,j} \langle \Psi_{\text{modes}}|\Phi_i\rangle\langle\Phi_i|\phi_j\rangle|\phi_j\rangle, \quad (4)$$

where Φ_i are the normal mode eigenfunctions, and ϕ_j are the reactive coordinate eigenfunctions.

The isomerization is simulated through evolution of the prepared wave packet on the reactive states for 480 fs with time intervals of 0.24 fs. The reactive states are the $A^3\Pi$ state of the acetylene dication [Fig. 3(c)] and the $B^3\Pi$ state of the allene dication [Fig. 3(d)]. On both reactive states, the Franck-Condon region is not the global minimum. Isomerization occurs if small barriers in the PES are overcome by the kinetic energy of the generated wave packets and the isomerization minima indicated in Figs 3(c) and 3(d) are reached. From these isomerization minima, dissociation can take place. The dissociation yield L (R) corresponding to the left (right) isomerization is quantified by the part of the wave packet at the corresponding isomerization minimum after integration over the propagation time. The asymmetry parameter A is calculated from L and R according to Eq. (1).

For the isomerization of acetylene to vinylidene, the control mechanism is illustrated by the calculated wave packet propagation displayed in Fig. 4. The wave packet that is prepared in the neutral and cation is projected onto the reactive $A^3\Pi$ state in the dication and propagated along the two reactive coordinates introduced above. The wave packet possesses a CEP-dependent preferential propagation direction contained in the basic wave packet Ψ_{basic}. The propagation direction results in population of either one of

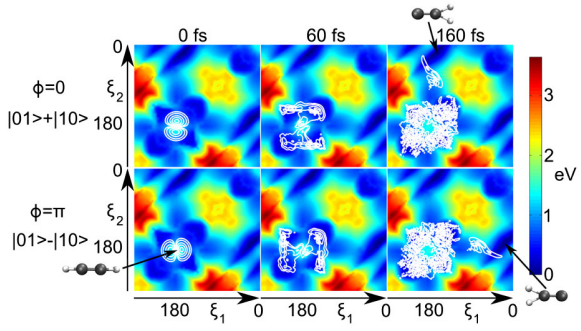

FIG. 4. Schematic of the control mechanism for hydrogen migration in acetylene. Vibrational wave packets of the $\Psi_{\text{basic}}(0) = |01\rangle + |10\rangle$ (top row) and the $\Psi_{\text{basic}}(\pi) = |01\rangle - |10\rangle$ (bottom row) superposition (see text) are propagated on the PES of the first excited state of the acetylene dication along two reactive coordinates. The contour lines display snapshots of the calculated nuclear wave packet which leads to isomerization of the acetylene dication. The CEP of the few-cycle pulse determines the sign in the superposition and thereby influences whether the left proton moves to the right (top row) or the right proton to the left (bottom row).

the two indicated potential minima corresponding to the left or the right vinylidene configurations. This leads to the experimentally observed bias in the C^+ emission direction after dissociation of the C—C bond, tunable with the CEP.

The isomerization of allene to propyne occurs on the PES plotted in Fig. 3(d) in a similar manner as the isomerization of acetylene but is more complex. The reactive coordinates for the allene isomerization are a linear combination of eight normal modes. Three of these modes [one IR-inactive, two IR-active ones; see Fig. 3(b)] are populated in the preparation step, giving rise to a CEP-dependent wave packet $\Psi = |00m\rangle + e^{-i\phi}(|n_1 00\rangle + |0n_2 0\rangle)$, which allows for steering of the direction of hydrogen migration. We believe that the proposed model can be extended to dynamics in even larger molecules—including rearrangements of functional groups, such as the keto-enol tautomerization—as long as the proper reaction coordinates can be identified.

In conclusion, we have demonstrated experimentally that few-cycle laser pulses can be exploited to steer the preferential direction of hydrogen migration in small hydrocarbon molecules. The hydrogen migration processes leading to the isomerization of acetylene to vinylidene and to H_3^+ formation in allene can be understood in terms of a nuclear control mechanism similar to the one proposed in Ref. [27]. According to this mechanism, a field-sensitive nuclear wave packet is prepared during the few-fs interaction of the molecules with the laser field which predetermines the outcome of an isomerization reaction taking place on a significantly longer time scale. The efficiency of the control could be improved by resonant excitation of the vibrational modes and driving ionization by even shorter laser pulses. Our work has implications on the strong-field coherent control of more complex photochemical

reactions, which may lead to alteration of the structural and functional properties of hydrocarbon molecules.

We are grateful to F. Krausz for his support and fruitful discussions. We acknowledge A. Kessel and S. A. Trushin for experimental support. We are grateful for support by the EU through the ERC Grant ATTOCO (No. 300372), by the Max Planck Society, and by the DFG via LMUexcellent and the cluster of excellence Munich Centre for Advanced Photonics (MAP). This project has received funding from the European Union's Horizon 2020 research and innovation programme under the Marie Sklodowska-Curie Grant Agreement No. 657544. A. S. A. acknowledges support from the American University of Sharjah and the Arab Fund for Economic and Social Development (State of Kuwait). I. B. I. was supported by the Chemical Sciences, Geosciences, and Biosciences Division, Office of Basic Energy Sciences, Office of Science, U.S. Department of Energy. We are also grateful for support from the King-Saud University in the framework of the MPQ-KSU-LMU Collaboration.

*Matthias.kuebel@physik.uni-muenchen.de
†Regina.de_Vivie@cup.uni-muenchen.de
‡matthias.kling@lmu.de

[1] B. G. Levine and T. J. Martínez, Annu. Rev. Phys. Chem. **58**, 613 (2007).
[2] H. M. D. Bandara and S. C. Burdette, Chem. Soc. Rev. **41**, 1809 (2012).
[3] T. Osipov, C. L. Cocke, M. H. Prior, A. Landers, T. Weber, O. Jagutzki, L. Schmidt, H. Schmidt-Böcking, and R. Dörner, Phys. Rev. Lett. **90**, 233002 (2003).
[4] H. Xu, T. Okino, and K. Yamanouchi, Chem. Phys. Lett. **469**, 255 (2009).
[5] Y. H. Jiang, A. Rudenko, O. Herrwerth, L. Foucar, M. Kurka, K. U. Kühnel, M. Lezius, M. F. Kling, J. van Tilborg, A. Belkacem, K. Ueda, S. Düsterer, R. Treusch, C. D. Schröter, R. Moshammer, and J. Ullrich, Phys. Rev. Lett. **105**, 263002 (2010).
[6] H. Ibrahim, B. Wales, S. Beaulieu, B. E. Schmidt, N. Thiré, E. P. Fowe, E. Bisson, C. T. Hebeisen, V. Wanie, M. Giguére, J.-C. Kieffer, M. Spanner, A. D. Bandrauk, J. Sanderson, M. S. Schuurman, and F. Légaré, Nat. Commun. **5**, 4422 (2014).
[7] C. F. Rodriquez, A. Cunje, T. Shoeib, I. K. Chu, A. C. Hopkinson, and K. W. M. Siu, J. Am. Chem. Soc. **123**, 3006 (2001).
[8] T. Okino, A. Watanabe, H. Xu, and K. Yamanouchi, Springer Proc. Phys. **125**, 335 (2012).
[9] T. Okino, A. Watanabe, H. Xu, and K. Yamanouchi, Phys. Chem. Chem. Phys. **14**, 10640 (2012).
[10] B. R. Heazlewood, A. T. Maccarone, D. U. Andrews, D. L. Osborn, L. B. Harding, S. J. Klippenstein, M. J. T. Jordan, and S. H. Kable, Nat. Chem. **3**, 443 (2011).
[11] C. Naccache, The chemistry of catalytic hydrocarbon conversions, in *Applied Catalysis* (Academic Press, New York, 1982), Vol. 3, pp. 199–200.
[12] *Acyclic Hydrocarbons—Advances in Research and Application: 2012 Edition*, edited by Q. Ashton Acton (Scholarly Editions, Atlanta, Georgia, 2012), p. 272.
[13] C. Uiberacker and J. Werner, J. Chem. Phys. **120**, 11540 (2004).
[14] M. E. A. Madjet, Z. Li, and O. Vendrell, J. Chem. Phys. **138**, 094311 (2013).
[15] X. Xie, S. Roither, M. Schöffler, E. Lötstedt, D. Kartashov, L. Zhang, G. G. Paulus, A. Iwasaki, A. Baltuška, K. Yamanouchi, and M. Kitzler, Phys. Rev. X **4**, 021005 (2014).
[16] X. Xie, K. Doblhoff-Dier, S. Roither, M. S. Schöffler, D. Kartashov, H. Xu, T. Rathje, G. G. Paulus, A. Baltuška, S. Gräfe, and M. Kitzler, Phys. Rev. Lett. **109**, 243001 (2012).
[17] S. Kaziannis, N. Kotsina, and C. Kosmidis, J. Chem. Phys. **141**, 104319 (2014).
[18] N. Kotsina, S. Kaziannis, and C. Kosmidis, Int. J. Mass Spectrom. **380**, 34 (2015).
[19] T. Zuo and A. D. Bandrauk, Phys. Rev. A **52**, R2511 (1995).
[20] M. F. Kling, C. Siedschlag, A. J. Verhoef, J. I. Khan, M. Schultze, T. Uphues, Y. Ni, M. Uiberacker, M. Drescher, F. Krausz, and M. J. J. Vrakking, Science **312**, 246 (2006).
[21] E. Lötstedt, T. Kato, and K. Yamanouchi, Phys. Rev. A **85**, 041402 (2012).
[22] E. Lötstedt, T. Kato, and K. Yamanouchi, J. Chem. Phys. **138**, 104304 (2013).
[23] X. Gong, Q. Song, Q. Ji, H. Pan, J. Ding, J. Wu, and H. Zeng, Phys. Rev. Lett. **112**, 243001 (2014).
[24] G. G. Paulus, F. Grasbon, H. Walther, P. Villoresi, M. Nisoli, S. Stagira, E. Priori, and S. De Silvestri, Nature (London) **414**, 182 (2001).
[25] A. Baltuska, T. Udem, M. Uiberacker, M. Hentschel, E. Goulielmakis, C. Gohle, R. Holzwarth, V. S. Yakovlev, A. Scrinzi, T. W. Hänsch, and F. Krausz, Nature (London) **421**, 611 (2003).
[26] A. Schiffrin, T. Paasch-Colberg, N. Karpowicz, V. Apalkov, D. Gerster, S. Mühlbrandt, M. Korbman, J. Reichert, M. Schultze, S. Holzner, J. V. Barth, R. Kienberger, R. Ernstorfer, V. S. Yakovlev, M. I. Stockman, and F. Krausz, Nature (London) **493**, 70 (2013).
[27] A. S. Alnaser, M. Kübel, R. Siemering, B. Bergues, N. G. Kling, K. J. Betsch, Y. Deng, J. Schmidt, Z. A. Alahmed, A. M. Azzeer, J. Ullrich, I. Ben-Itzhak, R. Moshammer, U. Kleineberg, F. Krausz, R. de Vivie-Riedle, and M. F. Kling, Nat. Commun. **5**, 3800 (2014).
[28] S. Miura, T. Ando, K. Ootaka, A. Iwasaki, H. Xu, T. Okino, K. Yamanouchi, D. Hoff, T. Rathje, G. G. Paulus, M. Kitzler, A. Baltuška, G. Sansone, and M. Nisoli, Chem. Phys. Lett. **595–596**, 61 (2014).
[29] J. Ullrich, R. Moshammer, A. Dorn, R. Dörner, L. P. H. Schmidt, and H. Schmidt-Böcking, Rep. Prog. Phys. **66**, 1463 (2003).
[30] F. Lücking, A. Assion, A. Apolonski, F. Krausz, and G. Steinmeyer, Opt. Lett. **37**, 2076 (2012).
[31] T. Rathje, N. G. Johnson, M. Möller, F. Süßmann, D. Adolph, M. Kübel, R. Kienberger, M. F. Kling, G. G. Paulus, and A. M. Sayler, J. Phys. B **45**, 074003 (2012).

[32] M. Schultze, A. Wirth, I. Grguras, M. Uiberacker, T. Uphues, A. J. Verhoef, J. Gagnon, M. Hofstetter, U. Kleineberg, E. Goulielmakis, and F. Krausz, J. Electron Spectrosc. Relat. Phenom. **184**, 68 (2011).

[33] A. S. Alnaser, I. Litvinyuk, T. Osipov, B. Ulrich, A. Landers, E. Wells, C. M. Maharjan, P. Ranitovic, I. Bochareva, D. Ray, and C. L. Cocke, J. Phys. B **39**, S485 (2006).

[34] M. Kübel *et al.* (to be published).

[35] H. Niikura, F. Légaré, R. Hasbani, A. D. Bandrauk, M. Y. Ivanov, D. M. Villeneuve, and P. B. Corkum, Nature (London) **417**, 917 (2002).

5 Control of electron dynamics

The timescales involved with ultra short laser pulses do not only allow the observation and control of nuclear dynamics, but also of electronic processes [103]. One scenario for the control of electron dynamic is the selective population of dressed states [104]. In this scenario a laser pulse creates a superposition between two electronic states, which will in turn generate an oscillating dipole moment. Now a second laser pulse with a relative phase shift of $\pm\pi$ to the first pulse can pick one dressed state to be populated. The intensity of the second pulse is much larger than the intensity of the first pulse and determines the splitting Ω between the dressed states. If the two dressed states have resonance to two different target states, the final population of these can be controlled with this mechanism. If the two target states have different reaction pathways this will ultimately also control the product of a chemical reaction with laser light.

This control scheme has been realized with the potassium atom [105, 106], were the photo electron energy can be influenced by the choice of the laser pulse. The more complex system of the potassium dimer behaves similarly [107, 108], but even with just one nuclear coordinate the coupling of the nuclear and electron dynamics influences the control of the electron dynamic.

To accurately describe these effects for the dressed state scenario a more sophisticated approach to the electronic wave function is needed, as it has to respond to the coupled electron and nuclear dynamics. To calculate an appropriate time dependent electronic wave function, that also allows to easily evaluate the electron density as a function of the time, the molecular wave function is, analog to the Born-Oppenheimer approximation, multiplied with the complex conjugated total nuclear wave function χ_{tot} from left and integrated over the nuclear coordinate R [70].

$$\varphi_{\text{tot}} = \int \chi_{\text{tot}}^{*} \Psi_{\text{mol}} \, \mathrm{d}R = \begin{pmatrix} \varphi_1 \\ \varphi_2 \\ \vdots \\ \varphi_n \end{pmatrix} \tag{5.1}$$

With this the new coupled electron wave function is

$$\varphi_i = a_i^2 \Phi_i + \sum_{j \neq i} \big\langle \chi_i(R) \big| \chi_j(R) \big\rangle \Phi_j \tag{5.2}$$

with $a_i = \sqrt{\big\langle \chi_i \big| \chi_i \big\rangle}_R$ the population of the ith electronic state and the overlap $\big\langle \chi_i(R) \big| \chi_j(R) \big\rangle_R$ of the nuclear wave function of the ith and jth state.

Because the time depended laser pulse determines the population of the electronic states in the nuclear dynamics in equation 2.22, the Hamiltonian of the electrons in the basis of the electronic eigenstates is diagonal [70].

With the help of the new stationary electronic wave function the electron density ρ_{tot} depending on the electronic coordinate and time can be obtained through integrating the square of the absolute value of the total wave function over the nuclear coordinates:

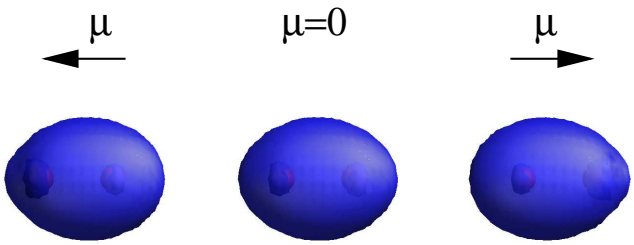

Figure 5.1: Distribution of the electron density within a 1.2 fs time frame (from the situation of the left to the right) of the superposition of the $X^1\Sigma_g^+$- and $A^1\Sigma_u^+$-state and the resulting induced dipole moment μ

$$\begin{aligned}\rho_{\text{tot}} = |\varphi_{\text{tot}}(r,t,\bar{R})|^2 &= \int \Psi^*_{\text{mol}}\Psi_{\text{mol}}\,\mathrm{d}R = (\Phi_1^*\Phi_2^*\cdots\Phi_n^*)\begin{pmatrix}\varphi_1\\ \varphi_2\\ \vdots\\ \varphi_n\end{pmatrix}\\ &= \sum_i a_i(t)|\Phi_i(r,t,\bar{R})|^2 + \sum_i\sum_{j>i} 2Re\{\langle\chi_i(R,t)|\chi_j(R,t)\rangle_R\Phi_i^*(r,t,\bar{R})\Phi_j(r,t,\bar{R})\}\\ &= \sum_i a_i(t)|\Phi_{i,0}(r,\bar{R})|^2 + \sum_i\sum_{j>i} 2Re\{\langle\chi_i(R,t)|\chi_j(R,t)\rangle_R\Phi_{i,0}^*(r,\bar{R})\Phi_{j,0}(r,\bar{R})e^{-i\Delta E_{i,j}(R(t))t}\}\end{aligned} \tag{5.3}$$

Quantumdynamical methods (see section 2.2) allow the numerical solving of equation 2.22. With this the populations $a_i(t)$, the overlap of the nuclear wave function $\langle\chi_i|\chi_j\rangle$ and the time dependent expectation value of the nuclear coordinate $R(t)$, can be evaluated. Quantumchemical calculations (see section 2.1) with the nuclear geometries $R(t) = \langle\chi_{\text{tot}}|R|\chi_{\text{tot}}\rangle$ allow to determine the shape of the orbitals $\Phi_{i,0}$. The oscillation period of the eigenfunction in the phase space is given by the time dependent eigenenergies $E_i(R(t))$, as the nuclear distance changes with time. So the phase of the electronic wave function has to be calculated recursively [70].

$$\theta_i(t) = \theta_i(t-\Delta' t)e^{-iE_i(t)\Delta' t} \tag{5.4}$$

Because the electronic phase changes faster than the nuclear motion, the time step $\Delta' t$ for the calculation of the electronic phase has to be shorter than the time step Δt of the propagation. Figure 5.1 shows a 1.2 fs time frame of a superposition of the $X^1\Sigma_g^+$ ground state and the first excited $A^1\Sigma_u^+$ state. The electron density changes drastically while the nuclei barely move at all.

The electronic excitation of the $X^1\Sigma_g^+$ ground state wave packet creates two nuclear wave packets, one in the ground state and one in the first excited state $A^1\Sigma_u^+$. This creates an oscillating dipole moment (see fig. 5.1 for a 1.2 fs time frame of the changing electron density and fig. 5.2 top panel blue for the time evolution of the oscillating dipole moment). The wave packet in the excited state moves away, because the binding potentials differ for the two involved states, which decreases the overlap between the two wave packets (fig. 5.2 2nd panel from top cyan), and therefore the oscillating dipole moment, that depends on the overlap. Without the oscillating dipole the second pulse can not create the dressed states. This leads to a timing window dictated by the nuclear dynamic, that would not come up if only considering the electron dynamic. The second effect of the nuclear wave packet movement is the change of the energy difference (fig. 5.2 bottom red) of the two electronic states depending on the nuclear coordinate (fig. 5.2 3rd panel from top magenta) and the correlated frequency of the oscillating dipole, which leads to a phase

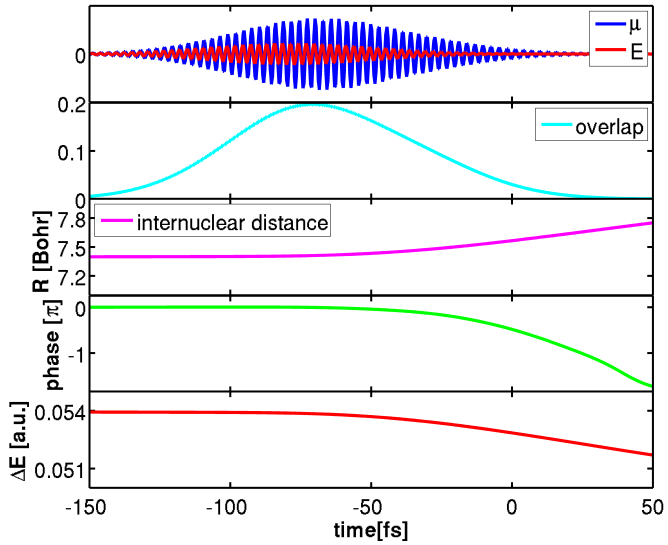

Figure 5.2: This figure illustrates the effect of nuclear wave packet motion on the oscillating dipole moment (top blue). The laser field (top red) excites the molecule forming a ground state wave packet and an excited state wave packet, that moves away. The overlap of these two wave packet is shown in cyan (2nd panel from top). As the excited wave packet moves away the average nuclear distance between the two atoms (magenta 3rd panel) increases. The 4th panel shows the phase difference (green) between the oscillating dipole moment (top blue) and the laser field (top red). The reason for the phase difference is that the increasing internuclear distance decreases the energy difference (bottom red) of the two states.

difference (fig. 5.2 4th panel from top green) between the exciting laser pulse (fig. 5.2 top red) and the oscillating dipole (fig. 5.2 top blue).

On the next pages the article "Charge oscillation controlled molecular excitation" published in *Physical Review Letters* is reprinted with permission from *Phys. Rev. Lett.* **110**, 123003 (2013).

PRL 110, 123003 (2013) PHYSICAL REVIEW LETTERS week ending 22 MARCH 2013

Charge Oscillation Controlled Molecular Excitation

Tim Bayer,[1] Hendrike Braun,[1] Cristian Sarpe,[1] Robert Siemering,[2] Philipp von den Hoff,[2] Regina de Vivie-Riedle,[2] Thomas Baumert,[1] and Matthias Wollenhaupt[1,*]

[1]*Institut für Physik und CINSaT, Universität Kassel, Heinrich-Plett-Strasse 40, 34132 Kassel, Germany*

[2]*Department Chemie, Ludwig-Maximilians-Universität München, Butenandt-Strasse 11, 81377 München, Germany*

(Received 12 December 2012; revised manuscript received 18 February 2013; published 22 March 2013)

The direct manipulation of charge oscillations has emerged as a new perspective in chemical reaction control. Here, we demonstrate, in a joint experimental and theoretical study, that the electron dynamics of a molecule is efficiently steered by controlling the interplay of a driving femtosecond laser pulse with the photoinduced charge oscillation. These oscillations have a typical Bohr period of around 1 fs for valence electrons; therefore, control has to be exerted on a shorter time scale. Specifically, we show how precision pulse shaping is used to manipulate the coupled electron and nuclear dynamics in order to address different bound electronic target states in a molecule. We present a strong-field coherent control mechanism which is understood in terms of a simple classical picture and at the same time verified by solving the time-dependent Schrödinger equation. This mechanism is universally applicable and opens a wide spectrum of applications in the reaction control of complex systems.

DOI: 10.1103/PhysRevLett.110.123003 PACS numbers: 32.80.Qk, 32.80.Rm, 42.50.Md

The ability to control the course and the outcome of chemical reactions using coherent light [1] has become realistic with the experimental accessibility of femtosecond laser pulses acting on the natural time scale of nuclear motion driving chemical reactions [2]. With the advent of sophisticated pulse shaping techniques [3,4], efficient control on these very processes became available [5]. New frontiers opened with the realization of attosecond pulses in the laboratory. The emerging field of attosecond science [6–9] provided the possibility to directly observe even faster electron dynamics. Because of the high photon energies, the excitation of outer shell electrons by attosecond laser fields suffers from low cross sections and is likely to cause direct ionization, hampering the implementation of valence bond chemistry control schemes. On the other hand, electronic transitions of outer shell electrons driven by pico- to femtosecond laser pulses benefit from large transition moments. This is a prerequisite for efficient population transfer and thus to achieve efficient product yields in reaction control. In addition, nonperturbative strong laser fields alter the potential energy surface (PES) via dynamic Stark shifts, exploring new routes to different target states inaccessible in the weak-field regime. Experimental demonstrations of nonresonant Stark control acting on the time scale of the intensity envelope of an ultrashort laser pulse [10] comprise the observation of non-Franck-Condon transitions in bound wave packet motion [11], population control in atoms by shaped laser pulses [12], control of bound vibrational levels [13], and control of the branching ratio in a dissociation reaction [14]. The resonant Stark effect, acting on the time scale of the electron dynamics, provides more efficient manipulation of the energy landscape and in particular enables Stark shifting of molecular states to higher as well as lower energies [15–18].

In this Letter, we present a resonant coherent control scheme based on shaped intense femtosecond laser pulses where the initial part of the laser pulse creates an oscillating charge distribution with maximum amplitude in a molecule. After evolution on coherently coupled PES, a later part of the laser pulse is timed with extreme precision [19] to adjust the phase of the field to the oscillating dipole. The scenario allows us to steer the coupled electron and nuclear motion of the molecule to selectively populate different target channels, each of which entails different subsequent nuclear dynamics. Theoretical studies on the selective population of a single target channel employing pulse sequences used the potassium dimer (K_2) as the molecular prototype system [20–22]. Here, we report on the first experimental implementation of this control mechanism on molecules. For a proof of principle study, we also use the K_2 molecule because this system can be studied experimentally and theoretically on an equally accurate level. Quantum dynamical studies confirmed that the selectivity of the switching process is caused by the induced electronic coherence. Figure 1(a) shows the scheme for the selective excitation of K_2 with near 800 nm laser pulses. The molecular system consists of the $X^1\Sigma_g^+$ ground state, a resonant intermediate state ($A^1\Sigma_u^+$), and a set of final target states for selective population. The insets display calculated three-dimensional electronic density distributions for the relevant molecular states. In addition, the electronic densities for the superposition states of the $X^1\Sigma_g^+$ and $A^1\Sigma_u^+$ and their resulting dipole moments are shown. For computational details, see the Supplemental Material [23]. Weak-field interaction (red arrows) excites the molecule from the vibronic ground state $X^1\Sigma_g^+$ to the $2^1\Pi_g$ state via the resonant state $A^1\Sigma_u^+$. Strong-field resonant interaction initially results in a charge oscillation in

 © 2013 American Physical Society

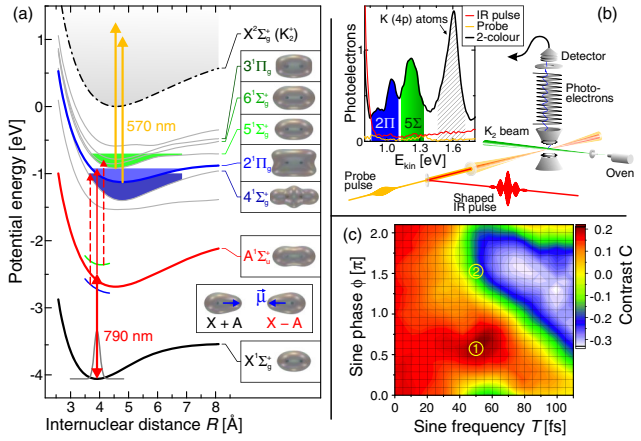

FIG. 1 (color online). (a) Excitation and detection scheme, (b) experimental setup and measured photoelectron signals, and (c) measured contrast landscape. For details, see the text.

the X-A subsystem, visualized by the distinct electronic superpositions of maximum coherence. The PESs are modified, and the corresponding dressed states (indicated by short blue and green line segments above and below the $A\,^1\Sigma_u^+$ PES around $R = 3.9$ Å) give access to lower (blue-shaded area between the $4\,^1\Sigma_g^+$ and the $2\,^1\Pi_g$ PES) and higher-lying (green-shaded area between the $5\,^1\Sigma_g^+$ and the $3\,^1\Pi_g$ PES) electronic target states. In the experiment, a probe pulse (yellow arrows) photoionizes the excited molecule and maps the target state populations into the photoelectron spectrum.

This strong-field control scenario can be realized by a double pulse sequence consisting of a moderately strong preparation pulse followed by a more intense main pulse [17,20,24]. In this scenario, both pulses are resonant with the X-A transition. This pulse sequence permits a transparent analysis of the physical mechanism. The preparation pulse gives rise to an *electronic* coherence in the X-A subsystem, launching an electronic wave packet. The time evolution of the electronic wave packet is reflected in the oscillating dipole moment $\vec{\mu}(t)$. The dipole oscillates with a molecular Bohr period proportional to the energy difference in the X-A subsystem of about 2.8 fs. Analogous to a classical oscillator driven on resonance, the induced dipole initially follows the driving field with a phase shift of $-\pi/2$. The subsequent intense main pulse interacts with the dipole, giving rise to an interaction energy $\varepsilon(t) = -\vec{\mu}(t) \cdot \vec{E}(t)$ that is analogous to a classical dipole in an electric field. The interaction energy is controlled precisely by the phase relation in the scalar product. A main pulse which is timed to oscillate out of phase with the previously induced dipole *maximizes* $\varepsilon(t)$. Higher-lying electronic target states become energetically accessible and are excited selectively. Shifting the main pulse in time by half an optical cycle causes in-phase oscillations of the laser and the dipole. This leads to *minimization* of $\varepsilon(t)$, i.e., to selective excitation of lower-lying electronic target states. In a quantum mechanical framework, maximization (minimization) of the interaction energy corresponds to selective population of a dressed state (SPODS) [25]. Here, this means selective population of the upper (lower) molecular dressed state of the resonant X-A subsystem. The dressed state energy splitting is proportional to the amplitude of the electric field.

Following these arguments, high precision phase control to suitably adapt the laser field to the induced dipole dynamics ($\vec{E}$ and $\vec{\mu}$ antiparallel or parallel) in combination with amplitude control to adapt the interaction energy to the separation of the target states, i.e., several 100 meV [17], are the ingredients for selective excitation on the ultrafast time scale.

In practice, the straightforward implementation using a double pulse sequence does not always lead to the optimal controllability of molecular systems [20,21]. In general, the light-induced electric dipole is subject to additional phase dynamics due to vibrational wave packet propagation on the PESs during the interaction with the laser pulse; i.e., the electronic resonance becomes time dependent, introducing dynamic detuning. This coupling between electron and nuclear motion influences the amplitude and phase of the coherent charge oscillation. Thus, the interplay between the driving laser field, which simultaneously induces and controls the dipole dynamics, and the driven molecule is more complex. To allow for this complexity, we used more versatile pulse shapes in terms of both temporal amplitude and phase. To this end, we applied a sinusoidal phase modulation $\varphi(\omega) = A \sin[T(\omega - \omega_0) + \phi]$ to our laser spectrum. This spectral phase modulation yields a multipulse sequence [17,26–28]. The features of the sequence are adjusted by the phase parameters A, T, and ϕ. The sine amplitude A determines the amplitudes of the subpulses; their temporal separation is given by the sine frequency T. The sine phase ϕ controls the relative temporal phases between adjacent subpulses and exerts phase control on the electric dipole dynamics.

A schematic of the experimental setup is displayed in Fig. 1(b); for further details, see Ref. [23]. An amplified Ti:sapphire laser system provides pulses of 25 fs FWHM at a central wavelength of about 790 nm. Because of the blue detuning of the laser spectrum with respect to the X-A resonance (846 nm at $R_0 = 3.9$ Å), the system is biased toward excitation of the $2\,^1\Pi_g$ state. Under these conditions, we observe switching between the states $2\,^1\Pi_g$ and $5\,^1\Sigma_g^+$ rather than between the states $4\,^1\Sigma_g^+$ and $5\,^1\Sigma_g^+$, as discussed in the theory [20]. The amplified IR pulses are spectrally phase modulated according to $\varphi(\omega)$ using our home-built Fourier transform pulse shaper based on a liquid crystal spatial light modulator. The shaped IR pulses are focused into a potassium supersonic molecular beam. The laser and molecular beams intersect between the pole plates of a magnetic bottle time-of-flight photoelectron spectrometer. In the experiments on K_2, the final

PRL 110, 123003 (2013) PHYSICAL REVIEW LETTERS week ending 22 MARCH 2013

population in the neutral electronic target channels is measured by photoionization and detection of photoelectrons. Ionization is triggered by a 570 nm probe pulse [yellow photon arrows in Fig. 1(a)] from an optical parametric amplifier, which follows the shaped IR pulse collinearly into the interaction region, allowing for nearly background-free detection of photoelectrons from the molecular target states $2^1\Pi_g$ and $5^1\Sigma_g^+$, as seen in the measured photoelectron spectrum in Fig. 1(b) (for more details, see Ref. [23]). The photoelectrons from the $2^1\Pi_g$ state are a measure for the final population in the lower electronic target channel. Photoelectrons from the target states $5^1\Sigma_g^+$, $6^1\Sigma_g^+$, and $3^1\Pi_g$ are a measure for the final population in the upper electronic target channel. For simplicity, we will refer to the entire upper target channel contribution as the $5^1\Sigma_g^+$ signal. For the following discussions, we introduce the contrast $C = (S_{5\Sigma} - S_{2\Pi})/(S_{5\Sigma} + S_{2\Pi})$ between the integrated signal yields $S_{2\Pi}$ [blue-shaded area in the inset to Fig. 1(b)] and $S_{5\Sigma}$ (green-shaded area), as a scalar measure for the selectivity achieved in the population of a specific electronic target channel.

First, we investigated the intensity dependence of the population transfer to the electronic target channels by the bandwidth-limited IR pulse. This procedure provides an unambiguous check on the strong-field nature of the excitation process and rules out perturbative scenarios such as spectral interference. Our findings (see Supplemental Fig. 2) confirm that, in the weak-field limit, i.e., for laser intensities smaller than 1×10^{11} W/cm^2, only the $2^1\Pi_g$ state is accessible. Efficient population of higher-lying target states is only achieved above a threshold intensity of about 5×10^{11} W/cm^2. This observation proves the nonperturbative character of the scenario. Subsequently, we studied strong-field *phase* control on the K_2 molecule. To this end, we chose a fixed IR pulse intensity of 8.5×10^{11} W/cm^2, at which the upper target channel was populated most efficiently and almost selectively by the bandwidth-limited pulse. The sine amplitude was set to $A = 0.8$ rad, which was found to provide a high degree of control on both the upper and the lower target channel yields. The experimental result of a systematic variation of the phase parameters T and ϕ is illustrated in Fig. 1(c) in terms of a two-dimensional contrast landscape.

A pronounced maximum is found around $T = 50$ fs and $\phi = 1.8$ rad with $C = 0.21$ [see Fig. 1(c), label 1], the high sine frequency of $T = 50$ fs hinting to vibrational wave packet dynamics. The corresponding photoelectron spectrum is shown in Fig. 2(a). The photoelectron yield

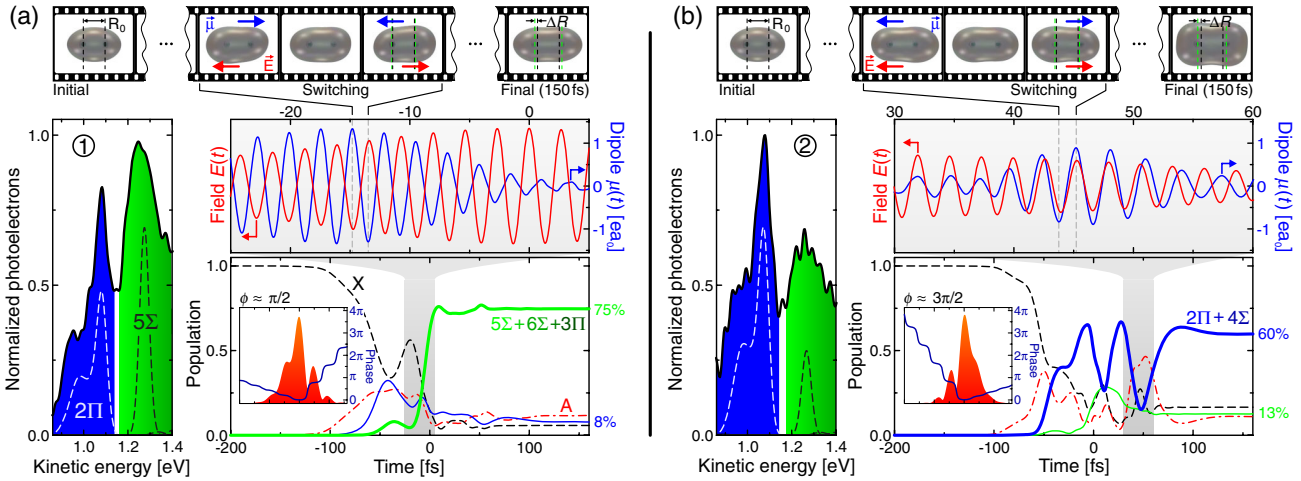

FIG. 2 (color online). Experimental and theoretical results for the excitation of K_2 molecules with two different pulse shapes, leading to population of (a) the upper target state $5^1\Sigma_g^+$ and (b) the lower target state $2^1\Pi_g$. On both sides, the left frame shows the measured photoelectron spectra (black line, signal contributions colored accordingly) compared to simulations, taking focal intensity and molecular orientation averaging into account (dashed lines). To the right of these spectra, the neutral electronic population dynamics are shown, along with the driving shaped IR pulses, decomposed into their temporal amplitude (red background) and phase (blue line), as insets. The black dashed line represents the ground state $X^1\Sigma_g^+$, the red dash-dotted line the intermediate state $A^1\Sigma_u^+$. For clarity, the blue and green curves represent the accumulated populations of the lower (i.e., the $2^1\Pi_g$ and the $4^1\Sigma_g^+$ states) and upper (i.e., the $5^1\Sigma_g^+$, $6^1\Sigma_g^+$, and $3^1\Pi_g$ states) electronic target channels. The phase relation of the electric field $E(t)$ (red line) and the induced electric dipole moment $\mu(t)$ of the X-A subsystem (blue line) is illustrated in the upper right frame. It depicts the interplay of dipole and field during the switching time window (gray-shaded background) where the population transfer to the electronic target channels takes place. The amplitude and phase modulation of the electronic dipole with respect to the constant electric field directly reflects the coupling between the nuclear and electronic motion. Out-of-phase (in-phase) oscillation of μ and E, as on the left-hand (right-hand) side, maximizes (minimizes) the interaction energy and results in efficient population of the upper (lower) electronic target channel. The movies on top show snapshots of the driven charge oscillation for decisive moments during the laser-molecule interactions.

of the upper target channel exceeds the one generated by the bandwidth-limited IR pulse that is also included in the landscape in Fig. 1(c) for $T = 0$ fs with a contrast of $C = 0.12$, proving efficient population of the upper target channel. Simultaneously, the low yield of photoelectrons from the lower target channel indicates the selectivity achieved by the shaped IR pulse. From the basic control scheme derived on atoms, we expect switching from the upper to the lower target channel by a change of the sine phase by $\Delta\phi = \pi$ [17] as the signature of SPODS. Indeed, we find efficient population of the lower target channel at a phase shift of about π at a fixed subpulse separation of $T = 50$ fs with $C = -0.2$; see Fig. 1(c), label 2, and Fig. 2(b) for the measured photoelectron spectrum. Here, the high photoelectron signal from the lower target channel together with the low signal from the upper target channel indicate selective and efficient population of the lower electronic target channel. Generally, the regions of selective excitation are not as sharply defined as in atoms due to molecular orientation averaging. To extract a realistic picture of the underlying control mechanism for the distinct pulse shapes shown in Figs. 2(a) and 2(b), we carried out quantum dynamics simulations. The calculations included the coupled nuclear and electronic wave packet propagation induced by the intense shaped IR pulses. This approach allows us to visualize and follow the prepared oscillating dipole $\mu(t)$. A detailed description of the numerical techniques applied in the calculations is given in Refs. [20,23,29]. We model the K_2 molecule by seven electronic states, cf. Fig. 1(a), and approximate the experimental parameters by a Gaussian-shaped input pulse centered at 800 nm with a FWHM duration of 30 fs. The input pulse is sinusoidally phase modulated in the frequency domain according to $\varphi(\omega)$. To elucidate the underlying control mechanism, we assume the shaped IR pulses to be polarized at 45° with respect to the internuclear axis of the diatomic molecule for the simulation of the population dynamics. Thus, parallel ($\Sigma \leftarrow \Sigma$) and perpendicular ($\Pi \leftarrow \Sigma$) transitions are driven by the same intensity. For the actual comparison between measured and simulated photoelectrons, however, we consider both focal intensity averaging and molecular orientation averaging in order to model the experimental conditions. The measured photoelectron spectra and the results of the simulations are presented in Fig. 2. For a detailed description of the displayed quantities, we refer to the figure caption. The measured two-color photoelectron spectrum associated with the pulse shape (a) is characterized by a pronounced $5^1\Sigma_g^+$ signal that clearly exceeds the contribution from the $2^1\Pi_g$ state. Initially, between -100 and -50 fs, the laser field guides the ground state $X^1\Sigma_g^+$ and the resonant intermediate state $A^1\Sigma_u^+$ into a coherent electronic superposition, launching the oscillating electric dipole. In the switching time window, the dipole oscillates with maximum amplitude exactly out of phase with the electric field of the main pulse. The intense central subpulse opens the upper target channel energetically and, due to the maximization of the interaction energy $\varepsilon(t)$, transfers the population efficiently to the high-lying set of target states. The lower electronic target channel remains nearly unpopulated. During the time between the buildup of the electronic coherence and the switching time, the internuclear distance increases by 8% due to the vibrational dynamics, resulting in a change of the Bohr frequency of 100 meV. This coupling between the nuclear and electronic motions is directly reflected in the amplitude and phase modulations of the electric dipole in relation to the driving laser field, as stated in the introduction, and would not be seen in the case of a resonantly driven atom. The good agreement of the measured and simulated photoelectron spectra confirms the high degree of control achieved in the experiment. For the width of the simulated signals, a spectrometer resolution of 50 meV (at 1.2 eV) was taken into account. Additional broadening due to the width of the optical parametric amplifier probe spectrum (70 meV) was not considered. The simulation results for the pulse shape (b) are presented on the right-hand side of Fig. 2. In the measured and calculated photoelectron spectra, a considerable enhancement of the $2^1\Pi_g$ at the expense of the $5^1\Sigma_g^+$ signal is observed. Inspection of the population dynamics reveals again a buildup of the *X*-*A* coherence between -100 and -50 fs. After this time period, a more complicated population dynamics is observed. Rabi cycling in the lower electronic target channel occurs due to the fact that (i) the transition dipole moment between states $2^1\Pi_g$ and $A^1\Sigma_u^+$ is larger than the corresponding coupling between states $5^1\Sigma_g^+$ and $A^1\Sigma_u^+$ [20] and (ii) the lower target channel is always accessible energetically. However, after the completion of the second Rabi cycle, around 45 fs, the dipole increases once more and shifts in phase with the shaped laser pulse during the switching time window. Thus, the interaction energy $\varepsilon(t)$ is minimized and the lower target states are populated efficiently, while the upper electronic target channel remains almost unpopulated. Owing to the longer time until the switching occurs, the internuclear separation has by then increased by 11% and the frequency of the oscillating dipole is changed by 130 meV.

The electron movies in the upper panels of Fig. 2 visualize the spatial aspects of the induced electronic and nuclear motion together with the associated dipole moment $\vec{\mu}(t)$ (blue arrows) and the applied electric field $\vec{E}(t)$ (red arrows). Starting from the ground state configuration, the movies proceed via the transient electron dynamics during the switching time window and end with the molecule in its final electronic configuration. The vertical black and green dashed lines indicate the nuclear dynamics during the interaction. On the left-hand side, the induced dipole and the electric field oscillate strictly out of phase, steering the molecule into a peanut-shaped electron configuration dominated by the $5^1\Sigma_g^+$ electron density distribution

[cf. Fig. 1(a)]. On the right-hand side, $\vec{\mu}(t)$ and $\vec{E}(t)$ oscillate strictly in phase. As a result, the molecule is guided into a cushionlike electronic configuration, clearly reflecting the $2^1\Pi_g$ electron density distribution.

We demonstrated efficient ultrafast switching between bound electronic target states in a molecule by intense femtosecond laser pulses shaped with attosecond precision. It was shown how accurate phase control of photoinduced electron dynamics combined with specific manipulation of the potential energy landscape using resonant strong laser fields allows us to steer the molecular system efficiently into a preselected electronic target channel. The key to strong-field control of coupled electron-nuclear dynamics is tailoring the phase of the driving laser field to the charge oscillation of the induced electron wave packet. We note that signatures of this control scenario have also been observed in the controlled fragmentation of isopropyl alcohol [5]. Promising applications of the presented scenario therefore range from ultrafast coherent control of valence bond chemistry in complex systems to efficient ultrafast switching in quantum information processing [30].

The Kassel group gratefully acknowledges financial support by the Deutsche Forschungsgemeinschaft (DFG) and the Otto Braun Fonds. This work was furthermore supported by the European Commission Project FASTQUAST. The Munich group gratefully acknowledges support by the DFG via the Cluster of Excellence: Munich Centre of Advanced Photonics, the SFB749, and the Normalverfahren.

*wollenhaupt@physik.uni-kassel.de

[1] M. Shapiro and P. Brumer, *Quantum Control of Molecular Processes* (Wiley-VCH, Berlin, 2011) and references therein.
[2] A. Zewail, J. Phys. Chem. A **104**, 5660 (2000).
[3] A. M. Weiner, Opt. Commun. **284**, 3669 (2011).
[4] T. Brixner, G. Krampert, T. Pfeifer, R. Selle, G. Gerber, M. Wollenhaupt, O. Graefe, C. Horn, D. Liese, and T. Baumert, Phys. Rev. Lett. **92**, 208301 (2004).
[5] M. Wollenhaupt and T. Baumert, Faraday Discuss. **153**, 9 (2011) and references therein.
[6] P. B. Corkum and F. Krausz, Nat. Phys. **3**, 381 (2007).
[7] M. F. Kling and M. J. J. Vrakking, Annu. Rev. Phys. Chem. **59**, 463 (2008).
[8] F. Krausz and M. Ivanov, Rev. Mod. Phys. **81**, 163 (2009).
[9] F. Remacle and R. D. Levine, Proc. Natl. Acad. Sci. U.S.A. **103**, 6793 (2006).
[10] P. J. Bustard, G. Wu, R. Lausten, D. Townsend, I. A. Walmsley, A. Stolow, and B. J. Sussman, Faraday Discuss. **153**, 321 (2011).
[11] T. Frohnmeyer, M. Hofmann, M. Strehle, and T. Baumert, Chem. Phys. Lett. **312**, 447 (1999).
[12] C. Trallero-Herrero, J. L. Cohen, and T. Weinacht, Phys. Rev. Lett. **96**, 063603 (2006).
[13] H. Goto, H. Katsuki, H. Ibrahim, H. Chiba, and K. Ohmori, Nat. Phys. **7**, 383 (2011).
[14] B. Sussman, D. Townsend, M. Ivanov, and A. Stolow, Science **314**, 278 (2006).
[15] S. H. Autler and C. H. Townes, Phys. Rev. **100**, 703 (1955).
[16] C. Meier and V. Engel, Phys. Rev. Lett. **73**, 3207 (1994).
[17] M. Wollenhaupt, D. Liese, A. Präkelt, C. Sarpe-Tudoran, and T. Baumert, Chem. Phys. Lett. **419**, 184 (2006).
[18] A. Palacios, H. Bachau, and F. Martín, Phys. Rev. A **74**, 031402 (2006).
[19] J. Köhler, M. Wollenhaupt, T. Bayer, C. Sarpe, and T. Baumert, Opt. Express **19**, 11 638 (2011).
[20] M. Wollenhaupt and T. Baumert, J. Photochem. Photobiol., A **180**, 248 (2006).
[21] P. von den Hoff, M. Kowalewski, and R. de Vivie-Riedle, Faraday Discuss. **153**, 159 (2011).
[22] J. Petersen and R. Mitrić, Phys. Chem. Chem. Phys. **14**, 8299 (2012).
[23] See Supplemental Material at http://link.aps.org/supplemental/10.1103/PhysRevLett.110.123003 for further details.
[24] T. Bayer, M. Wollenhaupt, C. Sarpe-Tudoran, and T. Baumert, Phys. Rev. Lett. **102**, 023004 (2009).
[25] M. Wollenhaupt, A. Präkelt, C. Sarpe-Tudoran, D. Liese, and T. Baumert, J. Opt. B **7**, S270 (2005).
[26] D. Meshulach and Y. Silberberg, Nature (London) **396**, 239 (1998).
[27] J. Herek, R. Wohlleben, R. Cogdell, D. Zeidler, and M. Motzkus, Nature (London) **417**, 533 (2002).
[28] M. Wollenhaupt, A. Präkelt, C. Sarpe-Tudoran, D. Liese, T. Bayer, and T. Baumert, Phys. Rev. A **73**, 063409 (2006).
[29] P. von den Hoff, I. Znakovskaya, M. F. Kling, and R. de Vivie-Riedle, Chem. Phys. **366**, 139 (2009).
[30] R. de Vivie-Riedle and U. Troppmann, Chem. Rev. **107**, 5082 (2007).

6 Summary and Outlook

Understanding the fundamental interaction between light and matter is an important step to tailor the control of electron and/or nuclear dynamics with laser pulses and guide experimental efforts. The first part of this work examined the angular dependence of the tunnel ionization of small hydrocarbons. While laser pulses are a great tool to take snapshots of nuclear dynamics and with attosecond pulses even electron dynamics, it is not an interference free method, as the laser interacts with the system and the information retrieved is not that of the undisturbed system but the system with laser. If the laser pulse is very short compared to the observed dynamics, then the influence of the laser on the dynamics is negligible, but even slightly longer pulses can leave an impact on the system. As demonstrated on the studied hydrocarbons, the signal stems from the light dressed orbitals and not from the undisturbed orbitals and the behavior of these orbitals differ. In the case of the CHD derivates AP and AT the field free HOMO and Lowest Unoccupied Molecular Orbital (LUMO) behave almost identical, but the more malleable C-C π-bonds give rise to a preferential tunnel ionization direction that ultimately leads to an anisotropy in the angular dependence for AT, but not for AP. The homologue series ethane, ethylene and acetylene shows that the stabilization of highly localized Rydberg-type orbitals is dependent on the presence of π-bonds. In contrast the orbitals in the diatomic molecules CO and N_2 do not show this characteristic.

The second and third part of this work demonstrate control over the nuclear and electron dynamics, respectively, with the help of laser pulses, that would not be possible without them. Both examples rely on the phase component of the laser field in a slightly different way. The controlled deprotonation and isomerization of acetylene and allene utilize the absolute phase or CEP of a single pulse, while the population of dressed states needs a relative phase shift between two pulses. Figure 6.1 shows this difference: in the top panel is one pulse envelope with different CEPs, demonstrating the change of the absolute phase, while in the bottom panel there are two pulse envelopes with a relative phase difference between them. In this work the absolute phase controlled the nuclear wave packet and thereby the nuclear dynamics, but it is also possible to control the electron dynamics with the CEP, for example in H_2^+.

The electron dynamics in the potassium dimer system studied in the third part is already influenced by the nuclear dynamics. So the more interesting question is not to control or describe the electron or the nuclear dynamics separately, but to investigate coupled nuclear and electron dynamics. The ansatz used in chapter 5 includes the dependence on the nuclear coordinate only as the time dependent expectation value $R(t)$ in equation 5.3. This approximation can not be used in more complex systems, especially in systems with more than one local minimum. To expand the ansatz, the nuclear coordinate has to be included explicitly, so the last line of equation 5.3 should read:

$$\sum_i a_i(t)|\Phi_i(r,R(t))|^2+\sum_i\sum_{j>i} 2Re\{a_i^*(t)a_j(t)\cdot\int \chi_i^*(R,t)\Phi_i^*(r,t;R(t))\Phi_j(r,t;R(t))\chi_j(R,t)\,\mathrm{d}R\} \tag{6.1}$$

This formulation allows to describe the coupled nuclear and electron dynamics in molecules (NEMol). One possible application for the NEMol ansatz is the keto-enol isomerization of 3-aminoacrolein [109].

The asymmetry of the nuclear dynamics in acetylene and allene with CEP controlled laser pulses may not be big enough to matter in a normal chemical synthesis, but the fact, that it works on a symmetric molecule is very important. While the investigated reactions lead to the same product, it demonstrates, that in principle the control scheme could lead to distinguishable products if they are different enantiomeres, i.e. the symmetric reaction takes place at a chiral center. As chiral molecules are very im-

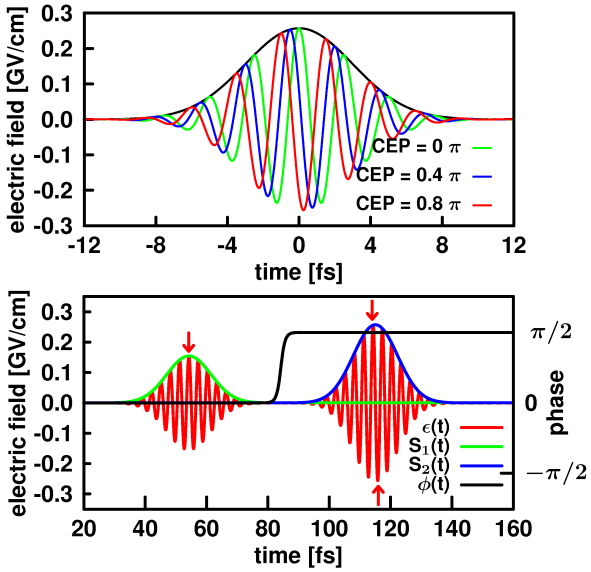

Figure 6.1: Top panel: Several laser pulses with varying CEP but the same envelope, showing the difference coming from the absolute phase of the laser field. Bottom panel: One pulse train consisting of two pulses with a relative phase difference between the first and second pulse.

portant in biological processes and therefore in pharmaceutical applications, even a small asymmetry in enantiomers could make a big difference in reactions without prior chiral selectivity or chiral catalysts. So the next step would be identifying possible PESs which would support CEP control of the nuclear wave packet. Figure 6.2 shows two promising traits for PESs with controllable reaction pathways. The first (left panel in Fig. 6.2) is the excitation to a transition state, that leads to the two products. This is the situation for the studied systems in section 4.2. The other option (right panel in Fig. 6.2) would be to control the passage through a conical intersection.

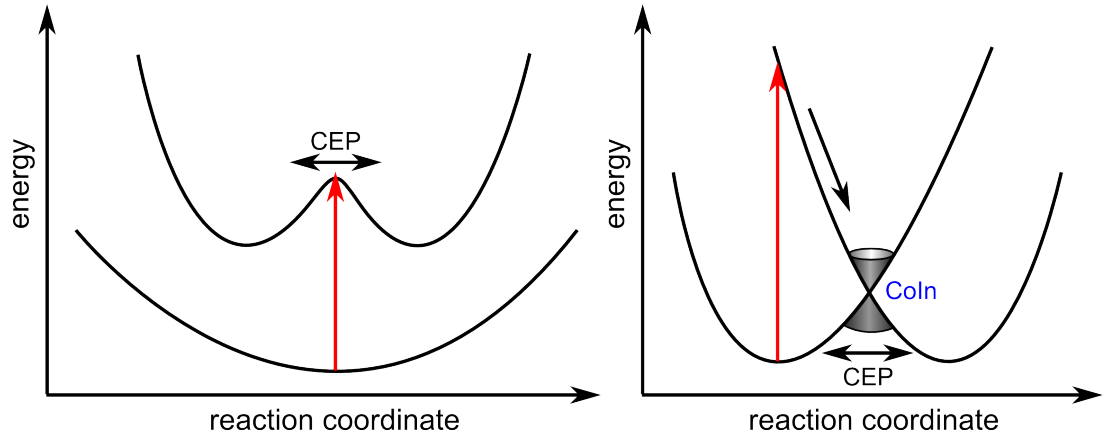

Figure 6.2: Left panel: schematic reaction that excite to an transition state to control the final product with the CEP of the laser. Right panel: schematic reaction, that uses a CoIn as a control point for the products.

While angular dependent tunnel ionization is normally not a prime example for coupled nuclear and electron dynamics, the measurement for ethene C_2H_4 in chapter 3 hints that possible interesting dynamics could be present. To replicate the pattern for the measured deprotonation, the calculated ionization has been mapped to the deprotonation. There are several possibilities to weight the different C-H bond dissociations to the ionization, but the weight mapping for the best agreement between measured and calculated values suggests an unequal treatment of the C-H bonds. The reason for this is probably that the electron dynamics, stemming from the electron leaving the system via tunnel ionization, influences

the nuclear dynamics for the two possible C-H bond dissociations by causing a preference for one of them. This is an interesting case of coupled nuclear and electron dynamics, as in the other examples the nuclear dynamics influences the electron dynamics and not the other way round. The idea to describe the influence of the electronic wave packet on the nuclear wave packet in a quantum dynamical way, would be to express the electron nuclei potential $V_{\mathrm{el,nuc}}$ time dependent. Preliminary calculations show that for the case of ethene, the first six excited states of the cation are likely not enough to accurately describe the time dependent potential.

7 List of abbreviations

ADK Ammosov–Delone–Krainov
AO Atomic orbital
AP α-phellandrene
AT α-terpinene
CAS Complete–Active–Space
CASPT2 Complete–Active–Space second-order perturbation theory
CASSCF Complete–Active–Space–Self–Consistent Field
CC Coupled Cluster
CEP Carrier–Envelope–Phase
CHD Cyclohexadiene
CI Configuration-Interaction
CoIn Conical Intersection
DFT Density Functional Theory
FDRC orbital Field Dressed orbital with Rydberg Character
HF Hartree–Fock
HOMO Highest Occupied Molecular Orbital
IR Infrared
KER Kinetic Energy Release
LCAO Linear combination of atomic orbitals
LUMO Lowest Unoccupied Molecular Orbital
MCTDH Multi Configuration Time Dependent Hartree
MO Molecular orbital
MRCI Multi-Reference Configuration-Interaction
NEMol Nuclear and Electron dynamic in Molecules
OCE Optimal–Control–Experiment
OCT Optimal–Control–Theory
PES Potential Energy Surface
PPT Perelomov–Popov–Terent'ev
RAS Restricted–Active–Space
SCF Self–Consistent Field
SFA Strong–Field–Approximation
SPODS Selective Population of Dressed States
TDDFT Time Dependent Density Functional Theory
TDM Transition Dipole Moment
TDSE Time Dependent Schrödinger Equation
VMI Velocity–Map Imaging

References

[1] D. Stichnoth, P. Kölle, T. J. Kimbrough, E. Riedle, R. de Vivie-Riedle and D. Trauner, *Photochemical formation of intricarene*, Nature Commun. **5**, 5597 (2014).

[2] B. P. Fingerhut, T. T. Herzog, G. Ryseck, K. Haiser, F. F. Graupner, K. Heil, P. Gilch, W. J. Schreier, T. Carell, R. de Vivie-Riedle and W. Zinth, *Dynamics of ultraviolet-induced DNA lesions: Dewar formation guided by pre-tension induced by the backbone*, New J. Phys. **14**, 065006 (2012).

[3] C. Gollub, M. Kowalewski, S. Thallmair and R. de Vivie-Riedle, *Chemoselective quantum control of carbonyl bonds in Grignard reactions using shaped laser pulses*, Phys. Chem. Chem. Phys. **12**, 15780 (2010).

[4] A. H. Zewail, *Femtochemistry: Atomic-Scale Dynamics of the Chemical Bond Using Ultrafast Lasers (Nobel Lecture)*, Angew. Chem. Int. Ed. **39**, 2586 (2000).

[5] M. J. Rosker, M. Dantus and A. H. Zewail, *Femtosecond real-time probing of reactions. I. The technique*, J. Chem. Phys. **89**, 6113 (1988).

[6] M. Dantus, M. J. Rosker and A. H. Zewail, *Femtosecond real-time probing of reactions. II. The dissociation reaction of ICN*, J. Chem. Phys. **89**, 6128 (1988).

[7] N. Krebs, I. Pugliesi and E. Riedle, *Pulse Compression of Ultrashort UV Pulses by Self-Phase Modulation in Bulk Material*, Appl. Sci. **3**, 153 (2013).

[8] P. Baum, S. Lochbrunner and E. Riedle, *Generation of tunable 7-fs ultraviolet pulses: achromatic phase matching and chirp management*, Appl. Phys. B – Lasers O. **79**, 1027 (2004).

[9] E. Riedle, M. Beutter, S. Lochbrunner, J. Piel, S. Schenkl, S. Spörlein and W. Zinth, *Generation of 10 to 50 fs pulses tunable through all of the visible and the NIR*, Appl. Phys. B – Lasers O. **71**, 457 (2000).

[10] C. Manzoni, D. Polli and G. Cerullo, *Two-color pump-probe system broadly tunable over the visible and the near infrared with sub-30fs temporal resolution*, Rev. Sci. Instrum. **77**, 023103 (2006).

[11] G. Cerullo, M. Nisoli and S. De Silvestri, *Generation of 11 fs pulses tunable across the visible by optical parametric amplification*, Appl. Phys. Lett. **71**, 3616 (1997).

[12] D. Polli, M. Antognazza, D. Brida, G. Lanzani, G. Cerullo and S. D. Silvestri, *Broadband pump-probe spectroscopy with sub-10-fs resolution for probing ultrafast internal conversion and coherent phonons in carotenoids*, Chem. Phys. **350**, 45 (2008).

[13] D. Strickland and G. Mourou, *Compression of amplified chirped optical pulses*, Opt. Commun. **56**, 219 (1985).

[14] M. Bradler, P. Baum and E. Riedle, *Femtosecond continuum generation in bulk laser host materials with sub-μJ pump pulses*, Appl. Phys. B – Lasers O. **97**, 561 (2009).

[15] T. Helgaker, P. Jorgensen and J. Olsen, *Molecular Electronic-Structure Theory*, John Wiley & Sons Ltd., Chichester, England (2013).

[16] W. Kutzelnigg, *Einführung in die Theoretische Chemie*, WILEY-VCH Verlag Gmbh, Weinheim (2002).

[17] A. Szabo and N. S.Ostlund, *Modern quantum chemistry: introduction to advanced electronic structure theory*, Dover Piblications, Inc., Mineola, New York (1996).

[18] I. N. Levine, *Quantum Chemistry*, Prentice Hall, fifth edn. (2000).

[19] D. J. Tannor, *Introduction to Quantum Mechanics: A Time-Dependent Perspective*, University Science Books, Sausalito, California, USA (2007).

[20] J. A. Pople, *Quantum Chemical Models (Nobel Lecture)*, Angew. Chem. Int. Ed. **38**, 1894 (1999).

[21] C. Ochsenfeld, J. Kussmann and D. S. Lambrecht, *Linear-Scaling Methods in Quantum Chemistry*, in K. B. Lipkowitz and T. R. Cundari (eds.), *Reviews in Computational Chemistry*, pp. 1–82, John Wiley & Sons, Inc. (2007).

[22] C. Y. Yam, Q. Zhang, F. Wang and G. H. Chen, *Linear-scaling quantum mechanical methods for excited states*, Chem. Soc. Rev. **41**, 3821 (2012).

[23] R. Zaleśny, M. G. Papadopoulos, P. G. Mezey and J. Leszczynski (eds.), *Linear-Scaling Techniques in Computational Chemistry and Physics*, vol. 13 of *Challenges and Advances in Computational Chemistry and Physics*, Springer Netherlands (2011).

[24] J. Kussmann, M. Beer and C. Ochsenfeld, *Linear-scaling self-consistent field methods for large molecules*, WIREs Comput. Mol. Sci. **3**, 614 (2013).

[25] W. Kohn, *Nobel Lecture: Electronic structure of matter—wave functions and density functionals*, Rev. Mod. Phys. **71**, 1253 (1999).

[26] M. Casida and M. Huix-Rotllant, *Progress in Time-Dependent Density-Functional Theory*, Annu. Rev. Phys. Chem. **63**, 287 (2012), PMID: 22242728.

[27] C. Adamo and D. Jacquemin, *The calculations of excited-state properties with Time-Dependent Density Functional Theory*, Chem. Soc. Rev. **42**, 845 (2013).

[28] E. Runge and E. K. U. Gross, *Density-Functional Theory for Time-Dependent Systems*, Phys. Rev. Lett. **52**, 997 (1984).

[29] A. Hofmann, *Ultraschnelle molekulare Quantendynamik durch konische Durchschneidungen*, Ph.D. thesis, Ludwig-Maximilians-Universität München (2001).

[30] A. Hofmann and R. de Vivie-Riedle, *Adiabatic approach for ultrafast quantum dynamics mediated by simultaneously active conical intersections*, Chem. Phys. Lett. **346**, 299 (2001).

[31] H. J. Monkhorst, *Calculation of properties with the coupled-cluster method*, International Journal of Quantum Chemistry **12**, 421 (1977).

[32] J. Cizek and J. Paldus, *Coupled Cluster Approach*, Physica Scripta **21**, 251 (1980).

[33] M. J. Bearpark, F. Ogliaro, T. Vreven, M. Boggio-Pasqua, M. J. Frisch, S. M. Larkin, M. Morrison and M. A. Robb, *CASSCF calculations for photoinduced processes in large molecules: Choosing when to use the RASSCF, ONIOM and MMVB approximations*, J. Photochem. Photobiol. A **190**, 207 (2007).

[34] B. O. Roos, *Theoretical studies of electronically excited states of molecular systems using multiconfigurational perturbation theory*, Acc. Chem. Res. **32**, 137 (1999).

[35] K. Andersson, P. A. Malmqvist, B. O. Roos, A. J. Sadlej and K. Wolinski .

[36] K. Andersson, P. Malmqvist and B. O. Roos, *Second-order perturbation theory with a complete active space self-consistent field reference function*, The Journal of Chemical Physics **96** (1992).

[37] R. Ditchfield, W. J. Hehre and J. A. Pople, *Self-Consistent Molecular-Orbital Methods. IX. An Extended Gaussian-Type Basis for Molecular-Orbital Studies of Organic Molecules*, J. Chem. Phys. **54**, 724 (1971).

[38] P. Hariharan and J. Pople, *The influence of polarization functions on molecular orbital hydrogenation energies*, Theor. Chim. Acta **28**, 213 (1973).

[39] V. A. Rassolov, M. A. Ratner, J. A. Pople, P. C. Redfern and L. A. Curtiss, *6-31G* basis set for third-row atoms*, J. Comput. Chem. **22**, 976 (2001).

[40] M. Kowalewski, *Quantendynamik isolierter molekularer Systeme*, Ph.D. thesis, Ludwig-Maximilians-Universität München (2012).

[41] M. H. Beck, A. Jäckle, G. A. Worth and H.-D. Meyer, *The multiconfiguration time-dependent Hartree method: A highly efficient algorithm for propagating wavepackets.*, Phys. Rep. **324**, 1 (2000).

[42] H.-D. Meyer, *Studying molecular quantum dynamics with the multiconfiguration time-dependent Hartree method*, Wiley Interdisciplinary Reviews: Computational Molecular Science **2**, 351 (2012).

[43] J. C. Tully, *Mixed quantum-classical dynamics*, Faraday Discuss. **110**, 407 (1998).

[44] M. Barbatti, G. Granucci, M. Persico, M. Ruckenbauer, M. Vazdar, M. Eckert-Maksić and H. Lischka, *The on-the-fly surface-hopping program system Newton-X: Application to ab initio simulation of the nonadiabatic photodynamics of benchmark systems*, J. Photochem. Photobiol. A **190**, 228 (2007), Theoretical Aspects of Photoinduced Processes in Complex Systems.

[45] M. Richter, P. Marquetand, J. González-Vázquez, I. Sola and L. González, *SHARC: ab Initio Molecular Dynamics with Surface Hopping in the Adiabatic Representation Including Arbitrary Couplings*, J. Chem. Theory Comput. **7**, 1253 (2011).

[46] S. Mai, P. Marquetand and L. González, *A general method to describe intersystem crossing dynamics in trajectory surface hopping*, Int. J. Quantum Chem. pp. 1215–1231 (2015).

[47] X. Andrade, D. Strubbe, U. De Giovannini, A. H. Larsen, M. J. T. Oliveira, J. Alberdi-Rodriguez, A. Varas, I. Theophilou, N. Helbig, M. J. Verstraete, L. Stella, F. Nogueira, A. Aspuru-Guzik, A. Castro, M. A. L. Marques and A. Rubio, *Real-space grids and the Octopus code as tools for the development of new simulation approaches for electronic systems*, Phys. Chem. Chem. Phys. **17**, 31371 (2015).

[48] G. Kolesov, O. Grånäs, R. Hoyt, D. Vinichenko and E. Kaxiras, *Real-Time TD-DFT with Classical Ion Dynamics: Methodology and Applications*, Journal of Chemical Theory and Computation **12**, 466 (2016), PMID: 26680129.

[49] V. Roudnev, B. D. Esry and I. Ben-Itzhak, *Controlling HD^+ and H_2^+ Dissociation with the Carrier-Envelope Phase Difference of an Intense Ultrashort Laser Pulse*, Phys. Rev. Lett. **93** (2004).

[50] J. Hu, M.-S. Wang, K.-L. Han and G.-Z. He, *Attosecond resolution quantum dynamics between electrons and H_2^+ molecules*, Phys. Rev. A **74**, 063417 (2006).

[51] I. Kawata, H. Kono and Y. Fujimura, *Adiabatic and diabatic responses of H_2^+ to an intense femtosecond laser pulse: Dynamics of the electronic and nuclear wave packet*, J. Chem. Phys. **110**, 11152 (1999).

[52] M. F. Kling, C. Siedschlag, A. J. Verhoef, J. I. Khan, M. Schultze, T. Uphues, Y. Ni, M. Uiberacker, M. Drescher, F. Krausz and M. J. J. Vrakking1, *Control of Electron Localization in Molecular Dissociation*, Science **312**, 312 (2006).

[53] X. M. Tong and C. D. Lin, *Dynamics of Light-Field Control of Molecular Dissociation at the Few-Cycle Limit*, Phys. Rev. Lett. **98** (2007).

[54] F. He, C. Ruiz and A. Becker, *Control of Electron Excitation and Localization in the Dissociation of H_2^+ and Its Isotopes Using Sequential Ultrashort Laser Pulses*, Phys. Rev. Lett. **99**, 083002 (2007).

[55] M. V. Korolkov, K.-M. Weitzel and S. D. Peyerimhoff, *Spin orbit induced predissociation dynamics of HCl^+ and HBr^+ ions: temporal and spectral representations*, International Journal of Mass Spectrometry **201**, 109 (200).

[56] A. D. Pradhan, K. P. Kirby and A. Dalgarno, *Theoretical study of HCl^+: Potential curves, radiative lifetimes, and photodissociation cross sections.*, J. Chem. Phys. **95**, 9009 (1991).

[57] D. Pavičić, K. F. Lee, D. M. Rayner, P. B. Corkum and D. M. Villeneuve, *Direct Measurement of the Angular Dependence of Ionization for N_2, O_2, and CO_2 in Intense Laser Fields*, Phys. Rev. Lett. **98**, 243001 (2007).

[58] L. G. M. Petterson, M. Larson and S. Svensson, *The X-ray excited Auger electron spectrum of NO and potentialcurves and photodissociation of the NO^{2+} ion.*, J. Chem. Phys. **96**, 4884 (1992).

[59] P. von den Hoff, I. Znakovskaya, M. Kling and R. de Vivie-Riedle, *Attosecond control of the dissociative ionization via electron localization: A comparison between D_2 and CO*, Chemical Physics **366**, 139 (2009), Attosecond Molecular Dynamics.

[60] I. Znakovskaya, P. von den Hoff, S. Zherebtsov, A. Wirth, O. Herrwerth, M. J. J. Vrakking, R. de Vivie-Riedle and M. F. Kling, *Attosecond Control of Electron Dynamics in Carbon Monoxide*, Phys. Rev. Lett. **103**, 103002 (2009).

[61] A. H. Zewail, *Laser Femtochemistry*, Science **242**, 1645 (1988).

[62] A. H. Zewail, *Femtochemistry: Atomic-Scale Dynamics of the Chemical Bond*, J. Phys. Chem. A **104**, 5660 (2000).

[63] X. M. Tong, Z. Zhao and C. D. Lin, *Theory of molecular tunneling ionization*, Phys. Rev. A **66** (2002).

[64] D. R. Yarkony, *Nonadiabatic Quantum Chemistry – Past, Present, and Future*, Chem. Rev. **112**, 481 (2012).

[65] S. Matsika and P. Krause, *Nonadiabatic Events and Conical Intersections*, Annu. Rev. Phys. Chem. **62**, 621 (2011).

[66] A. Nenov, *Relation between molecular structure and ultrafast photoreactivity with application to molecular switches*, Ph.D. thesis, Ludwig-Maximilians-Universität München (2012).

[67] W. Fuß, S. Lochbrunner, A. Müller, T. Schikarski, W. E. Schmid and S. Trushin, *Pathway approach to ultrafast photochemistry: potential surfaces, conical intersections and isomerizations of small polyenes*, Chemical Physics **232**, 161 (1998).

[68] C. J. Cramer, *Essentials of Computational Chemistry - Theories and Models*, John Wiley & Sons Ltd., Chichester, England (2004).

[69] H.-J. Werner, P. J. Knowles, G. Knizia, F. R. Manby, M. Schütz, P. Celani, T. Korona, R. Lindh, A. Mitrushenkov, G. Rauhut, K. R. Shamasundar, T. B. Adler, R. D. Amos, A. Bernhardsson, A. Berning, D. L. Cooper, M. J. O. Deegan, A. J. Dobbyn, F. Eckert, E. Goll, C. Hampel, A. Hesselmann, G. Hetzer, T. Hrenar, G. Jansen, C. Köppl, Y. Liu, A. W. Lloyd, R. A. Mata, A. J. May, S. J. McNicholas, W. Meyer, M. E. Mura, A. Nicklass, D. P. O'Neill, P. Palmieri, D. Peng, K. Pflüger, R. Pitzer, M. Reiher, T. Shiozaki, H. Stoll, A. J. Stone, R. Tarroni, T. Thorsteinsson and M. Wang, *MOLPRO, Version 2012.1, A Package of Ab Initio Programs* (2012).

[70] D. Geppert, P. von den Hoff and R. de Vivie-Riedle, *Electron dynamics in molecules: a new combination of nuclear quantum dynamics and electronic structure theory*, J. Phys. B: At. Mol. Opt. Phys. **41**, 074006 (2008).

[71] C. Leforestier, R. H. Bisseling, C. Cerjan, M. D. Feit, R. Friesner, A. Guldberg, A. Hammerich, G. Jolicard, W. Karrlein, H.-D. Meyer, N. Lipkin, O. Roncero and R. Kosloff, *A Comparison of Different Propagation Schemes for the Time Dependent Schrödinger Equation*, J. Comput. Phys. **94**, 59 (1991).

[72] M. Y. Ivanov, M. Spanner and O. Smirnova, *Anatomy of strong field ionization*, Journal of Modern Optics **52**, 165 (2005).

[73] Y. Mairesse, J. Higuet, N. Dudovich, D. Shafir, B. Fabre, E. Mével, E. Constant, S. Patchkovskii, Z. Walters, M. Y. Ivanov and O. Smirnova, *High Harmonic Spectroscopy of Multichannel Dynamics in Strong-Field Ionization*, Phys. Rev. Lett. **104**, 213601 (2010).

[74] A. S. Alnaser, I. Litvinyuk, T. Osipov, B. Ulrich, A. Landers, E. Wells, C. M. Maharjan, P. Ranitovic, I. Bochareva, D. Ray and C. L. Cocke, *Momentum-imaging investigations of the dissociation of D 2 + and the isomerization of acetylene to vinylidene by intense short laser pulses*, Journal of Physics B: Atomic, Molecular and Optical Physics **39**, S485 (2006).

[75] R. de Vivie-Riedle, K. Kobe, J. Manz, W. Meyer, B. Reischl, S. Rutz, E. Schreiber and L. Wöste, *A Femtosecond Study of Multiphoton Ionization Processes in K_2: From Pump-Probe to Control*, J. Chem. Phys. **100**, 7789 (1996).

[76] T. Popmintchev, M.-C. Chen, P. Arpin, M. M. Murnane and H. C. Kapteyn, *The attosecond nonlinear optics of bright coherent X-ray generation*, Nat Photon **4**, 822 (2010).

[77] E. Goulielmakis, V. S. Yakovlev, A. L. Cavalieri, M. Uiberacker, V. Pervak, A. Apolonski, R. Kienberger, U. Kleineberg and F. Krausz, *Attosecond Control and Measurement: Lightwave Electronics*, Science **317**, 769 (2007).

[78] K. C. Kulander, *Time-dependent Hartree-Fock theory of multiphoton ionization: Helium*, Phys. Rev. A **36**, 2726 (1987).

[79] M. Uiberacker, T. Uphues, M. Schultze, A. J. Verhoef, V. Yakovlev, M. F. Kling, J. Rauschenberger, N. M. Kabachnik, H. Schroder, M. Lezius, K. L. Kompa, H.-G. Muller, M. J. J. Vrakking, S. Hendel, U. Kleineberg, U. Heinzmann, D. . JOUR, M. Drescher and F. Krausz, *Attosecond real-time observation of electron tunnelling in atoms*, Nature **446**, 627 (2007).

[80] M. Wollenhaupt, M. Krug, J. Köhler, T. Bayer, C. Sarpe-Tudoran and T. Baumert, *Photoelectron angular distributions from strong-field coherent electronic excitation*, Applied Physics B **95**, 245 (2009).

[81] L. DiMauro and P. Agostini, *Ionization dynamics in strong laser fields*, Advances in Atomic, Molecular, and Optical Physics **35**, 79 (1995).

[82] F. H. M. Faisal, A. Becker and J. Muth-Böh, *ntense-Field Many-Body S-Matrix Theory: Applications to Processes in Femtosecond Laser Pulses*, Laser Physics **9**, 115 (1999).

[83] A. M. Perelomov, V. S. Popov and M. V. Terent'ev, *Ionization of atoms in an alternating electric field*, Zh. Eksp. Teor. Fiz. **51**, 309 (1966).

[84] M. V. Ammosov, N. B. Delone and V. P. Krainov, *Tunnel ionization of complexatoms and of atomic ions in an alternating electromagnetic field*, Zh. Eksp. Teor. Fiz. **91**, 2008 (1986).

[85] C. Z. Bisgaard and L. B. Madsen, *Tunneling ionization of atoms*, American Journal of Physics **72**, 249 (2004).

[86] A. M. M. Hussien, *Ionization of diatomic molecules in intense laser fields*, Ph.D. thesis (2015).

[87] V. P. Majety and A. Scrinzi, *Dynamic Exchange in the Strong Field Ionization of Molecules*, Phys. Rev. Lett. **115**, 103002 (2015).

[88] P. von den Hoff, I. Znakovskaya, S. Zherebtsov, M. F. Kling and R. de Vivie-Riedle, *Effects of multi orbital contributions in the angular-dependent ionization of molecules in intense few-cycle laser pulses*, Applied Physics B **98**, 659 (2010).

[89] I. Barth, H.-C. Hege, H. Ikeda, A. Kenfack, M. Koppitz, J. Manz, F. Marquardt and G. K. Paramonov, *Concerted quantum effects of electronic and nuclear fluxes in molecules*, Chemical Physics Letters **481**, 118 (2009).

[90] P. von den Hoff, *Gekoppelte Kern- und Elektronendynamik: Molekulare Systeme und deren Kontrolle durch die Bewegung der Elektronen.*, Ph.D. thesis, Ludwig-Maximilians-Universität München (2012).

[91] T. Brixner and G. Gerber, *Quantum Control of Gas-Phase and Liquid-Phase Femtochemistry*, ChemPhysChem **4**, 418 (2003).

[92] F. Krausz and M. Ivanov, *Attosecond physics*, Rev. Mod. Phys. **81**, 163 (2009).

[93] T. Baumert, T. Brixner, V. Seyfried, M. Strehle and G. Gerber, *Femtosecond pulse shaping by an evolutionary algorithm with feedback*, Applied Physics B: Lasers and Optics **65**, 779 (1997).

[94] M. Dugan, J. Tull and W. Warren, *High-resolution acousto-optic shaping of unamplified and amplified femtosecond laser pulses*, JOSA B **14**, 2348 (1997).

[95] F. Lücking, A. Assion, A. Apolonski, F. Krausz and G. Steinmeyer, *Long-term carrier-envelope-phase-stable few-cycle pulses by use of the feed-forward method*, Opt. Lett. **37**, 2076 (2012).

[96] T. Rathje, N. G. Johnson, M. Möller, F. Süßmann, D. Adolph, M. Kübel, R. Kienberger, M. F. Kling, G. G. Paulus and A. M. Sayler, *Review of attosecond resolved measurement and control via carrier-envelope phase tagging with above-threshold ionization*, Journal of Physics B: Atomic, Molecular and Optical Physics **45**, 074003 (2012).

[97] M. Schultze, A. Wirth, I. Grguras, M. Uiberacker, T. Uphues, A. Verhoef, J. Gagnon, M. Hofstetter, U. Kleineberg, E. Goulielmakis and F. Krausz, *State-of-the-art attosecond metrology*, Journal of Electron Spectroscopy and Related Phenomena **184**, 68 (2011), Advances in Vacuum Ultraviolet and X-ray PhysicsThe 37th International Conference on Vacuum Ultraviolet and X-ray Physics (VUVX2010).

[98] B. J. Whitaker, *Imaging in Molecular Dynamics: Technology and Applications*, Cambridge University Press (2003).

[99] C. Bordas, F. Paulig, H. Helm and D. L. Huestis, *Photoelectron imaging spectrometry: Principle and inversion method*, Review of Scientific Instruments **67**, 2257 (1996).

[100] M. Barbatti, M. Ruckenbauer, F. Plasser, J. Pittner, G. Granucci, M. Persico and H. Lischka, *Newton-X: a surface-hopping program for nonadiabatic molecular dynamics*, WIREs Comput. Mol. Sci. **4**, 26 (2014).

[101] A. Baltuska, T. Udem, M. Uiberacker, M. Hentschel, E. Goulielmakis, C. Gohle, R. Holzwarth, V. S. Yakovlev, A. Scrinzi, T. W. Hänsch and F. Krausz, *Attosecond control of electronic processes by intense light fields*, Nature **421**, 611 (2003).

[102] M. F. Kling, P. von den Hoff, I. Znakovskaya and R. de Vivie-Riedle, *(Sub-)femtosecond control of molecular reactions via tailoring the electric field of light*, Phys. Chem. Chem. Phys. **15**, 9448 (2013).

[103] A. Baltuška, T. Udem, M. Uiberacker, M. Hentschel, E. Goulielmakis, C. Gohle, R. Holzwarth, V. S. Yakovlev, A. Scrinzi, T. W. Hänsch and F. Krausz, *Attosecond control of electronic processes by intense light fields*, Nature **421**, 611 (2003).

[104] M. Wollenhaupt, A. Präkelt, C. Sarpe-Tudoran, D. Liese and T. Baumert, *Quantum control by selective population of dressed states using intense chirped femtosecond laser pulses*, Appl. Phys. B **82**, 183 (2006).

[105] T. Bayer, M. Wollenhaupt and T. Baumert, *Strong-field control landscapes of coherent electronic excitation*, J. Phys. B: At. Mol. Opt. Phys. **41**, 074007 (2008).

[106] T. Bayer, M. Wollenhaupt, C. Sarpe-Tudoran and T. Baumert, *Robust Photon Locking*, Phys. Rev. Lett. **102**, 023004 (2009).

[107] M. Wollenhaupt and T. Baumert, *Ultrafast strong field quantum control on K_2 dimers*, Journal of Photochemistry and Photobiology A: Chemistry **180**, 248 (2006).

[108] J. Petersen and R. Mitric, *Electronic coherence within the semiclassical field-induced surface hopping method: strong field quantum control in K_2*, Phys. Chem. Chem. Phys. **14**, 8299 (2012).

[109] T. B. Schnappinger, *Gekoppelte Kern- und Elektronendynamik: Ein Methodenvergleich am Beispiel von 3-Aminoacrolein*, Master's thesis, Ludwig-Maximilians-Universität München Fakultät Chemie und Pharmazie Department Chemie und Biochemie (2015).